Politecnico di Torino

ScuDo
Scuola di Dottorato ~ Doctoral School
WHAT YOU ARE, TAKES YOU FAR

Doctoral Dissertation
Doctoral Program in Aerospace Engineering (36^{th}cycle)

Methodology and Tools for High-Speed Vehicles Conceptual Design to Support Environmental Regulations

By

Oscar Gori

******

Supervisor(s):
Prof. Nicole Viola

Doctoral Examination Committee:
Dr. Thomas Roetger, Referee, ENVISA
Dr. Roberto Scigliano, Referee, Centro Italiano Ricerche Aerospaziali
Dr. Martin Schaefer, Board Member, European Union Aviation Safety Agency
Dr. Luca Boggero, Board Member, Deutsches Zentrum für Luft-und Raumfahrt
Prof. Marco Fioriti, Board Member, Politecnico di Torino

Politecnico di Torino
2024

Declaration

I hereby declare that, the contents and organization of this dissertation constitute my own original work and does not compromise in any way the rights of third parties, including those relating to the security of personal data.

Oscar Gori
2024

* This dissertation is presented in partial fulfillment of the requirements for **Ph.D. degree** in the Graduate School of Politecnico di Torino (ScuDo).

Acknowledgements

I want to thank my supervisors and colleagues for their consistent support, guidance, and helpful feedback during my PhD research. Their expertise and encouragement played a crucial role in shaping my work.
A special thanks to my family for always being there, understanding, and supporting me. Their love provided the strength I needed to overcome challenges during this academic journey.
Thank you to my friends who cheered me on and supported me along the way, adding depth to my experience.
Thanks to Alessia for walking alongside me on this journey.
Thank you to the partners of the STRATOFLY and More&Less projects for their collaboration and dedication to advancing our field. Their contributions were essential to completing this thesis.
This thesis wouldn't have been possible without the collective support of these individuals, and I'm truly grateful for their impact on both my academic and personal growth.

Abstract

In recent years, there has been a growing interest in high-speed passenger transportation systems. Consequently, there is a compelling need to develop rapid and reliable methods to be applied during the initial phases of design, when the selected configuration remains susceptible to potential changes. This thesis seeks to introduce innovative methodologies and tools for the conceptual design of high-speed vehicles, in support to environmental regulations. The accurate estimation of the aerodynamic features of high-speed vehicles is a pivotal aspect of preliminary design. To address this, the methodology presented here aims at enhancing the evaluation of aerodynamic characteristics in the early stages of design, when more advanced aerodynamic analyses, such as Computational Fluid Dynamics (CFD) simulations, are not yet available. The work is based on models already available in the literature, which are modified to better adapt to the vehicle configurations considered in the analysis. Depending on the flight regime, two main configuration types can be considered: the typical wing-body configuration for cruise Mach number in the low supersonic regime (i.e. from Mach 1.5 to Mach 3) and the waverider configuration for the hypersonic regime with Mach greater than 5. The workflow includes static stability and trim analysis for a complete preliminary vehicle characterization. Moreover, even if mission simulation is typically reserved for later stages of the design process, the proposed methodology involves the exploitation of mission simulation since the very early phases of the conceptual design.

The research activity has been carried on within the field of two Horizon 2020 European Union funded projects, the STRATOFLY and the MORE&LESS projects. The case studies considered in those projects are exploited for the test and validation of the methodology developed during the research.

The technical data collected from the different analyses can then be used as input to support the development of environmental regulations specifically tailored for

high-speed aircraft, focusing on the CO_2 certification emission standards. At the moment, those standards are defined for subsonic aircraft only, since no high-speed aircraft is currently flying in the airspace. For that reason, it is important to work towards the definition of a specific certification standard for supersonic concepts. The proposed methodology suggests the exploitation of mission simulation data, to evaluate to what extent the present regulations are capable of representing supersonic aircraft behaviour and, in case this is not verified, to support the work towards the definition of emission standards specifically tailored for high-speed vehicles.

Contents

List of Figures

List of Tables

Nomenclature

Roman Symbols

$(x/c)_{max}$	Chordwise location of the airfoil maximum thickness point
$\frac{t}{c}$	Airfoil thickness to chord length ratio
a	Aircraft acceleration on ground
a	Semi-major axis
b	Semi-minor axis
C_D	Drag coefficient
C_L	Lift coefficient
C_M	Pitching moment coefficient
C_{D_0}	Zero lift drag coefficient
C_{D_F}	Skin-friction drag coefficient
C_{D_i}	Induced drag coefficient
$C_{D_{bB}}$	Body bluntness drag coefficient
$C_{D_{fB}}$	Body friction drag coefficient
$C_{D_{pB}}$	Body pressure drag coefficient
$C_{D_{VL}}$	Vortex induced drag coefficient
$C_{D_{WL}}$	Wave drag due to lift coefficient

$C_{D_{WV}}$	Wave drag due to volume coefficient
C_{f_c}	Flat plate skin-friction coefficient
C_{L_0}	Zero angle of attack lift coefficient
C_{L_α}	Lift-curve slope
C_{M_y}	Pitching moment coefficient
CO_2	Carbon Dioxide
d	Fuselage diameter
d_A	Approaching distance
d_F	Flare distance
d_s	Landing run
d_{TD}	Touch-down distance
f	Rolling friction factor
FF_c	Component Form Factor
$h_{0_{LDG}}$	Landing obstacle clearance
I_{sp}	Specific impulse
l	Length
l	Total body length
l_h	Position of the breakpoint between forebody and afterbody
$LH2$	Liquid Hydrogen
n_z	Contingency factor along z-axis at take-off
$n_{x_{LDG}}$	contingency load at landing along x-axis
$n_{z_{LDG}}$	Contingency load at landing along z-axis
NO_x	Nitrogen Oxides

Q_c Interference drag factor

R Thrust rating

$S_{exposed}$ Exposed wing planform

S_{max} Maximum cross-section area

S_{plan} Total planform area

T Take-off thrust

T/D Thrust-to-Drag ratio

T_{le} Maximum radiation equilibrium temperature

t_{LO} Time required to perform rotation

t_{TD} Time required to complete touch-down

V Velocity

V_1 Take-off decision speed

V_2 Initial climb speed

V_{LDG} Final landing speed

x_{CoG} Position of the centre of gravity

CoG Centre of Gravity

Greek Symbols

α Angle of attack

α_{trim} Trim angle of attack

ε_{skin} Skin emissivity

η Airfoil Efficiency

γ Complement of the leading edge sweep angle

γ Glide scope angle

γ Heat capacity ratio

γ_0 Climb path angle

Λ_{le} Leading-edge sweep angle

μ Air viscosity

ρ Air density

Acronyms / Abbreviations

ARV Ascent and Re-entry Vehicle

ASD Accelerate&Stop Distance

ASDA Accelerate-Stop Distance Available

ATR Air Turbo Rocket

BAC British Aircraft Corporation

BOC Begin Of Cruise

CAEP Committee on Aviation Environmental Protection

CAV Cruise and Acceleration Vehicles

DMR Dual Mode Ramjet

EOC End Of Cruise

ESM Experimental Service Module

EU European Union

FCS Flight Control System

HEXAFLY High-Speed Experimental Fly Vehicles

HEXAFLY-INT High-Speed Experimental Fly Vehicles - INTernational

HOTOL HOrizontal Take Off and Landing

ICAO International Civil Aviation Organization

LAPCAT-II Long-term Advanced Propulsion Concepts And Technologies II

LDA Landing Distance Available

LTO Landing and Take-off Cycle

MAC Mean Aerodynamic Chord

MOC Mid Of Cruise

MTOM Maximum Take-Off Mass

MZFM Maximum Zero Fuel Mass

NACA National Advisory Committee for Aeronautics

NASA National Aeronautics and Space Administration

O−ARV Orbital Ascent and Re-entry Vehicle

OEW Operative Empty Weight

OML Outer Mould Line

PLdB Perceived Level decibel

RBCC Rocket-Based Combined Cycles

RGF Reference Geometry Factor

RV−NW Non-Winged Re-entry Vehicle

RV−W Winged Re-entry Vehicle

SAF Sustainable Aviation Fuel

SAR Specific Air Range

SO−ARV SubOrbital Ascent and Re-entry Vehicle

SST SuperSonic Transport

TBCC Turbine-Based Combined Cycles

TOD Take-Off Distance

TODA Take-Off Distance Available

TOR Take-Off Run with critical engine failure TOR_{n-1}

TORA Take-Off Run Available

TRL Technology Readiness Level

Chapter 1

Context and scope of the research activity

Since the very beginning of the aviation era and during the 20th century, the aviation sector has experienced rapid development, evolving from its early stages up to the establishment of a global airline market. This fast evolution was particularly fuelled by political and economic incentives, including the influences of the two World Wars and the Cold War. Across this period, various milestones were achieved, driven by a diverse array of basic research initiatives and technology development programs, responding to the fluctuating economic, political, and technological landscapes. As the world transitioned into the new millennium, a compelling imperative emerged within the scientific and engineering community to modernize civil passenger aircraft and redefine mission concepts. In particular, the focus moved towards mitigating the climate impact of the aviation sector, implementing more sustainable air transportation systems. This shift presented a fresh set of challenges for designers, emphasizing the reduction of greenhouse gases, pollutant emissions, and noise emissions for current and future commercial aircraft. In particular, especially in the European Union (EU), this effort is enhanced by the EU's aim to reach climate neutrality by 2050 [1]. Simultaneously, after several decades dominated by subsonic commercial flight, the interest in high-speed regimes has resurfaced, presenting attractive prospects for the transportation landscape of the medium and long term.

Within the described scenario, commercial suborbital flight has emerged as a new reality together with different initiatives focusing on the development and im-

provement of high-speed technologies, potentially representing the first step towards new reliable, advanced, and safe high-speed transportation systems. In particular, the research presented in this thesis has been conducted within the framework of two European initiatives focused on collaborative research in high-speed flight and funded by the European Commission:

- the Horizon 2020 STRATOFLY project [2, 3], which addresses Stratospheric Flying Opportunities for High-Speed Propulsion Concepts;
- the Horizon 2020 More&Less project [4], which is focused on MDO and Regulations for Low-boom and Environmentally Sustainable Supersonic aviation.

Since the early 2000s, a number of projects have received funding from the European Commission, all dedicated to advancing the Technology Readiness Level (TRL) of key technologies for high-speed flight. The multitude of initiatives in this field serves as a testament to the inherent complexity associated with high-speed flight research, which involves a high integration of many disciplines such as aerodynamics, propulsion, aerothermodynamics, etc. Hence, a collaborative effort is essential since the very early phases of the design, to guarantee the best outcome in terms of performance as well as compliance with the initial set of requirements. Moreover, the design is also driven by the main target to reach an appropriate level of environmental sustainability and safety, as well as to guarantee a high level of protection for citizens. This means that specific attention is paid to the estimation of emissions: not only for what concern the pollutants, but also looking at greenhouse gasses, noise, and sonic boom. It should also be highlighted that the present environmental regulations do not fully cover the high-speed flight regime. The only existing regulations have been established by ICAO in terms of noise and emissions standards and are referred to the Concorde case, which is the only supersonic aircraft that entered into service in the aviation history. Moreover, supersonic flight is currently prohibited over land due to the sonic boom effects, so that only transatlantic and transpacific routes can be exploited for high-speed aircraft, limiting the SuperSonic Transport (SST) operability [5]. For that reason, the Committee for Aviation Environmental Protection of the International Civil Aviation Organization (ICAO-CAEP) [6] is currently focusing on the noise and emissions characteristics of modern and future high-speed passenger concepts, with the main aim of review and update existing regulations, while also working on the possible development of future certification standards [5].

The present work proposes a new methodology and tools to be used for the conceptual design of environmentally sustainable high-speed concepts, in support of the update and development of environmental regulations. A multi-fidelity and multidisciplinary approach is required to fulfil this objective: starting from the aircraft configuration, aerodynamic models available in the literature are exploited for the initial aerodynamic characterization of each concept, and are later modified to improve the prediction during the very early phases of the design. Those data are then used as input to perform mission simulation to validate the concepts along the reference trajectory. The entire set of results can then be exploited to support the ongoing work on the environmental regulations for high-speed aircraft.

Chapter 2 provides an overview of the main characteristics of high-speed civil aircraft, based on their concept and mission type. Then, a description of the main drivers of high-speed aircraft design are also reported, with a particular focus on the aerodynamic and propulsive characteristics of this kind of vehicle. Moreover, the environmental issues of high-speed aircraft design are also illustrated, focusing on the impact on climate change, noise and pollutant emissions, and sonic boom. This chapter continues with an overview of past and future high-speed concepts developed around the world. Eventually, two of the latest EU funded projects on high-speed concepts, the STRATOFLY and the MORE&LESS project are described, since the research activity illustrated in this thesis has been conducted within the framework of those two projects.

Chapter 3 is dedicated to the description of the case studies considered in the analysis, divided into wing-body concepts and waverider configurations. Their reference mission is also presented, to provide a complete overview of the concepts.

Chapter 4 presents the methodology employed to perform the research activity, which involves a preliminary aerodynamic characterization, based on aerodynamic models available in the literature. Static stability analysis is also included, followed by a verification of the aircraft performance along the reference trajectory through mission simulation. Moreover, the capability of a given high-speed concept to abide by the present operational procedures in airport proximity is also evaluated, focusing on the required distance to complete take-off and landing. This is also intended to verify the aircraft's capability to operate within present airport infrastructures.

Chapter 5 illustrates the main results obtained during the research activity. First, the proposed empirical corrections to the aerodynamic models, which are derived

and adapted considering the specific configurations under study, are presented. Then, a comparison between the performance evaluated with those models and the ones obtained through higher fidelity analysis is carried on, focusing on the impact on the aircraft performance along the mission. The results of the static stability and trimmability analysis are also reported here, for the specific configuration of a Mach 8 waverider. Moreover, the take-off and landing distances required are also computed, to verify the compliance with the main international airport runways. Eventually, the work carried on in support of a possible modification and update of environmental regulations is presented, focusing in particular on the CO_2 emissions standards, which are currently defined for subsonic aircraft only.

Finally, a discussion on the main achievements of the research activity is presented, together with some suggestions for possible improvements to the proposed methodology and results in future works.

Chapter 2

Introduction

The demand for faster and environmentally friendly civil aviation is driving the worldwide scientific and aerospace community to design a new generation of high-speed aircraft that can be both environmentally sustainable and guarantee a high level of protection for citizens. Moreover, the emergence of innovative propulsion technologies, coupled with advancements in the design of civil high-speed passenger aircraft are prompting global authorities to revise the current regulatory frameworks. This work aims at mitigating ground-level effects and reducing the environmental impact and the contribution to climate change.

This chapter will provide an overview of the main characteristics of high-speed vehicles. First, section 2.1 reports the different categories of high-speed aircraft, based on their configuration and mission type. Then, section 2.2 describes the main drivers that lead the design of high-speed vehicles, focusing on the aerodynamic and propulsive characteristics typical of the supersonic and hypersonic regimes. The environmental issues of high-speed vehicle design are also described and reported in section 2.3. Eventually, section 2.4 provides an overview of past and future high-speed concepts, while section 2.5 describes two European-funded projects where the research presented in this thesis was conducted.

2.1 High-speed civil aircraft

In the near future, a wide range of high-speed civil and military applications are expected to operate in the same airspace, as summarized in Figure 2.1, which includes

both already existing vehicles and future concepts. Each type of concept can be characterized depending on the mission it is supposed to perform. For example, the lowest part of the airspace is characterized by subsonic cruise aircraft, which fly at a maximum altitude between 9 and 12 km. For higher cruise speeds, the cruise altitude will also be higher. Supersonic civil passenger aircraft ($1.5 \leq Mach \leq 3$) are designed to fly between 15 and 20 km. Moreover, hypersonic cruise vehicles are supposed to operate at higher altitudes between 20 and 40 km. All those concepts share the same mission type, which consists in transporting passengers from the departure site A to the arrival site B.

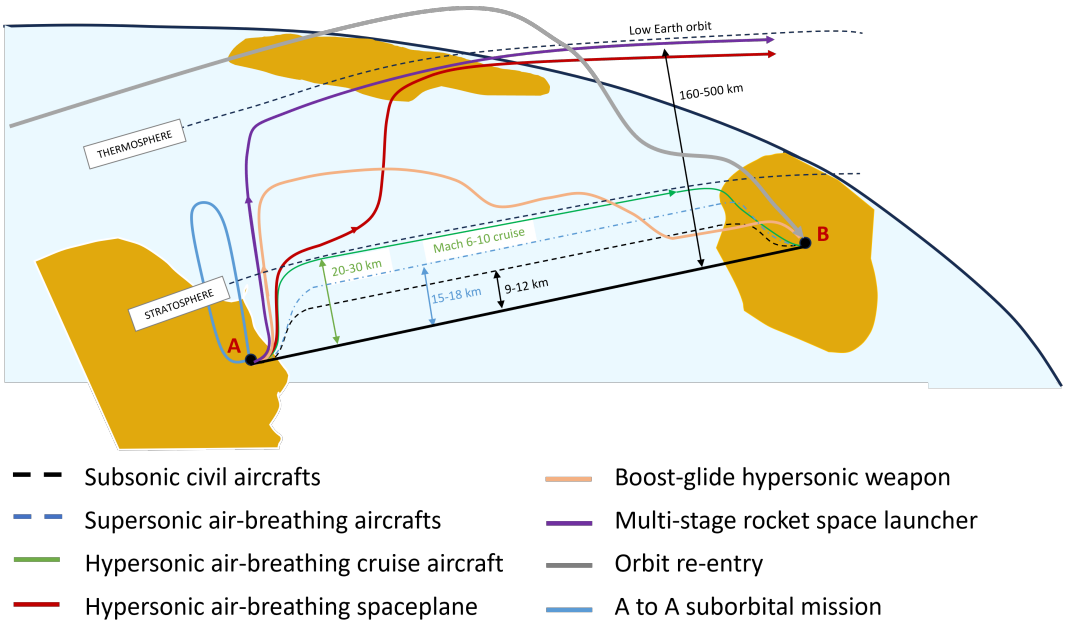

Fig. 2.1 High-speed missions concepts

However, different trajectory types can also be identified. For example, the red curve in the image shows the typical mission of a hypersonic air-breathing spaceplane. It departs from point A, then reaches the low Earth orbit, and returns to the starting point A to complete its mission. This type of vehicle usually exploits a combination of air-breathing engines up to an altitude between 30 and 40 km and rocket engines for higher altitudes. The multistage rocket space launcher performs a similar mission, while using only rocket engines as propulsion. Finally, suborbital vehicles are also included in this description, which fly up to an altitude of 100 km operating from point A and returning to the same location.

Due to this wide range of configurations for high-speed vehicles, a classification, according to the configuration type and the mission which it is supposed to complete, can be presented [7].
First, **Non-Winged Re-entry Vehicles (RV-NW)** can be considered. They include capsules and blunted cones, and they are generally designed for the re-entry phase from orbit into the Earth's atmosphere, following a gliding trajectory. They are launched on top of a rocket, which provides them the necessary acceleration to remain in the desired orbit or to escape Earth's gravity, depending on the mission requirements. Then, they perform a ballistic re-entry trajectory, followed by a braking phase, which is completed thanks to the support of a parachute system. Eventually, RV-NW can land either at sea or on the ground. They are characterized by a low lift-to-drag ratio, which is usually lower than 1.2. Additionally, their design is heavily influenced by the need to maximize drag for deceleration. Notable examples of this kind of vehicles are the Apollo Command Module and the Soyuz re-entry module.

Winged Re-entry Vehicles (RV-W) are usually more complex than the non-winged, and they are often reusable vehicles. They generally perform a controlled re-entry from orbital or sub-orbital missions to the Earth's surface. An important characteristic of this type of vehicle is that they fly at high angles of attack during the majority of the mission, to increase the drag and, as a consequence, the braking action. RV-W are launched on top of a rocket or take off horizontally from a carrier vehicle. The Space Shuttle Orbiter is one of the best examples of Winged Re-Entry vehicles.

Ascent and Re-entry Vehicles (ARV) are Single-Stage-To-Orbit (SSTO) space transportation systems, equipped with air-breathing and/or rocket propulsion. They are usually designed to reach Low Earth Orbit (LEO), and they are able to operate from subsonic to hypersonic velocities. For that reason, they are designed considering both aircraft and spacecraft characteristics. They can be further divided into Orbital Ascent and Re-entry Vehicles (O-ARV) or SubOrbital Ascent and Re-entry Vehicles (SO-ARV). For example, the Skylon spaceplane is a O-ARV, while the SpaceShipTwo is a SO-ARV.

Finally, **air-breathing Cruise and Acceleration Vehicles (CAV)** include supersonic and hypersonic aircraft which fly at low angles of attack, trying to minimize drag as much as possible. They are characterized by an aircraft-like shape and a high lift-to-drag ratio, which is usually greater than 4.5-5. Their propulsion system can be

a rocket motor, a combination of turbojet and rocket, or a combination of turbojet and ramjet/scramjet. The cruise phase is usually performed at high altitudes in the atmosphere, and they operate between two airports in a mission which is similar to one of the subsonic commercial airlines. Noteworthy examples of CAVs are the Concorde and Tupolev Tu-144.

The different types of vehicles presented here include the entire range of conditions that define the supersonic and hypersonic regime, from supersonic speed to orbit operations. Of course each concept is characterized by very different conditions during flight, and, for that reason, the analysis of the physical phenomena governing each flight condition can be fundamental to better address the design of this type of vehicle, while also better understanding the major challenges of high-speed flight. For that reason, the next section 2.2 is dedicated to the description of the main drivers of high-speed aircraft design, together with the fundamental characteristics of the supersonic and hypersonic environment.

2.2 Drivers of high-speed aircraft design

The design of high-speed vehicles presents significant challenges due to the unique features which characterize these concepts. High-speed systems are designed to fly through different flight regimes, ranging from subsonic to hypersonic velocities. Depending on the flight conditions, the flow physics, the aerodynamics and the propulsive characteristics exhibit significant variations. Furthermore, to ensure optimal performance and operability across various applications, high levels of integration are necessary.

This section reports the main drivers of high-speed aircraft design. Indeed, many aspects of aerodynamics, aerothermodynamics, propulsion, and flight control are unique to high-speed flight, which results in a challenging design and development of high-speed concepts [8]. At different Mach numbers, the aerodynamic behavior varies as the nature of the flow changes from subsonic to transonic, supersonic, and hypersonic flow. At high velocities like supersonic and hypersonic regimes, shock waves play a significant role. The airflow experiences compressions and expansions, leading to abrupt changes in pressure, temperature, and density levels. These changes are marked by regions that exhibit distinct characteristics within the airflow. In this regime, shock waves and Mach waves have shallow characteristics, which means

that disturbances in the flow have a limited extent of influence. The main direction of this influence is downstream.

Supersonic flow refers to the flow field in which the Mach number exceeds 1 at every point. It is characterized by the formation of shock waves, across which flow properties and streamlines change discontinuously [9]. This is in contrast to subsonic flow, which exhibits continuous variations. Moreover, since the local velocity of the flow is higher than the speed of sound, each disturbance generated at a specific location within the flow is unable to propagate upstream, in contrast to subsonic flow.

Quite the opposite, there is not a clear distinction between supersonic and hypersonic regime, as it exists while transitioning from subsonic to supersonic flight. While the supersonic regime is defined for Mach number greater than 1, the hypersonic regime is usually specified for Mach numbers greater than 5, since the flow characteristics start to change at this Mach number. The hypersonic regime, despite its name, is essentially supersonic. It is characterized by additional phenomena, such as shock waves and temperature increase, that become more significant as the Mach number rises. It is critical to recognize that the hypersonic regime is not completely distinct from the supersonic regime but is instead an extension of it. Therefore, it is important to take into account these additional phenomena that come into play as the Mach number increases when analyzing the behaviour of an object flying at hypersonic speeds. Depending on the specific case, these phenomena could occur at speeds either lower or higher than Mach 5, and for this reason, Mach 5 cannot be considered a fixed transition point from one flow regime to another.

Based on these definitions, the following paragraphs are dedicated to the description of the main characteristics of the flow at increasing Mach numbers. Starting from the condition which corresponds to the transition from subsonic to supersonic regime, as soon as Mach number approaches 1 (transonic regime), the pressure disturbances propagate transverse to the flow, generating normal shocks. As a consequence, the wave drag in this flight regime is high and depends primarily on the vehicle's maximum cross-sectional area. As the Mach number enters the hypersonic domain ($Mach \geq 5$), the shock layer (the region of airflow situated between the shock and the surface of the body) undergoes a significant reduction in thickness, while simultaneously becoming highly compressed and heated. The proximity of the shock wave to the object poses several challenges in designing its leading edges. The flow lacks sufficient time to lower its temperature, leading to the transfer of a majority of

its energy as heat and causing elevated heat fluxes across the object. Additionally, at the leading edge, the shock may encounter a bow-shaped surface, commonly known as a bow shock, which can be treated as an almost normal shock. In such instances, the distance between the bow shock and the body is extremely limited, generating critical heating issues.

Moreover, as the flow undergoes deceleration due to viscous effects within the boundary layer, a portion of the lost kinetic energy transforms into internal energy of the gas, a phenomenon known as viscous dissipation. Consequently, the temperature within the boundary layer rises. The increase in temperature greatly affects the behaviour of hypersonic boundary layers. For instance, the viscosity coefficient rises with temperature, contributing to an increase in the thickness of the boundary layer. Additionally, since the pressure in the normal direction across a boundary layer remains constant, an increase in temperature leads to a decrease in density. To maintain the required mass flow through the boundary layer at the reduced density, the boundary-layer thickness must be larger. Both these effects work in tandem, causing hypersonic boundary layers to grow more rapidly compared to slower speeds. This has also an effect on the inviscid flow outside the boundary layer, resulting in a distorted perception of the body shape, which appears larger. Substantial alterations in the outer inviscid flow are created, and these changes, in turn, influence the growth of the boundary layer. The phenomena between the boundary layer and the outer inviscid flow is named viscous interaction [10]. It plays a crucial role in affecting the surface-pressure distribution, thereby impacting lift, drag, and stability in hypersonic vehicles. It also contributes to increase skin friction and heat transfer.

Furthermore, the very high viscous dissipation usually leads to a huge increase in temperatures, which can vary from hundreds to thousands Kelvin, depending on the Mach number. The flow within the boundary layer is characterized by a chemically reacting gas, which leads to a change in the mathematical model describing its behaviour. For example, the assumption that the heat capacity ratio $\gamma = 1.4$ cannot be considered valid, and γ becomes a function of the temperature. If air at 1 atm pressure is considered, high-temperature effects start to be important for temperature higher than 800 K, while dissociation of O_2 and N_2 starts to occur from 2000 K. Ionization takes place at even higher temperatures, typically manifesting as a characteristic phenomenon during the re-entry phase. This occurrence contributes to the widely recognized challenges associated with communication blackouts, as the

presence of a substantial number of ions and electrons within the plasma surrounding the vehicle limits effective communication.

Nevertheless, hypersonic flight is generally characterized by low-density flows due to the inherently high altitudes at which vehicles operate. Specifically, at lower altitudes, the gas can be effectively treated using the continuum hypothesis. This involves treating the mixture as a single gas, even when composed of different molecules. The hypothesis relies on the mean free path among molecules, which denotes the average distance between successive collisions within the mixture. The formulation of the continuum hypothesis typically involves the use of the Knudsen number Kn to compare the mean free path λ with the body reference length L:

$$Kn = \frac{\lambda}{L} \tag{2.1}$$

For $Kn < 0.03$ the flow is considered continuum, for $Kn > 1$ free molecular flow is present, while for $0.3 < Kn < 1$ there is a transitional regime. In a given scenario, the Knudsen number serves as the criterion to assess the significance and extent of low-density effects. For instance, a very small Knudsen number indicates a continuum flow, while a very large Knudsen number suggests free molecular flow.

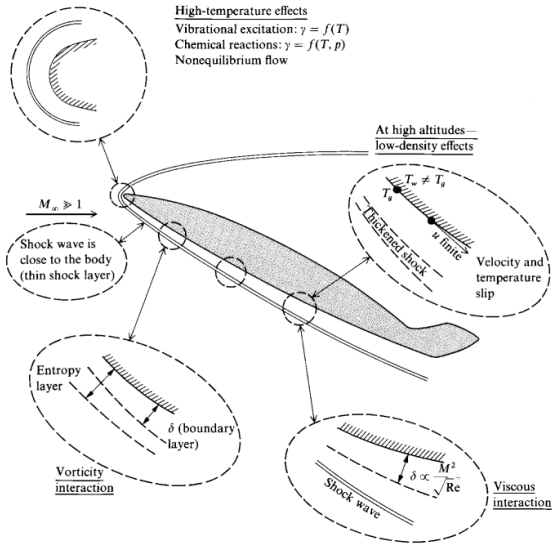

Fig. 2.2 Summary of the main effects of hypersonic flow [10]

A hypersonic vehicle performing re-entry from space is subject to these low-density effects, until it reaches a sufficiently low altitude in which the full continuum

aerodynamics is verified again. This altitude depends on the value of Kn, which, in turn, is a function of the dimension of the body. This means that, for larger vehicles, the continuum flow can be verified for higher altitudes than for smaller vehicles. Eventually, Figure 2.2 from [10] reports a summary of the typical phenomena which characterize the hypersonic flight, and that have been described in this chapter.

2.2.1 Aerodynamic characteristics of high speed vehicles

Aircraft's aerodynamic performance and stability are impacted significantly by flow characteristics across the Mach number range. Figure 2.3 reports the complete build-up of parasite drag C_{D_0} at the different Mach numbers. One of the key aerodynamic parameters that highlights the unique features of high-speed flight is the zero-lift drag C_{D_0}. C_{D_0} is formed by the skin friction drag and the wave drag due to volume. The first one is the predominant factor at subsonic speed, while the latter becomes significant from transonic Mach numbers. Indeed, the transonic peak around Mach 1 is caused by the wave drag increase, as shown in the plot. However, for higher Mach numbers C_{D_0} decreases, and at hypersonic speeds it could be lower than in the subsonic regime. The drag due to lift includes all the contribution to drag caused

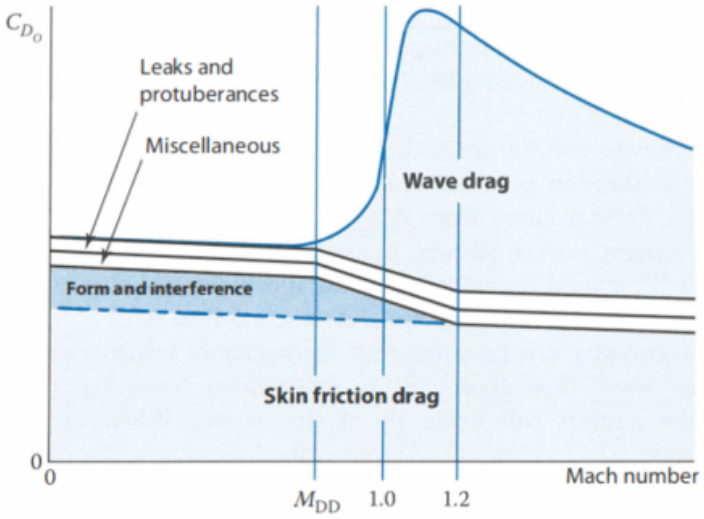

Fig. 2.3 C_{D_0} vs Mach number [11]

by the generation of lift, due to the fact that the lift distribution is not uniform on a wing. A pressure difference between the lower and upper wing surfaces creates

vortexes, especially near wing tips. It is clear that for higher values of C_L the drag due to lift also increases $\left(C_{D_i} = K \cdot C_L^2\right)$.

Aircraft longitudinal stability is another fundamental aspect to consider when dealing with high-speed aircraft design. It is defined by the derivative of the pitching moment coefficient (C_M) with respect to the C_L, which can be expressed as the distance between the position of the centre of gravity x_{CoG} and the aerodynamic centre x_{ac}, related to the reference length l, which is referred to as the static margin:

$$\frac{\partial C_M}{\partial C_L} = \left(x_{CoG} - x_{ac}\right)/l \tag{2.2}$$

If the static margin is negative the aircraft's stability is verified. Since the vehicle stability depends on the position of the aerodynamic centre, it is beneficial to analyze how it varies at the different Mach numbers. At subsonic velocities, x_{ac} is located approximately at $1/4$ of the Mean Aerodynamic Chord (MAC) of the wing, while at supersonic speeds it shifts towards the half of the MAC. Usually the static margin increases when moving from subsonic to supersonic regimes, while it decreases again for hypersonic speeds. The excessive stability at supersonic Mach numbers usually results in large control surface deflections, which are required to trim the vehicle, and that could lead to a very large trim drag. However, high-speed aircraft can opt for a reduced static margin to mitigate the adverse effects of trim drag, allowing for decreased stability during transonic/supersonic speeds and an acceptable level of instability during hypersonic and potentially subsonic speeds. This adjustment is feasible and can be implemented thanks to the availability of advanced active control systems.

2.2.2 Propulsive characteristics of high speed vehicles

Together with the aerodynamic design and performance analysis, the design of the propulsive system for high-speed vehicles is one of the most challenging task. The propulsive system should be able to accelerate the vehicle from take-off at low speeds up to supersonic and hypersonic velocities. Different types of engines should be considered depending on the cruise Mach number, since a single engine cannot cover the entire Mach range. Figure 2.4 reports the specific impulse I_{sp} of different engine types, depending on their Mach number.

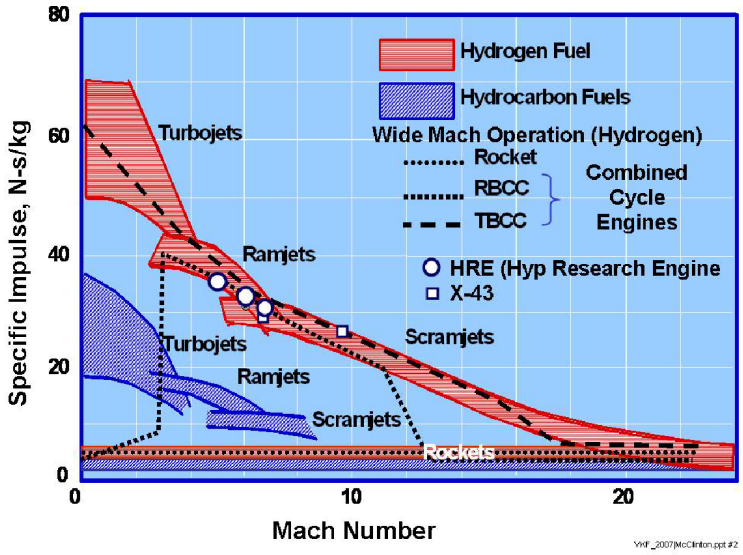

Figure 1. Hypersonic Engine Efficiency

Fig. 2.4 Specific impulse of different type of engines vs Mach number [12]

First, mission requirements define the most suitable propulsion system for a given case study. Air-breathing engines exploit atmospheric oxygen for combustion, which guarantees a reduction of weight and volume, while still having a higher specific impulse with respect to rockets, that are limited by the necessity to carry the oxidizer and fuel on-board. However, since the engine functioning depends directly on the Mach number, I_{sp} decreases with higher velocities. This means that the thrust decreases too. As can be seen in the figure, turbojet engines can be used up to Mach 3, while for higher Mach number ramjet or scramjet should be introduced. In particular, at least two engine types should be included in a hypersonic vehicle to ensure flying through different speed regimes. For example, a combination of integrated air-breathing and rocket concepts (air-turbo rockets), together with ramjet/scramjet can be a possibility for hypersonic concept's propulsion.

Moreover, different types of fuels can be used, such as typical hydrocarbons or liquid hydrogen ($LH2$). The main advantage of $LH2$ is the possibility to exploit its very high specific energy ε, which is equal to 143 MJ/kg, more than three times higher than the specific energy of hydrocarbons $\varepsilon = 42$MJ/kg. This results in a potential I_{sp} with $LH2$ which is double with respect to the one obtained with hydrocarbons. However, $LH2$ is also characterized by a lower volumetric density, higher production costs, and more difficult storage, compared to hydrocarbons. As a consequence, the impact of the $LH2$ on the aircraft configuration, and its weight,

is significant. First, if all other factors remain the same, the required hydrogen on-board is less than its kerosene counterpart, due to its high energy content. The aircraft gross weight will be also lower [13]. The engines of an aircraft powered by hydrogen fuel can be smaller but also more efficient, thanks to hydrogen's high specific heat capacity and its low storage temperature. In case of high-speed aircraft, the cryogenic hydrogen can be exploited to cool aircraft structures. However, the hydrogen storage requires up to 4 times more volume than kerosene. Moreover, due to the cryogenic properties of liquid hydrogen, tanks must also be designed with a low surface-to-volume ratio. This is necessary to minimize boil-off and reduce tank and insulation weight. Therefore, it is preferable to store the fuel in the fuselage to minimize the surface-to-volume ratio of the tanks. Consequently, fuselages are typically larger, resulting in a higher wetted area [13].

Thrust-to-Weight ratio (T/W) is another important parameter, which describes the engine performance. Air-breathing engines are characterized by lower T/W with respect to rockets, but the impact of this factor is limited if the lift is generated by aerodynamic forces (as it is for vehicles flying horizontally) instead of propulsion.

Considering all these aspects, it is possible to evaluate which type of propulsion is more suited for a given high-speed concept, while including also inlet and nozzle size requirements. For increasing Mach numbers the amount of air capture will be higher, leading to a very large inlet, engine and nozzle, which take up a significant part of the vehicle. Large propulsive components guarantee a sufficiently high thrust, but lead to some negative effects when flying in off-design conditions, especially at transonic speeds: inlet spillage and nozzle overexpansion drag can be very high in this case. Usually, a trade-off is carried on to find the best combination of component sizes, moving towards highly integrated vehicles.

A further parameter that is linked to the air-breathing vehicles' performance is the Thrust-to-Drag ratio (T/D). Of course, a high T/D means that the vehicle is efficient and that the fuel required to complete the mission will be lower. Moreover, a hydrocarbon vehicle would require more propellant than a liquid hydrogen one to fly at the same Mach number, due to the higher specific heat.

2.3 Environmental issues of high-speed aircraft design

Together with the main drivers described in the previous section, the design of high-speed vehicles cannot prevent from considering the environmental aspects impacting climate change, pollutant and noise emissions, sonic boom and social acceptance.

2.3.1 Impact on climate change

In December 2019 the European Commission presented its Green Deal with the main aim of reaching net carbon neutrality across all sectors and the European Union (EU) member states by 2050 [14]. At the same time, the Air Transport Action Group (ATAG) aims at a reduction of carbon dioxide (CO_2) emissions by 50% compared to 2005. However, the aviation world faces a significant challenge in achieving decarbonization in the following decades. This sector emits more than 900 million tons of CO_2 per year [14], and it is projected to double this amount by 2050, as can be seen in Figure 2.5, where the projection of CO_2 emission from aviation is reported. Per passenger, the aviation sector has become more carbon-efficient over the past three decades. Nevertheless, rising demand for air travel has led to a significant increase in direct CO_2 emissions from aviation, by 34 percent over the past five years. Growing populations and prosperity will further increase demand, with forecasts ranging from 3 to 5 percent per year until 2050.

CO_2 emissions are the best understood and most prevalent way to measure the climate impact of aviation today, but aircraft also emit nitrogen oxides (NO_x), water vapour, and soot at high altitudes. Despite the uncertainties, it is evident that non-CO_2 emissions effects are significant contributors to global warming. For kerosene aircraft, the total effect could be anywhere between two to four times as large as the impact from CO_2 emissions alone. Another important factor in evaluating the impact of emissions on climate is the residence time of each emitted species type. The residence times depend on the latitude and flight altitude, which is a function of the flight speed. For example, for a given altitude and latitude, the residence time of CO_2 is at least one order of magnitude higher than the one of water vapour.

Decarbonizing aviation requires the development of new fuels and propulsion technology. First, continuous improvement in aircraft and propulsion efficiency can

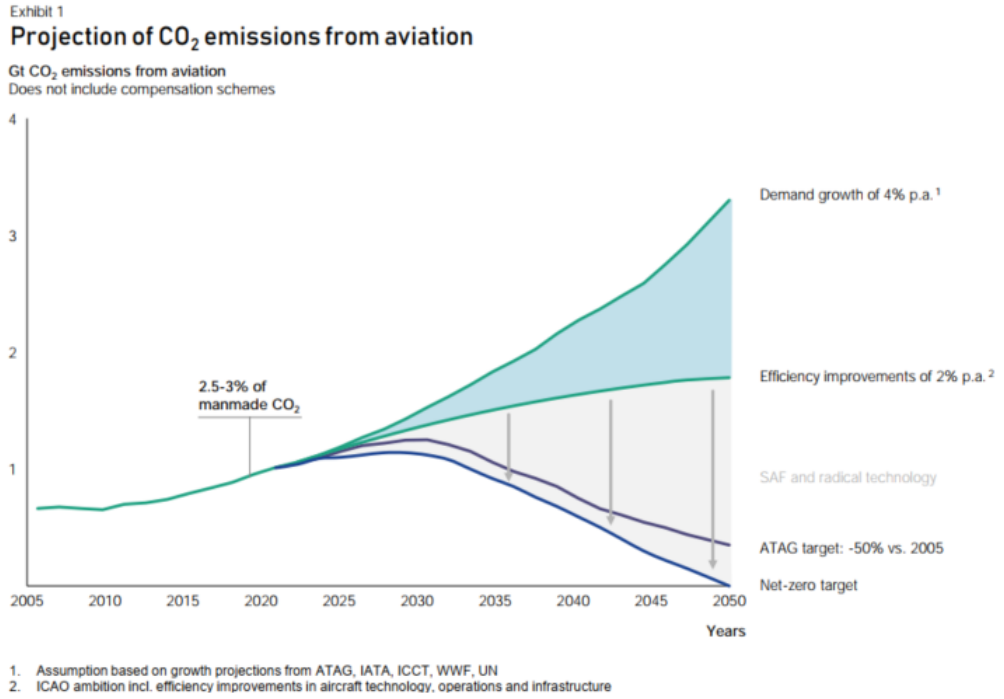

Fig. 2.5 Projection of CO_2 emissions from aviation [14]

be foreseen, but cannot compensate for the sector growth, which is expected to be greater than the efficiency improvement rate. A second possibility is to change the energy carrier, shifting to a more sustainable one. Possible solutions are to move towards different fuel types, such as Sustainable Aviation Fuels (SAF) or Hydrogen. SAF are fuels which are derived from sustainable feedstock. For example, they can be derived from biomass or waste, or they can be produced after a synthesis process from feedstock or biomass. The main advantage of biofuels is the possibility to use them as "drop-in fuels", which do not need any modification in aircraft or fuel infrastructure. However, the availability of feedstock, change in land use, high water use, and/or monoculture are challenging aspects which could lead to the competition between aviation industry and other sectors which exploit the feedstock for other purposes. Moreover, the reduction of non-CO_2 effects could be limited. Various states and organizations have established targets for SAF production. For example, the European Commission aims for increasing the amount of SAF in the following decades (32% SAF by 2040 and 63% by 2050) [15], but the current availability of SAF represents less than 0.1% of global aviation fuel consumption [16]. To meet the projected supply by 2050, a huge increase in production should be achieved, and the immediate increase in SAF production is expected to originate from biomass.

However, these type of feedstocks (first-generation biofuels), including crops like corn, oil palm, soy, or sugarcane, have been associated with increased food costs and a variety of detrimental environmental effects [16]. For that reason there is a wide demand for governmental regulations to prioritize the utilization of highly productive soils in the food industry, given the rapid growth of the global population and increased food demands [17]. The emergence of second-generation biofuel feedstocks, which do not depend on sugar or oil-rich crops and are not reliant on soil quality, presents a potential solution to mitigate land use challenges. However, it may still impose constraints on water accessibility for the cultivation of food crops [18]. A further possibility are fuels based on algae (third-generation biofuels), which have a significantly higher biomass productivity per area than plants and do not compete with food and land supplies. However, despite showing significant potential, certain limitations hinder the commercialization of third-generation biofuels, such as the higher production costs with respect to the other types of fuel. Considering the potentially significant role of algal biofuels in mitigating carbon emissions by 2050, futrther advancements in third-generation biofuel production are required.

The exploitation of hydrogen as a fuel could lead to a potentially high reduction of climate impact. First, differently from biofuels, it does not contain any carbon and does not produce any CO_2 in flight. For what concerns the other emission types, NO_x emissions can be reduced with respect to kerosene aircraft if $LH2$ is used. Moreover, considering the advancement in propulsion technology, and especially combustor design this type of emissions can be reduced up to the 90% [19]. The production of NO_x is influenced by both the residence time and combustion temperature. Hydrogen exhibits a higher flame speed compared to kerosene, resulting in quicker combustion and thus reduced residence times, which in turn leads to lower NO_x emissions and shorter combustors. Assuming full mixing of the hydrogen-air mixture, the reduced flame temperature during lean combustion mitigates NO_x production. However, inadequate mixing can lead to hot spots in areas where air and fuel reach stoichiometric conditions, thus generating NO_x. Techniques to enhance mixing intensity without pre-mixing fuel and air are essential for facilitating low-NOx hydrogen combustion. [20]

The amount of emitted water vapour, instead, is much higher in case hydrogen is used as a fuel, and its perturbation time strongly depends on the altitude at which it is emitted [21]. As can be seen in Figure 2.6, lifetime at altitudes below 12 km ranges from 1 hour to 6 months. Moreover, the lifetime is longer at high altitudes

and lower latitudes. In case of high-speed aircraft, which fly in the upper part of the troposphere and/or at stratospheric altitudes, the lifetime is increased up to 5.5 years, having an increasing impact on the climate.

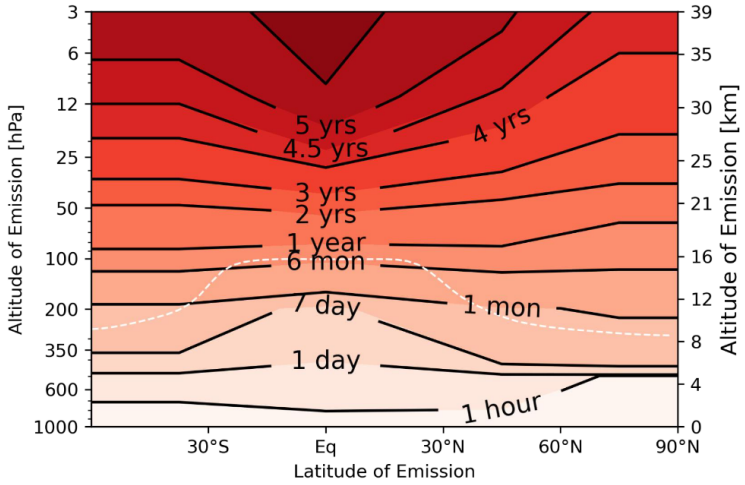

Fig. 2.6 Water vapour lifetime for different altitudes and latitudes [21]

Hydrogen can be produced directly from renewable energy, and its production cost is expected to decrease in the near future. However, the volume required to store the hydrogen on-board is much higher than for the kerosene, despite its higher energy density. This means that it cannot be used as a drop-in fuel, and indeed the aircraft should be adapted accordingly. Moreover, for longer ranges, the use of hydrogen could become unfeasible or limited, due to the very high volume requirements for storage on-board.

Additionally, together with the impact on climate, the aircraft noise, pollutant emissions and sonic boom should also be considered when designing an environmental sustainability aircraft. These three aspects are described in the following sections.

2.3.2 Aircraft noise

Aircraft noise at airport level is one of the most critical issues to address in the design of a new concept. The primary objective is to ensure that the airframe, engine, and overall aircraft performance are such that the aircraft complies with the community noise level standards established by regulations. While crucial for subsonic aircraft,

accomplishing this becomes even more challenging for high-speed aircraft due to significantly higher noise levels generated during take-off and landing phases. Noise regulations for subsonic aircraft are reported in the ICAO Annex 16, Vol. I [22]. More precisely, the certification noise levels are linked to three distinct operational conditions, which are physically indicated by a reference measurement point on the ground [23], as shown in Figure 2.7:

- Sideline-maximum power condition, where the measurement point is positioned along a line parallel to the runway centreline at a distance of 450 m, where the noise level peaks during take-off. This scenario is associated with the sideline measurement, representing the maximum sound level along the lateral full-power line.
- Flyover-intermediate power condition, where the measurement point is situated along the extended runway centreline, 6500 m from the start of the roll.
- Approach-low power condition, where the measurement point is placed 120 m vertically beneath the 3-degree descent path, which starts from a point located 300 m beyond the threshold.

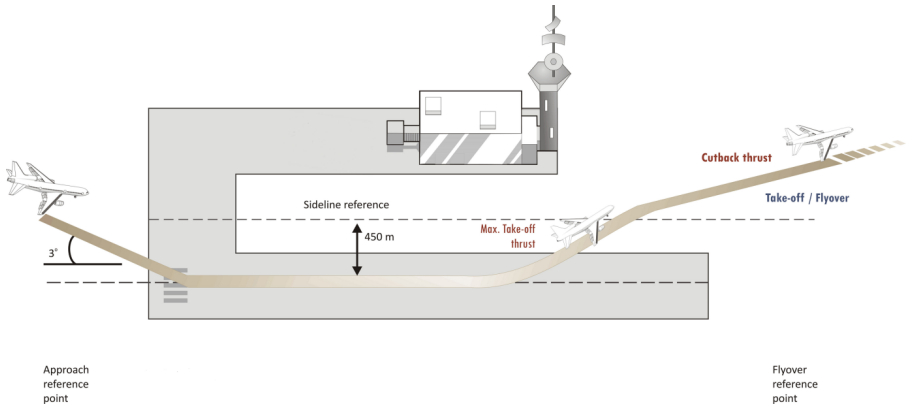

Fig. 2.7 Aircraft noise certification reference measurement points [24]

Due to the introduction of the Concorde in 1976, specific regulations for supersonic aircraft were added in 1981, but they only imposed to not exceed the noise levels of the Concorde. However, given the absence of subsequent high-speed aircraft following the Concorde, these regulations cannot be directly transposed onto new aircraft designs. Instead, they should serve as a valuable reference for establishing

updated requirements [5]. One crucial prerequisite for future supersonic concepts is the incorporation of cutting-edge technologies and flight procedures focused on minimizing noise, not only during en-route phases but also for Landing and Take-Off - LTO operations. Additionally, verifying noise emissions from the initial phases of the design process is the most effective approach to ensuring that forthcoming supersonic aircraft adhere to low-noise standards [23]. At the same time, it is important to highlight that an ad-hoc redefinition of noise regulations will be required. For that reason, the high-speed aviation community is putting great efforts in supporting the possible updates on those regulations for supersonic aircraft. For example, currently two different EU funded projects are focusing on noise and emissions of supersonic aircraft during the LTO cycle: the More&Less project (see subsection 2.5.2) and the SENECA ((LTO) noiSe and EmissioNs of supErsoniC Aircraft) project [25].

2.3.3 Pollutant emissions

The limit levels for pollutant emissions of subsonic aircraft are reported in the ICAO Annex 16, Vol. II [26]. Currently, the following species are regulated for subsonic aircraft [5]:

- Nitrogen Oxides (NO_x);
- Carbon monoxide (CO);
- unburned Hydrocarbons (HC);
- Non-volatile particulate matter (nvPM);
- Fuel venting.

It is also interesting to highlight that CO_2 emissions are not included within this list, since CO_2 contributes to climate change, but it does not have an impact on air quality. For each of the specified pollutants, emissions are assessed throughout a standardized LTO, which consists of various operational modes characterized by specified durations and engine thrust settings. Moreover, the air quality standards are directly referred to engines and not to a specific aircraft type, as it happens for noise and CO_2 emissions. Similarly to what happened for the aircraft noise, the pollutant emissions were not regulated for high-speed aircraft when the Concorde came into

service. So, the limits on emissions were tailored specifically on this aircraft, and modified LTO procedures were introduced. However, those regulations have not been updated after early 1980s and are now outdated, since they cannot reflect the most recent advancements in combustion technology, or the current understanding of environmental needs and the advanced supersonic concepts [27].

2.3.4 Sonic boom

An additional aspect to consider when dealing with high-speed aircraft is the sonic boom. It becomes relevant when an aircraft flies at supersonic and hypersonic speeds, since it is associated to the shock waves generated by the aircraft flying at velocities greater than the speed of sound. In these conditions, the aircraft is surrounded in the near field by a complex pattern of shock waves and expansion areas [27]. In particular, three flow regions Figure 2.8, which are usually named as “near,” “mid,” and “far fields, can be identified, when evaluating the sonic boom signature on ground of an aircraft flying at high altitudes. The three zones are delimited along the stream-wise direction by the bow and tail shocks. While an exact definition of the vertical span of each flow region presents challenges, it is possible to characterize the regions based on their aerodynamic structure [28].

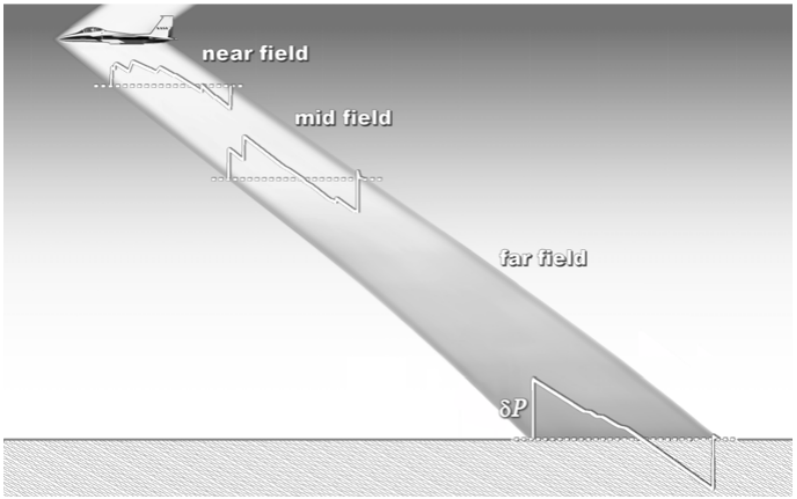

Fig. 2.8 Sonic boom propagation [28]

The near field is typically limited to few body lengths from the aircraft, and it is characterized by a nonlinear behaviour, with intense stream-wise gradients

in velocity and pressure and shocks originating from the aircraft. The midfield, considerably larger than the near field, serves as the transitional zone between the near and far fields. The far field, generally the most extensive of the three regions, is where the waveform of the signature reaches its asymptotic state. This state is commonly represented by an N-wave. Since the effect of those waves can propagate over long distances and reach the ground, they can have negative effects on people and buildings. For that reason, the flight of supersonic vehicles over land is currently forbidden [5]. However, even if the effects of sonic boom cannot be completely avoided, it can be possible to mitigate this impact and reduce the sonic boom to acceptable levels, following a low-sonic boom targeted aircraft design. Eventually, it is clear that a re-definition of the present regulations in terms of sonic boom restrictions is needed in the near future, considering the technological advancements on this field.

2.4 An overview of past and future high-speed concepts

The main aim of this section is to present an overview of the major activities for the design of high-speed transportation systems, which have been studied and/or developed in the past, considering both historical and technological perspectives. In particular, the section is divided into two different subsections: the first one (subsection 2.4.1) is dedicated to the supersonic concepts, while the second one illustrates hypersonic vehicles concepts (subsection 2.4.1).

2.4.1 Supersonic concepts

The very first aircraft capable of exceeding the speed of sound was the **Bell X-1** (Figure 2.9). Initially named XS-1, it was designed within a joint program by National Advisory Committee for Aeronautics (NACA) and U.S. Air Force to develop special manned transonic and supersonic research aircraft. Indeed, this kind of vehicles were the first to be built for experimental purposes only, creating the concept of research aircraft [29]. It completed its first historical flight on 14 October 1947, piloted by Captain Charles E. “Chuck” Yeage, reaching a maximum

speed of Mach 1.06 at an altitude of approximately 13700 m [30]. A Boeing B-29 Superfortress was exploited to perform an air launch of the X-1, which was released at an altitude of 6000 m. It was powered by the XLR-11 liquid oxygen and ethyl alcohol rocket engine.

Fig. 2.9 Bell X-1

The Bell X-1 aircraft had a pioneering role in introducing and validating numerous structural and aerodynamic advancements, such as thin and strong wing sections, supersonic fuselage configurations, and innovative control system designs [30].
A second generation of X-1 aircraft followed, characterized by a longer cylindrical fuselage, reaching the maximum length the carrier aircraft could allow [31]. Moreover, a low-pressure turbo-pump was introduced, which allowed for larger tanks within the fuselage. Four aircraft were supposed to be built (X-1A, X-1B, X-1C, X-1D), but only the first two were actually completed. The main objective was to double the Mach number of the first aircraft's generation. This condition was reached on 12 December 1953, when Maj. Charles E. "Chuck" Yeager reached Mach 2.44 at an altitude of 22600 m on board of the X-1A. However, the aircraft started to roll soon after, tumbling out of control and making the pilot unconscious. He then revived at an altitude of 9000 m, being able to recover and land back.

However, the first aircraft capable of reaching the Mach 2 speed, was the **Douglas D-558-II "Skyrockets"** (Figure 2.10), which performed its historical flight few weeks before the X-1A on the 20 November 1953. It was designed almost in parallel with the X-1, by NACA and the US Navy, which pushed to purse a more conservative design with respect to the X-1. Three different aircraft were built, which flew a total of 313 flights, and contributed to collect a large amount of data on the coupling of

lateral and longitudinal motions, loads generating on wing and tail, and lift and drag characteristics of swept-wing aircraft in transonic and supersonic regime [32].

Fig. 2.10 Douglas D-558-II "Skyrockets"

The **Convair B-58 Hustler** (Figure 2.11) was the first production supersonic bomber to reach Mach 2 and was operated from 1962. It was characterized by a very innovative design features, such as the thin delta wing, the fuselage designed according to the area rule and the use of honeycomb sandwich construction [33].

Fig. 2.11 Convair B-58 Hustler

At the same time, during the 1950s, the Soviet Union was also analysing the possibility to design a supersonic aircraft. They developed the **Mikoyan-Gurevich MiG-19** (Figure 2.12), that became the first supersonic jet fighter to be mass-produced from 1955. It was capable of accelerating up to a maximum speed of Mach 1.35 and to cover a maximum range of 1390 km.

Fig. 2.12 Mikoyan-Gurevich MiG-19

The research on supersonic aircraft was also active in Western Europe, where France was the first nation to build an experimental aircraft capable of reaching supersonic velocities. The **Nord Gerfaut** (Figure 2.13) was a delta wing experimental research aircraft with a maximum Mach number of 1.13 at 10800 m [34]. It was able to reach Mach 1 in level flight without the use of an afterburner, and performed its first successful flight in 1954. The **Dassault Super Mystère** (Figure 2.14), instead, was the first European supersonic fighter jet to be mass-produced.

Fig. 2.13 Nord Gerfaut

Fig. 2.14 Dassault Super Mystère

The next speed record was established by the **Lockheed SR-71 "Blackbird"** (Figure 2.15), a long-range, high altitude strategic reconnaissance aircraft developed by Lockheed corporation, which was able to reach Mach 3. It was secretly designed from late 1950s, and it completed its first flight on 22 December 1964 [35].

Fig. 2.15 Lockheed SR-71 "Blackbird"

It was designed to cruise at Mach 3.2 up to an altitude of 26000 m. The challenging operational conditions in which these aircraft operated made them exceptional platforms for conducting research and experiments across various disciplines. These included aerodynamics, propulsion, structures, thermal protection materials, high-speed and high-temperature instrumentation, atmospheric studies, and the characterization of sonic boom. It was equipped with two Pratt and Whitney J58 axial-flow turbojets with afterburners. However, at high speeds the engine worked as a ramjet, with the air entering the inlet that was bypassed and went directly to the afterburners and nozzles [35].

The **XB-70 Valkyrie**, shown in Figure 2.16, was an ambitious prototype American supersonic strategic bomber, with a designated cruise Mach of 3 and an operating altitude of 21000 m. It is characterized by a delta wing and a slab-sided fuselage, which included the six jet engines that powered the aircraft [36]. The wing has an outer movable part which is maintained in a horizontal position for take-off, landing and subsonic flight, in order to increase the lift generated by the aircraft. At supersonic speed, instead, the wing tips are folded downward, as can be seen in Figure 2.17, so that their interaction with the shock wave could be avoided. Moreover, two canards are also included, to guarantee enough control.
However, at the time there was a general belief that manned bomber was obsolete and, for that reason, the project was ended early. Nevertheless, during the same period the interest towards SST was growing fast, in an attempt to dramatically reduce the flight times. For that reason, given the characteristics of the XB-70 Valkyrie, the idea that it could have been used a perfect test-bed for research on supersonic transport research was also considered.

Fig. 2.16 XB-70 Valkyrie at take-off

Fig. 2.17 XB-70 Valkyrie in supersonic flight configuration

As presented before, by the end of 1950s and early 1960s lots of different supersonic military jet aircraft were studied and designed. At the same time, the initial fleet of long-range, high-subsonic jet airliners had recently entered service. Then, the idea of having supersonic transport was soon becoming increasingly attractive, with the main aim of developing economically feasible aircraft and drastically reduce the flight time, so that supersonic transport could become attractive to a large segment of the passenger market [37]. The commercial viability of supersonic flight underwent under examination in the four nations that contributed the most to their development: France, UK, USA, and USSR [27].

For example, in the USA the same companies that developed the supersonic military aircraft in the previous years, such as the B-58 Hustler and the XB-70 Valkyrie, also focused on supersonic passenger transport, with direct government sponsorship. Boeing and General Electric were selected to develop a supersonic passenger airliner, the Boeing 2707 (Figure 2.18), capable of hosting up to 300 passengers and with a cruise speed of Mach 3. However, due to economic, environmental and political reasons, the project was ended in 1971 [27].

The development of a supersonic transport aircraft was going on also in Europe, where a consortium between the British Aircraft Corporation (BAC) and the French Aérospatiale begin the development of the Mach 2 Concorde (Figure 2.19) in 1962. It was operative from the 1960s until its final flight in 2003. The Concorde represented a pinnacle of aviation technology, featuring a slender ogive delta wing design and four Rolls-Royce Olympus 593 turbojet engines plus afterburner. To improve the propulsive performance at each Mach number variable geometry intake and

Fig. 2.18 Boeing 2707 SST

nozzle were introduced. Since it was capable of cruising at Mach 2, the Concorde significantly reduced travel time on transatlantic routes, completing a journey from New York to London in about three hours. The aircraft's cutting-edge engineering included a droop-nose mechanism, which lowered during take-off and landing to enhance visibility for pilots. Despite its technical accomplishments, the Concorde faced challenges, including high operational costs, limited range, and noise restrictions, leading to its retirement from commercial service. The Concorde remains an iconic symbol of aerospace innovation, showcasing the possibilities and challenges associated with supersonic passenger transportation.

Fig. 2.19 Concorde

However, it was the Tupolev Tu-144 (Figure 2.20) to be the first commercial airliner to exceed Mach 2, developed by Tupolev in USSR. It made its first flight in December 1968, just a few months before the Concorde, of which it shared a

similar delta-wing configuration and a slender fuselage. Despite its technological achievements, the Tu-144 experienced setbacks, including a tragic crash at the 1973 Paris Air Show, hindering its reputation. Additionally, the Tu-144 had a shorter commercial service life than the Concorde, with operations ceasing in 1978. The Tu-144's legacy lies in its contribution to early supersonic aviation and its role as a symbol of the intense competition during the Cold War-era race for supersonic passenger travel.

Fig. 2.20 Tupolev Tu-144

Since the retirement of the Concorde, there has been a persistent interest in developing a second-generation supersonic aircraft within the aviation industry. Various conceptual designs have emerged, driven by advancements in technology and a renewed focus on addressing the challenges that affected the Concorde's commercial success. These concepts prioritize improvements in fuel efficiency, sonic boom reduction, and enhanced passenger comfort, often incorporating cutting-edge materials and propulsion technologies. The ongoing pursuit of a second-generation supersonic aircraft underscores the industry's commitment to overcome past limitations and ushering in a new era of efficient and sustainable high-speed concepts.

Notable among these concepts is the Boom Overture (Figure 2.21), by Boom Supersonic, a modern supersonic aircraft with a focus on fuel efficiency and reduced sonic boom impact to allow supersonic flight over land.

Fig. 2.21 Boom Overture

The Overture is designed to accommodate between 65 and 88 passengers and achieve speeds of approximately Mach 1.7, dramatically reducing travel times on long-haul routes up to 7870 km of range. The aircraft's aerodynamic design features a slender delta wing, optimized to enhance performance at high speeds, and it is equipped with four medium by-pass turbofan engines without afterburner, using only 100% sustainable aviation fuel (SAF) [38]. Boom Supersonic places a strong emphasis on mitigating the sonic boom, a characteristic associated with supersonic flight, through advanced aerodynamic shaping and innovative design choices.

Another example is the Spike Aerospace S-512 supersonic business jet (Figure 2.22), intended to accommodate up to 18 passengers. The aircraft's design includes a slender window-less fuselage, optimized wings, and distinctive engine nacelles, all contributing to enhanced aerodynamic efficiency.

NASA is also working on a new supersonic concept in collaboration with Lockheed Martin, the X-59 Quesst, which is an experimental low-boom supersonic aircraft, shown in Figure 2.23. It is designed to cruise at Mach 1.42 at an altitude of 16800 m, creating a low boom (75 Perceived Level decibel (PLdB)), to evaluate supersonic transport acceptability. NASA is targeting to perform the first flight tests on 2024 [39].

Fig. 2.22 Spike S-512

Fig. 2.23 X-59 Quesst

2.4.2 Hypersonic concepts

In parallel to the research on supersonic concepts, the aviation world has also been always interested in developing hypersonic concept. For that reason, this section is dedicated to the analysis of the different hypersonic vehicles which have been designed or are currently studied within the world. In particular, the first part contains some details of the vehicles designed in the United States, then a description of the studies carried on outside the US is presented, while the last part focuses on the hypersonic research activity conducted in Europe.

Hypersonic concepts research in the USA

The very first example of human hypersonic flight is represented by the **X-15** (Figure 2.24), which was designed from 1954 by United States Air Force and the National Aeronautics and Space Administration (NASA), to demonstrate that controlled human flight with rocket-powered vehicles out of the Earth's atmosphere was possible. During the first part of the mission, the X-15 vehicle was carried by a B-52 aircraft. Then, once it was released, its rocket engines were able to provide thrust to reach an altitude of 100 km and a maximum speed of Mach 6.7. The ability to perform atmospheric re-entry and landing at a specific location was also demonstrated. A total of 199 flights were conducted with 3 different X-15 vehicles, which contributed to investigate the different aspects of human hypersonic flight and served as a fundamental basis for the development of the next piloted spaceflight programs (such as Mercury, Gemini, and Apollo) as well as the Space Shuttle program [40].

Fig. 2.24 X-15

The X-15's success laid the groundwork for exploring new concepts for hypersonic flight. The **X-20 Dyna-Soar** vehicle (Figure 2.25) is one of the main examples: it was initially conceived as a high-speed manoeuvrability test aircraft but was later designed to support various military missions, such as bombing, aerial reconnaissance, space rescue, and satellite maintenance. It was designed as a reusable winged spaceplane, that could be operated both as an unmanned vehicle and a piloted one. Additionally, the design of the vehicle incorporated the possibility of dynamic soaring, aiming to showcase atmospheric skipping and hypersonic glide at high altitudes. The program however, was cancelled by the US government before the vehicle's production started.

Fig. 2.25 X-20 Dyna-Soar

Despite the closure of the X-20 program, the period between 1960 and 1970 witnessed a growing demand within the scientific community for advancing technologies essential to high-speed applications. A wide number of lifting body configurations were designed and studied in this period, focusing especially on the aerodynamic characterization. Two examples of this type of concepts are the **X-23** (Figure 2.26) and **X-24** (Figure 2.26) vehicles. The X-23 was designed to study the manoeuvrability during the high-speed flight in atmospheric reentry, while the X-24 was created to study the low-speed manoeuvrability of a high-speed vehicle, demonstrating the ability to perform precision landing on a runway [30].

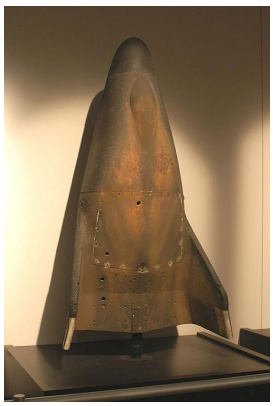

Fig. 2.26 X-23

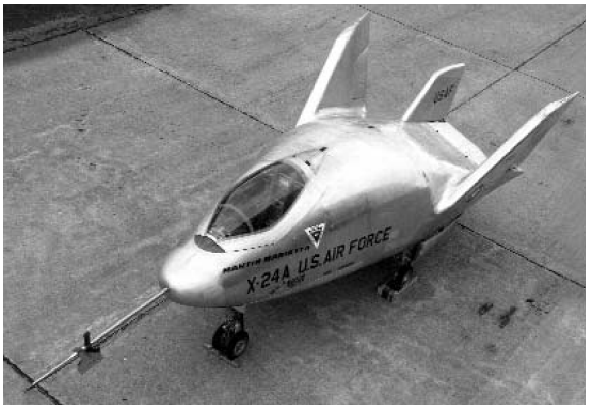

Fig. 2.27 X-24

Another significant advancement took place from the 1970s, leveraging the expertise gained from X-vehicles in the USA to initiate the development of the Space Shuttle (Figure 2.28). This spacecraft successfully entered orbit in 1981 and remained operational with success until 2011 [41].

Fig. 2.28 Space Shuttle Atlantis at landing

A further step in demonstrating the viability of sustained hypersonic flight and to reach low Earth orbit without the use of a rocket is represented by the National Aero-Space Plane (NASP) project [42]. Figure 2.29 shows the **X-30**, which is the experimental vehicle that has been studied within this project. Even if the program was cancelled in 1990 due to cost and technical difficulties, it still provided the aerospace community with valuable knowledge about hypersonic propulsion, aerodynamic and thermal protection system.

Fig. 2.29 X-30 vehicle

Moreover, the NASP program paved the way for subsequent air-breathing hypersonic aircraft concepts, such as the X-43. The **X-43A** vehicle is a pioneering hypersonic unmanned aircraft designed for atmospheric flight at speeds greater than Mach 5. Figure 2.30 and Figure 2.31 show an illustration of this vehicle, together with the main configuration data (expressed in inches). Developed within NASA's

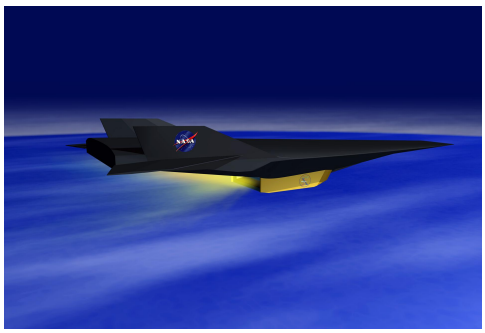

Fig. 2.30 X-43A illustration

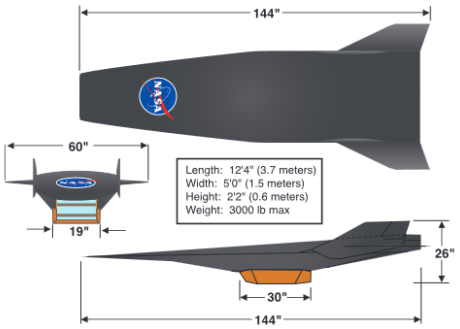

Fig. 2.31 X-43A vehicle configuration

Hyper-X program, the X-43A is equipped with an air-breathing scramjet engine, enabling it to efficiently operate within the hypersonic regime, where traditional

jet engines are inefficient. To reach the test altitude and speed, the vehicle is first carried up to 4000 ft by a NASA Dryden B-52B aircraft, and then an expendable booster rocket accelerates the vehicles up to the test conditions. From this point, the X-43A is in free flight conditions and the scramjet engine can be activated [43]. An overview of the trajectory is reported in Figure 2.32.

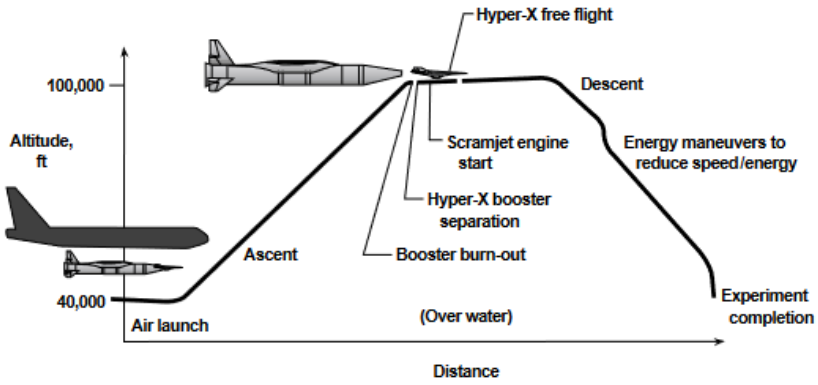

Fig. 2.32 X-43A mission concept

NASA made aviation history completing the first two successful flights using a vehicle equipped with a scramjet engine and flying at hypersonic speeds [43]. The first flight was performed in March 2004, reaching an altitude of 29 km at a maximum Mach number of 6.83, when the scramjet was operated for a total time of 11 s. The second flight, instead, reached a higher altitude of 34 km and a Mach number of 9.68. The vehicle played a pivotal role in expanding the understanding of hypersonic flight, as well as in validating key propulsion and related technologies for air-breathing hypersonic unmanned aircraft, contributing to provide valuable data for the development of future aerospace technologies. The X-43A's successful missions mark a significant leap forward in the exploration of hypersonic flight, with potential applications ranging from rapid space access to advanced military capabilities and efficient global transportation systems.

The **X-51A** (Figure 2.33) is another example of unmanned scramjet demonstrator vehicle, which was designed by United States Air Force within the WaveRider program, and equipped with a scramjet engine developed by Pratt & Whitney Rocketdyne. The primary goal of the X-51A program was to validate the performance of a scramjet engine utilizing endothermic hydrocarbon fuel. This involved accelerating the vehicle to hypersonic speed, after being carried by a Boeing B52 to the necessary

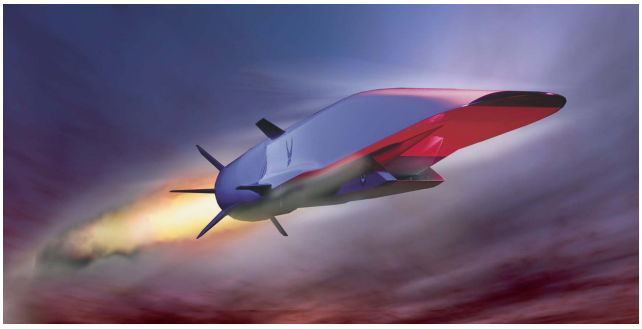

Fig. 2.33 X-51A waverider vehicle

altitude and speed conditions for initiating the engine. Four X-51A vehicles were constructed and flown, but only the fourth and ultimate X-51A flight was successful on 1st May 2013 [44]. The X-51A vehicle reached a maximum speed of Mach 5.1 at an altitude of 18 km, while the scramjet engine was operated for a total of 240 s.

Moreover, it is worth citing Virgin Galactic, a commercial space company which is currently providing suborbital space tourism services, exploiting two vehicles: the SpaceShipTwo and the WhiteKnightTwo. The latter is a four air-breathing jet engine and dual fuselage aircraft, which serves as a carrier for the SpaceShipTwo spacecraft, that is released at an altitude of 15 km. After the separation, the engine of the SpaceShipTwo is activated to reach a maximum altitude of 110 km, while the WhiteKnightTwo starts its descent towards the landing site [45]. At the moment, however, the SpaceShipTwo is able to reach altitudes slightly lower than 90 km. Figure 2.34 shows the SpaceShipTwo underneath its carrier aircraft, the WhiteKnightTwo.

Fig. 2.34 SpaceShipTwo underneath its carrier aircraft the WhiteKnightTwo

Hypersonic research outside the US

Outside the United States different projects have also investigated the possibility to design a hypersonic vehicle. For example, the Japanese Aerospace Exploration Agency (JAXA) is working on the development of an environmentally friendly Mach 5 passenger aircraft with reduced sonic boom and noise pollution. The vehicle concept is reported in Figure 2.35. It is designed to host up to 100 passengers along a reference trajectory between Tokyo and Los Angeles. It is provided with pre-cooled turbojet engines and ramjet [46], exploiting liquid hydrogen as propellant. Moreover, aerodynamic and propulsion tests have been carried out to validate the concept.

Fig. 2.35 JAXA Mach 5 concept

Another hypersonic concept is the Brazilian **14-X** Aerospace Vehicle, which is a technological demonstrator developed to test waverider and scramjet technology [47]. An overview of the vehicle is reported in Figure 2.36.
A two stage rocket is supposed to be used to accelerate the vehicle up to the desired altitude and Mach number to test the scramjet engine. The first test of the 14-X scramjet engine was conducted in 2021, when the demonstrator was released at an altitude of 30 km and a Mach number close to 6.

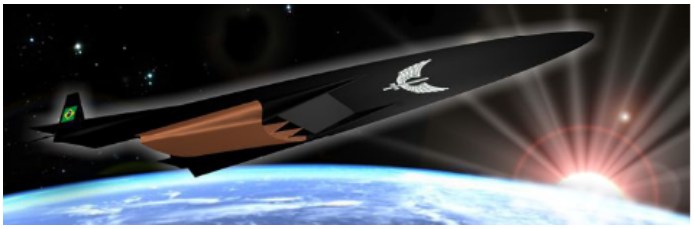

Fig. 2.36 14-X Hypersonic Aerospace Vehicle

European activity on hypersonic concepts

Eventually, it is important to highlight the European contribution to the development of hypersonic concepts and technologies. A first example of hypersonic concept designed in Europe is the **HOrizontal Take Off and Landing (HOTOL)** vehicle Figure 2.37, which was studied by British Aerospace in 1980s. It was a single stage to orbit winged vehicle, capable of performing horizontal take-off and landing from conventional runways. It would have been powered with a Rolls-Royce RB454 combined air-breathing/rocket cycle engine, which could operate in air-breathing mode up to Mach 5.5 and as a rocket for the higher speeds. The project, however, ended early due to lack of funding from UK governments.

Fig. 2.37 HOTOL

In the same period, also Germany approved a hypersonic project within the Hypersonic Technology Program, where the **Sänger II** concept was designed (Figure 2.38). It is intended as a two-stage space transportation system with turbo-ramjet propulsion [48], capable of performing horizontal take-off and landing from European airports. A description of its reference mission is reported here. The acceleration phase is completed using turbojets up to an altitude of 10 km. Then, thanks to the use of afterburners the vehicle can accelerate to supersonic speeds. At Mach 3.5 the ramjet propulsion is activated, and the vehicle performs a cruise phase at Mach 4.4 and an altitude of 25 km. Later, the altitude of 31 km is reached at Mach 6.8, prior to the stage separation which occurs at 35 km. The second stage's rocket engine are now activated to reach the desired orbit. The vehicle is then able to perform the reentry and landing. Moreover, the second stage was supposed to be both a cargo or passenger vehicle, depending on the mission type. However, in 1990s the project was also cancelled due to high cost.

Fig. 2.38 Sanger II

SpaceLiner (Figure 2.39) [49] is another example of hypersonic project which is under design at DLR, Germany. It is a two-stage hypersonic winged passenger vehicle that is supposed to fly along ultra-long haul distances, for example connecting Europe and Australia in 90 min.

Fig. 2.39 SpaceLiner

Looking at these examples, it is worth noticing that the hypersonic research in Europe was limited to independent national research initiatives up to the end of the 1990s. From 2000s, instead, the European aerospace community started to work together on high-speed propulsion and concepts.

One of these initiatives is the **Long-term Advanced Propulsion Concepts And Technologies (LAPCAT)** project, which has been funded by the European

Commission in the field of the sixth European Framework Program (FP6). This was the first example of a joint multidisciplinary work in the European Union on high-speed concepts. The project's main focus was on the analysis of two different types of engines: Turbine-Based Combined Cycles (TBCC) and Rocket-Based Combined Cycles (RBCC) engines. The assessment of critical technologies relative to engine and aircraft integration, as well as engine components and combustion has been also performed. The main outcome of this project are three vehicle concepts [50]:

- a hydrogen Mach 5 cruiser (Figure 2.40), designed with a wing-body configuration to host up to 300 passengers on-board, along antipodal routes with a maximum range of 18700 km; The total length of the vehicle is equal to 139 m and the fuselage diameter is 7.5 m. The total wing span is equal to 41 m. It is equipped with 4 Scimitar pre-cooled engines [51], which allow to cover the entire Mach range during the reference mission. Both the vehicle and the engine have been designed by Reaction Engines Ltd. (REL);
- a kerosene Mach 4.5 cruiser for 200 passengers, which was studied by DLR to evaluate the performance of kerosene as a fuel instead of hydrogen, since it has a supply infrastructure that is already available;
- a hydrogen Mach 8 cruiser (Figure 2.41) with a rocket-based combined cycle.

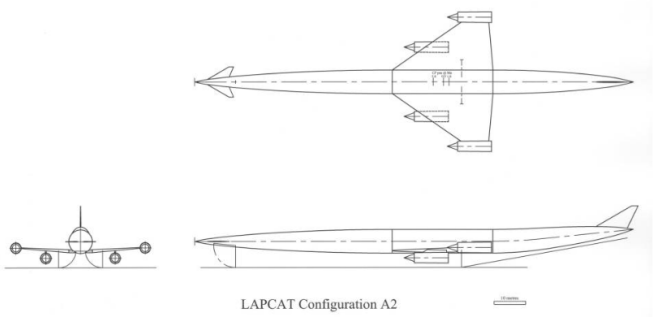

Fig. 2.40 LAPCAT A2 Mach 5 cruiser [50]

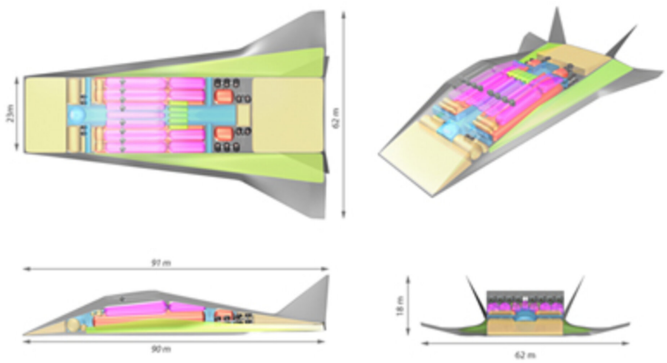

Fig. 2.41 LAPCAT A2 Mach 5 cruiser [50]

In the same period, the **Aerodynamic and Thermal Load interactions with Lightweight Advanced materials for high-Speed flight (ATTLAS)** project has also been funded under the sixth European Framework Programme (FP6), to investigate all the aspects of low hypersonic flight (from Mach 3 to Mach 6) related to material technology, aero-thermodynamics, sonic boom and aircraft performance. For example, the first concept to be analyzed was a kerosene based Mach 3.5 vehicle (called M3T), designed to host 200 passengers and to cover a maximum range of 10000 km [52], The Mach 6 concept [53], instead, was intended to host up to 200 passengers and to fly along routes with a maximum range of 7000 km.

The **Long-term Advanced Propulsion Concepts And Technologies II (LAPCAT - II)** project [54][55], which was the follow-up of the previous LAPCAT project, started in 2008 and was completed in 2013. The primary objective of LAPCAT-II was to further study two of the concepts designed within LAPCAT. The first one is the Mach 5 concept (LAPCAT-II A2, Figure 2.42), which is directly derived from the vehicle developed by REL. For what concerns the LAPCAT A2 Mach 5 vehicle, a detailed design of all the main components of the propulsion system has been carried on, which consists in a pre-cooled turbofan/ramjet engine (called SCIMITAR and developed by Reaction Engines). Both numerical and experimental analyses have been carried on to assess the performance of the intake, combustor and nozzle.

Fig. 2.42 LAPCAT-II A2 vehicle concept

The second one is the Mach 8 cruise concept (LAPCAT-II MR2.4, Figure 2.43), which is a waverider vehicle exploiting hydrogen as fuel. The vehicle has a total

Fig. 2.43 LAPCAT-II MR2.4 vehicle concept

length of 94 m and a wingspan of 41 meter [56]. It is equipped with a dorsal-mounted air breathing propulsive plant, with the intake, combustor and nozzle that are placed along the entire vehicle length. Moreover, it was equipped with two different engine types:

- the first one is used for the low-speed operations up to Mach 4.5, and is composed of six Air Turbo Rocket (ATR);
- the second one is a Dual Mode Ramjet (DMR), that is used for the higher Mach numbers up to Mach 8.

The LAPCAT-II vehicle is supposed to cruise at Mach 8 at an altitude of 33 km, covering a total maximum range of 18700 km. Both numerical methods and experimental tests were conducted during the research activity. Different analysis have been performed, such as nose-to-tail CFD, aerodynamic characterization and stability

analysis, combustor modelling, mission analysis, emissions estimations, and thermal control and protection subsystem sizing.

A direct successor of the LAPCAT-II project was the **High-Speed Experimental Fly Vehicles (HEXAFLY project)** [57], that was funded within the seventh European Research Framework Programme (FP7) in 2012. The project's main focus was on the development of an experimental high-speed vehicle, with the aim of advancing the Technology Readiness Level (TRL) of critical technologies studied during ATLLAS and LAPCAT projects. Six main area of interest have been investigated within the HEXAFLY project [58]:

- High-speed vehicle concepts;
- High-speed aerodynamics;
- High-speed propulsion;
- High-temperature materials and structures;
- High-speed flight control;
- High-speed environmental impact.

Moreover, three different vehicle architectures have been selected (Figure 2.44): the first one is a free-flight Experimental Flight Test Vehicle (EFTV), the second one is a vehicle mounted on the LEA platform, and the last one is a captive-carry test using a small scale vehicle launched on a sounding rocket [58].

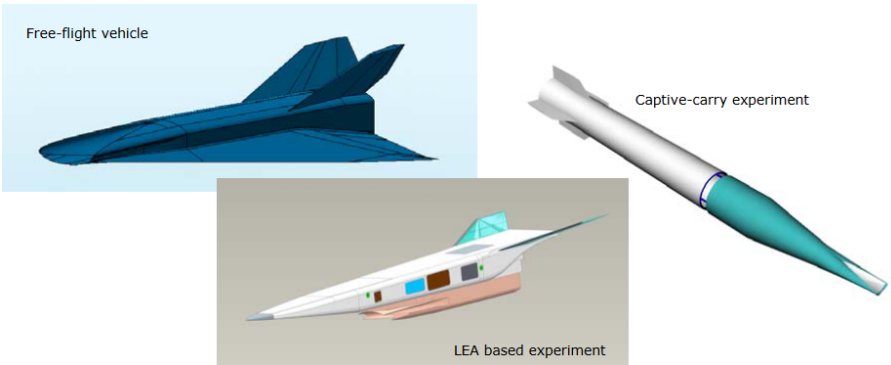

Fig. 2.44 HEXAFLY test vehicles [58]

The HEXAFLY project was followed up by the **High-speed EXperimental FLY vehicles-INTernational (HEXAFLY-INT project)** [59], which aims at demonstrating the feasibility of high-speed critical aspects in an experimental flight test campaign and gather flight data to validate technologies and methods for high-speed systems. It involves different partners from Europe, Russian Federation, Australia and Brazil. The reference vehicle is the HEXAFLY Experimental Flight Test Vehicle (EFTV) (Figure 2.45), which is a hypersonic waverider glider that has a total length of 3.29 m and a wingspan of 1.24 m, as shown in Figure 2.46. It is also equipped with two active elevons and a couple of fixed vertical fins, to be used for passive lateral-directional control.

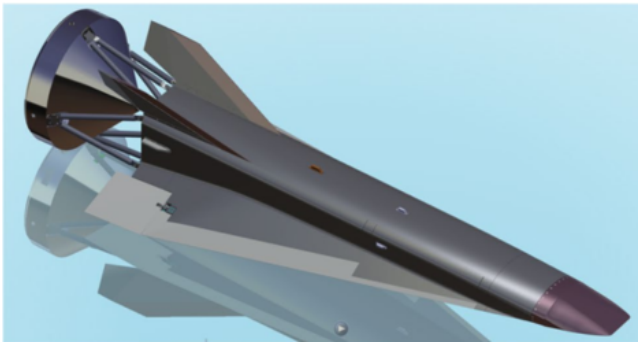

Fig. 2.45 HEXAFLY Experimental Flight Test Vehicle (EFTV) + Experimental Service Module (ESM)

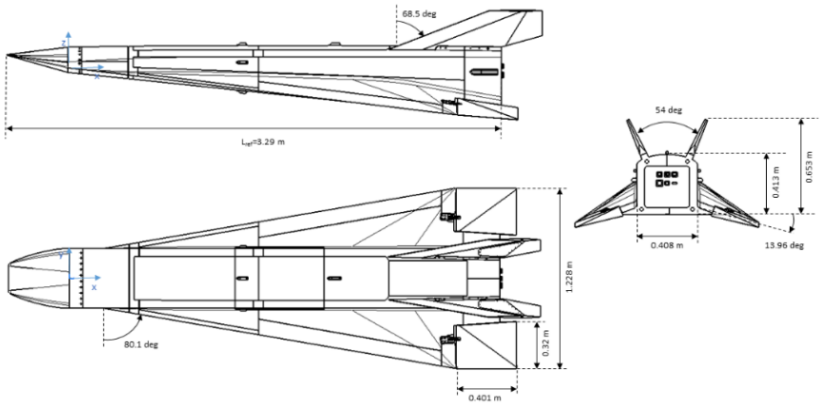

Fig. 2.46 HEXAFLY Experimental Flight Test Vehicle (EFTV) - geometric data [60]

The reference mission involves the use of the Brazilian VS50 launcher, which is capable of flying along a suborbital trajectory with an apogee at 90 km [59]. After

the release, the EFTV is supposed to fly the early descent docked to the Experimental Service Module (ESM) which is used to control the attitude of the vehicle. At an altitude of 55 km the vehicle detaches from the module, and performs the cruise phase at Mach 7 and an altitude of 32 km. The experimental window includes a controlled banking manoeuvre to fly within a radius of 600 km from the launch site and that is considered as the telemetry area. Then, the mission ends at Mach 2 and an altitude of 20 km. A complete overview of the mission scenario is reported in Figure 2.47.

Fig. 2.47 EFTV mission scenario [59]

Besides research projects, some private companies are also currently developing their own hypersonic passenger aircraft. Some examples are the European start-up Destinus [61] and the US company Hermeus [62].

Eventually, two additional EU funded projects focusing on high-speed passenger transportation should be mentioned: the H2020 STRATOFLY project and the H2020 MORE&LESS project. Since the research activity presented in this thesis has been conducted within the framework of these projects, a separated section (section 2.5) is dedicated to provide additional details on both projects.

2.5 Latest EU funded projects

The research activity presented in this thesis has been carried out within the field of the H2020 STRATOFLY project and the H2020 More&Less project. This section

is dedicated to presenting the two projects in detail: first, the Stratofly project is described in subsection 2.5.1, and then the More&Less project is presented in subsection 2.5.2.

2.5.1 H2020 STRATOFLY project - 2018-2020

Part of the research activity has been carried out within the field of the H2020 STRATOFLY project [63, 3], which received funding through the Horizon 2020 Research Programme and started in 2018. Leveraging the outcomes of various European projects on high-speed concepts, such as ATLLAS I/II [64, 65], HIKARI[66], LAPCAT I/II [55], HEXAFLY [57], and HEXAFLY Int [59, 67], it serves as an additional collaborative research initiative in this domain, supported by European funding. The project's main purposes are:

- to quantitatively assess the potential of civil high-speed aviation with respect to technical, environmental and economic viability in combination with human factors, social acceptance, implementation and operational aspects [2];
- to study the feasibility of high-speed civil transportation at stratospheric altitudes, while reducing the flight time on antipodal routes of one order of magnitude and ensuring a minimum environmental impact in terms of emitted noise and green-house gasses [2];
- to complete the design and concept of operations of the STRATOFLY MR3 vehicle, increasing the Technology Readiness Level (TRL) of pivotal high-speed technologies up to level 6 by 2035 [3].

The viability of a hypersonic aircraft is most logical when applied to cover distances from long-haul up to antipodal routes. This is because cruising at Mach 8 is most advantageous on long-haul routes, while medium-haul routes have cruise phases that are too short. A waverider configuration has been selected for the STRATOFLY vehicle, since it allows reaching a sufficiently high aerodynamic efficiency ($L/D >$ 6) at high speed. Moreover, liquid hydrogen is chosen as propellant, due to its higher specific energy if compared to hydrocarbon. This choice also guarantees complete decarbonization, achieving one of the main mission requirements. The STRATOFLY vehicle is characterized by a high-level of integration of propulsion

plant, aerothermodynamics, airframe and on-board subsystems. For this reason, a multidisciplinary design methodology has been developed within the STRATOFLY project to guarantee the best accordance between the vehicle design and the mission concept, and to ensure the achievement of an overall optimum and socially acceptable implementation of a high-speed aircraft fleet using feasible technologies. The vehicle configuration is derived from the LAPCAT MR2.4, studied within the LAPCAT II project [56]. An overview of STRATOFLY vehicle layout is reported in Figure 2.48 and highlights the high degree of integration among the vehicle and its subsystems [2, 68, 69].

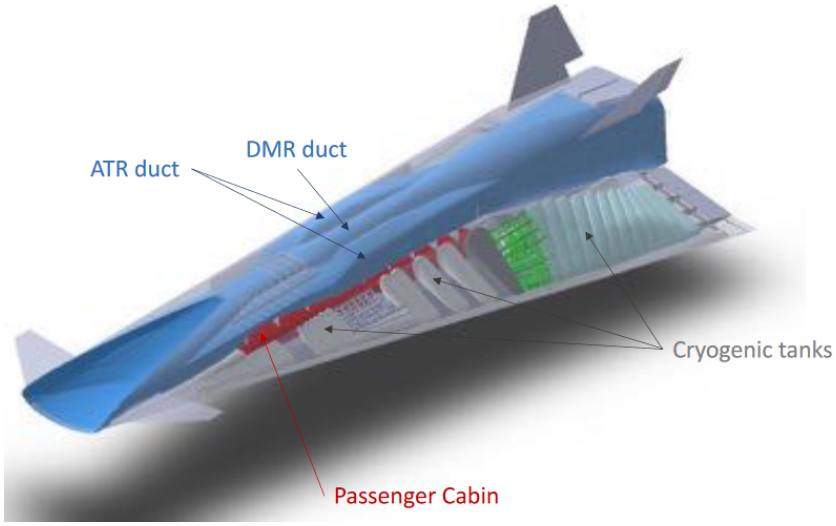

Fig. 2.48 STRATOFLY MR3 vehicle layout and subsystems integration

Indeed, during the LAPCAT-II project, the vehicle layout has been studied and optimized, focusing especially on aerothermodynamics and propulsion. However, less attention has been paid to the on-board subsystems and their integration. For that reason, during STRATOFLY, while the external dimensions of the MR2.4 are kept unchanged, some updates and modifications have been introduced for what concerns the internal vehicle architecture. The STRATOFLY partners have worked on the design, sizing and integration of the different subsystems. For example, the cabin compartment and the architecture of the tanks were re-designed exploiting the use of dual or multiple bubble structures, which allows achieving lightweight structures. The thermal and energy management subsystem has also been designed. Liquid hydrogen is exploited not only as a cooler for the most critical parts of the vehicle and the power plant elements, but it is also used to generate secondary power.

[70, 2] Moreover, additional numerical analyses have been carried on, in particular focusing on:

- the development of a complete aerodynamic database, obtained through CFD analysis [71];
- the analysis of the propulsive performance of the vehicle and the evaluation of the vehicle's emissions [72]
- the hydrogen combustion modelling [73];
- thermal analysis [74–77];
- structural analysis [78].

Finally, section 3.4 presents a complete overview of the STRATOFLY vehicle, which is one of the case studies of this research activity.

2.5.2 H2020 More&Less project

The H2020 More&Less project is a European project funded under the Horizon 2020 Research Programme in 2021 [4]. The research activity presented in this thesis has been partially conducted within the framework of this project. The project aims at *"supporting Europe to shape global environmental regulations for future supersonic aviation: recommendations are established on the basis of the outcomes of extensive high-fidelity modelling activities and test campaigns that merge into the multidisciplinary optimization framework to assess the holistic impact of supersonic aviation onto environment"* [4] (Figure 2.49).

Fig. 2.49 More&Less project

One of the main objectives is to assess the near and far-future supersonic aviation paradigm, including different types of aircraft and missions. At the same time, the project aims to contribute to citizen and environmental protection by conducting analyses on pollutant and greenhouse gas emissions, as well as noise. As a consequence of those analyses, the project works in support of the regulatory framework, to provide possible modifications and/or definitions of the regulations and procedures for future supersonic aircraft. A complete examination of current and upcoming environmental regulations and standards related to supersonic aircraft was conducted. The analysis is intended to verify areas in which the rulemaking process needs to evolve, particularly in adapting subsonic standards to the supersonic context. Technical data computed through the different analyses of the case studies can be exploited to outline reference flight profiles for supersonic aircraft. The aim is to formulate recommendations for adapting current CO_2 and noise standards to supersonic aircraft, while collaborating with the International Civil Aviation Organization's (ICAO) Committee on Aviation Environmental Protection (CAEP). Other objectives are also to contribute to preserving European knowledge and skills in the area of high-speed vehicles, while at the same time encouraging the cooperation with international partners.

The analysis starts from the conceptual design of a set of case studies, ranging from low to high-supersonic regime. Both low and high-fidelity modelling activities and experimental tests are performed, with a particular focus on the environmental impact of each concept. Particular focus is placed on the evaluation of the LTO cycle of such concepts to evaluate the pollutant emissions and noise levels, together with the analysis of the sonic boom and the impact on climate during the flight.

These data are also exploited to extend the use of already existing tools to supersonic aircraft design, which will be integrated into a multidisciplinary holistic framework. A wide range of the supersonic regime has been selected, from Mach 2 to Mach 5. Moreover, the possibility of exploiting alternative fuels to traditional hydrocarbons is investigated, by studying aircraft concepts that employ biofuels or cryogenic fuels. Exploring additional case studies involving diverse configurations, performance, and fuels allows for the improvement of tools flexibility. These tools, initially developed through modelling activities and test campaigns using the case studies, are designed to be adaptable for various vehicle concepts.

Chapter 3

Case studies

A variety of high-speed concepts were analyzed to test and validate the proposed methodology and tools. To cover different high-speed regimes, two types of vehicles were examined:

- wing-body configuration for cruise Mach number lower (or equal) than 3;
- waverider configuration for Mach number greater than 3.

The wing-body aircraft is more suitable for the supersonic range, flighting at a maximum Mach number of 3. Two configurations are analyzed here, the first one is a Mach 2 passenger transport concept (section 3.1), derived from the Concorde configuration, while the second one is a Mach 1.5 business jet (section 3.2). It is worth noticing that a third configuration is also available, which is a Mach 3 concept. However, due to limited data availability for this configuration during the research activity, it has been excluded from this thesis. This would be, however, an additional case study to include for future analysis. For higher cruise speeds, waverider concepts should be considered. For this work, two vehicles are taken into account, with a cruise Mach number equal to 5 and 8. These configurations are described in detail in section 3.4 and section 3.5. However, an additional general section has been included to better introduce the waverider concept and provide valuable details about this peculiar configuration in section 3.3. The complete list of case studies is reported in Figure 3.1.

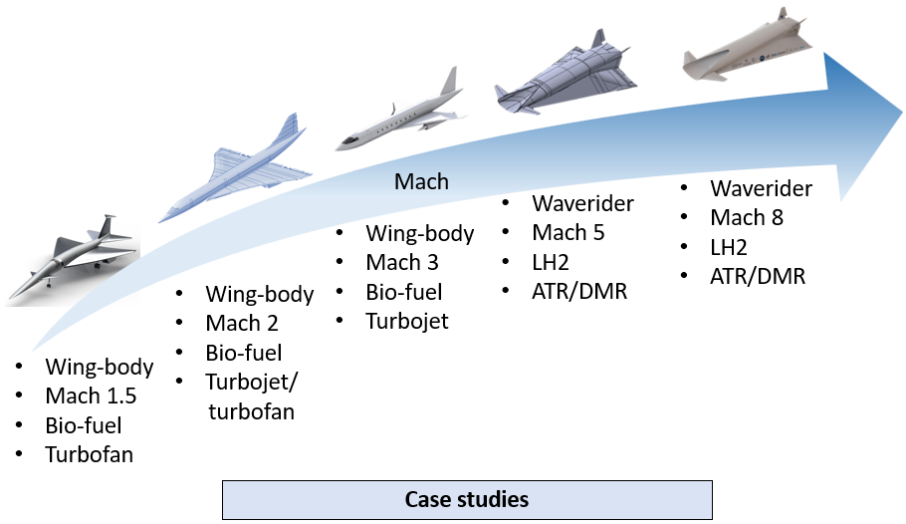

Fig. 3.1 Case studies overview

3.1 Mach 2 wing-body configuration

One of the case studies considered in the MORE&LESS project is a Mach 2 aircraft powered with biofuel, which is inspired by the Concorde configuration, targeting a minimization of noise and pollutant emissions as well as the lowest environmental impact at local, regional and global level. The aircraft's characterization involves various aspects including vehicle design, aerodynamic and propulsive characterization, and mission simulation. The MTOM of the aircraft is about 177 tons, with a maximum payload of 15280 kg and a fuel mass of 82180 kg. The aircraft's main geometric parameters are reported in Table 3.1, while an image of the aircraft is shown in Figure 3.2.

Table 3.1 Mach 2 concept geometric data

Parameter	Value
Cruise Mach number [-]	2
Wing surface [m^2]	327
Wingspan [m]	25.6
Fuselage length [m]	62.25
MTOM [Mg]	176.85
Passengers [-]	$\sim$ 120

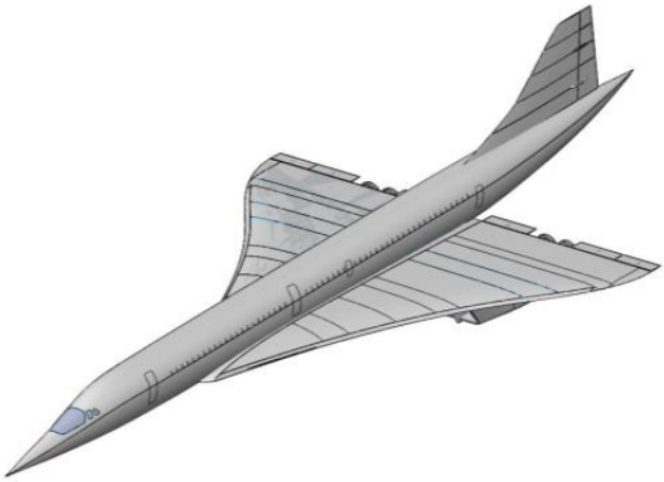

Fig. 3.2 Overview of Mach 2 aircraft

The Mach 2 aircraft is equipped with 3 elevons on each wing side and a tail rudder, which is divided into two separate surfaces. Table 3.2 reports the control surfaces main data.

Table 3.2 Flight control surfaces data for the Mach 2 aircraft

Surface	Chord[m]	Span[m]	Deflections [deg]	Surface [m^2]
Elevon (internal)	2.38	2.95	$\pm$ 25	7.02
Elevon (central)	1.93	2.35	$\pm$ 25	4.54
Elevon (external)	1.63	3.45	$\pm$ 25	5.63
Rudder (upper)	1.56	3.25	$\pm$ 15	5.07
Rudder (lower)	2.07	2.05	$\pm$ 15	4.24

3.1.1 Mach 2 reference mission

The mission of the Mach 2 configuration is presented in this section. The reference route is a long-haul route connecting Paris to New York, for a total range of approximately 5800 km. During the first part of the mission the aircraft performs a subsonic climb up to Mach=0.95 at an altitude of approximately 9 km. Then, a subsonic cruise follows, which is needed to avoid any sonic boom to happen while flying over land. The following phase is a supersonic climb, where the aircraft accelerates up to Mach

2 at an altitude of 15 km. An overview of the reference mission profile is reported in Figure 3.3.

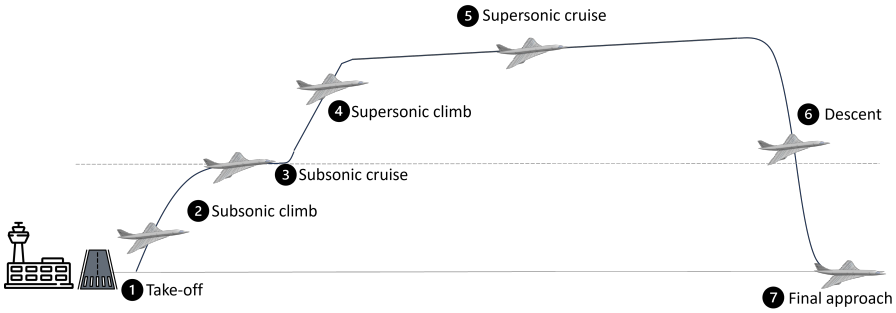

Fig. 3.3 Reference Mach 2 mission profile

3.2 Mach 1.5 wing-body configuration

An additional case study considered in this work is a Mach 1.5 business jet, which is equipped with two turbofan engines exploiting biofuels. Even if this configuration is not part of the STRATOFLY or More&Less projects, it has been included to extend the Mach number range and include cruise Mach lower than 2. The MTOM of this aircraft is about 39 tons, with a maximum payload of 1.5 tons and a fuel mass of 18 tons. The aircraft main geometric parameters are reported in Table 3.3, while an image of the aircraft is shown in Figure 3.4.

Table 3.3 Mach 1.5 concept geometric data

Parameter	Value
Cruise Mach number [-]	1.5
Wing surface [m^2]	112
Wingspan [m]	14
Fuselage length [m]	44
MTOM [Mg]	39
Passengers [-]	12

Fig. 3.4 Overview of Mach 1.5 business jet

3.2.1 Mach 1.5 reference mission

The reference mission of the Mach 1.5 aircraft is quite similar to the one of the Mach 2 case study, and it is designed to reach a maximum range of 6500 km. An overview of the different mission phases is reported in Figure 3.5. The main difference with respect to the Mach mission is the duration of the climb phase, which in this case is shorter, since the aircraft has to accelerate up to Mach 1.5, instead of 2. As a consequence, the cruise is held at a lower altitude, starting at approximately 14 km.

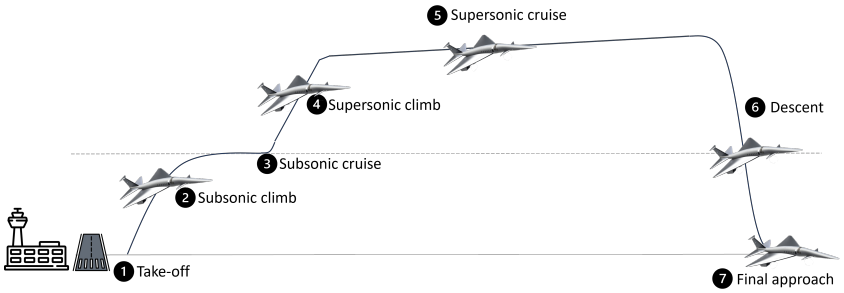

Fig. 3.5 Reference Mach 1.5 mission profile

3.3 The Waverider configuration

A waverider can be defined as *"any shape designed such that the bow shock generated by the shape is perfectly attached along the outer leading edge at the design flight condition."* [79] This configuration can be convenient in terms of aircraft performance with respect to conventional non waverider configurations, especially for what

concerns the lift-to-drag ratio. Moreover, it is fundamental to account for the skin friction drag contribution since the early phases of the waverider design [80, 81]. Indeed, due to the very large wetted surface area, the value of skin friction drag can be much higher than for a typical wing-body configuration. Usually, the vehicle's shape is derived from the flow field analysis, considering a steady inviscid supersonic flow field. Two types of flow can be selected: a steady two-dimensional planar or axisymmetric or a three-dimensional supersonic flow field [82]. For a first and preliminary design, the 2-D options can be selected, due to their simplicity compared to the 3-D one. Then, the viscous streamlines are introduced, to account for the effect of viscous flow. Once the flow field has been constructed, together with the development of inviscid and viscous streamlines, a three-dimensional waverider configuration can be derived from these streamlines [83].

Different shock surfaces can be generated, such as wedge-derived, wedge-cone based, and osculating cone-derived, etc., which lead to different vehicle configurations. For example, Figure 3.6 shows how a conical-flow waverider can be designed. The body's lower surface is found at the intersection between the conical flow stream surface and the shock wave, which defines the leading edge of the body. The body upper surface is obtained considering that it is a free-stream surface.

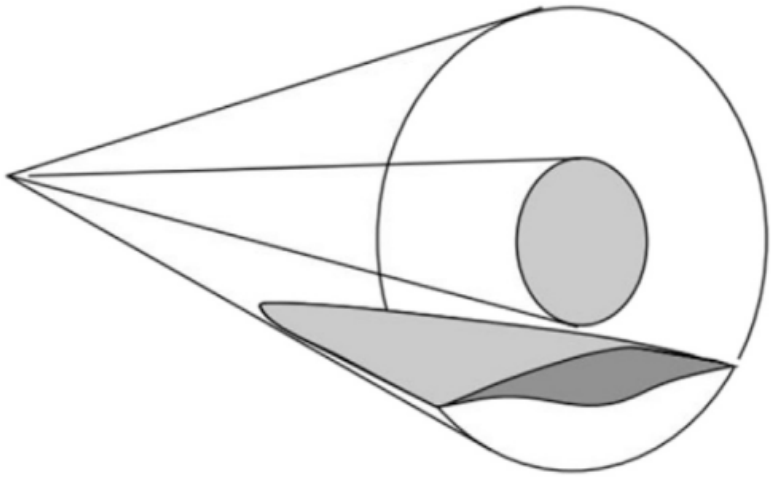

Fig. 3.6 Waverider derived from conical flow-field [83]

The osculating-cone theory was exploited to design the LAPCAT MR2.4 vehicle, and consequently, the derived STRATOFLY MR3 vehicle. For both those vehicles, the airframe and propulsion integration allows for a high-efficiency compression

airflow for the engine [82]. Moreover, the integration of the intake within the fuselage guarantees a very high mass capture [84].

3.4 STRATOFLY MR3 Mach 8 waverider

STRATOFLY MR3 vehicle is a Mach 8 waverider, which integrates 6 Air Turbo Rocket engines (ATR) that operate up to Mach 4-4.5 and a Dual Mode Ramjet (DMR). They both use liquid hydrogen as a propellant. The external shape of the vehicle resembles the one of the MR2.4 vehicle, having the same propulsion plant, but with different flight control surfaces, different rounding of the leading edges and a modified nozzle area. Specifically, during the redesign the waverider shape was modified taking into account the integration of subsystems and internal compartments. The primary goal was to achieve a greater degree of volumetric efficiency compared to the MR2.4. The vehicle is designed to have a Maximum Take Off Mass of about 400 tons, hosting 300 passengers for a total payload capacity of 33 tons and an empty mass of around 187 tons. The reference planform surface is around 2500 m^2 and the total internal volume is equal to 10000 m^3. An overview of the main data is reported in Table 3.4, while the vehicle shape is depicted in Figure 3.7. Liquid hydrogen has been chosen as propellant due to its high specific energy content, enabling the aircraft to fly along antipodal routes at a speed of Mach 8 without generating any CO_2 emission. This configuration provides numerous benefits in terms of aircraft performance, notably in achieving a high lift/drag ratio when compared to traditional non waverider designs.

Table 3.4 STRATOFLY MR3 waverider geometric data

Parameter	Value
Cruise Mach number [-]	8
Planform surface [m^2]	2500
Wingspan [m]	41
Fuselage length [m]	94
Internal volume [m^3]	10000
MTOM [Mg]	400
OEW [Mg]	187
Passengers [-]	300

Fig. 3.7 Overview of STRATOFLY MR3 waverider

The MR3 aircraft layout incorporates several aerodynamic control surfaces, including a fully adjustable canard, four elevons, two body flaps situated atop the integrated nozzle, and a pair of V-shaped rudders [85], as shown in Figure 3.8. The control surfaces main data are reported in Table 3.5.

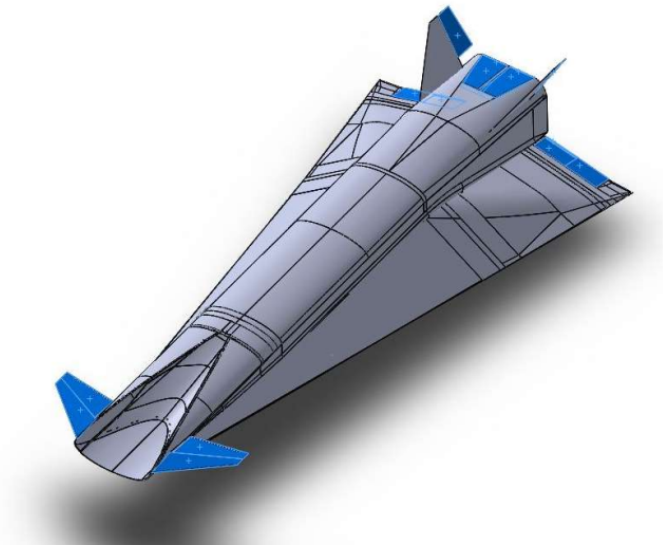

Fig. 3.8 Overview of STRATOFLY MR3 flight control surfaces

Table 3.5 Flight control surfaces data for the MR3 vehicle

Surface	Chord[m]	Span[m]	Deflections [deg]	Surface [m^2]
Elevon	3.00	5.00	$\pm$ 25	15.00
Canard	5.75	8.70	$\pm$ 20	50.00
Body flap	7.14	4.05	0 $\leftrightarrow$ -30	23.70
Canard	3.05	6.50	$\pm$ 20	19.80

3.4.1 Mach 8 reference mission

The reference mission considered for the analysis is an antipodal route, connecting Brussels to Sydney, for a total range of approximately 19000 km. During the first part of the mission, ATR engines are used. The vehicle performs a subsonic climb up to Mach=0.95 at an altitude of approximately 13 km. Then, the vehicle performs a subsonic cruise, which is needed to avoid any sonic boom to happen while flying over land. A constraint on the distance flown from the departure site is considered, to fulfil this requirement: the subsonic cruise phase ends when the vehicle is at 400 km from the departure airport. The Brussels airport meets the requirement, but any other airport located less than 400 km from the sea may also be chosen. Next, the vehicle performs a second climb, until it reaches Mach 4 (supersonic climb). At the end of this phase, the DMR is activated. During the first part of the hypersonic climb, from Mach 4 to Mach 4.5 the thrust generated by the DMR only is not sufficient. For that reason, during this part of the flight the DMR is used together with the ATR engines. Then, ATR engines are turned off and only the DMR is used to accelerate up to Mach 8 at an altitude of 32 km (hypersonic climb). The cruise is performed at Mach 8 and an altitude between 32 and 36 km. Since it is necessary to avoid flying over land due to the sonic boom requirements, so the vehicle cannot follow the shortest trajectory towards the destination airport. During the first part of the cruise, it flies over the Arctic region towards the Bering Strait, between Asia and North America. Then, the vehicle continues to cruise over the Pacific Ocean towards Sydney. The cruise phase is over when a certain distance from the landing site is reached. This distance depends on the type of descent considered, i.e. propelled or gliding descent. The first mission concept involved a gliding descent. However, since the aerodynamic performance could be very low in engine-off conditions, a propelled descent has

been considered for the final version of the mission concept. An overview of the reference mission profile is reported in Figure 3.9.

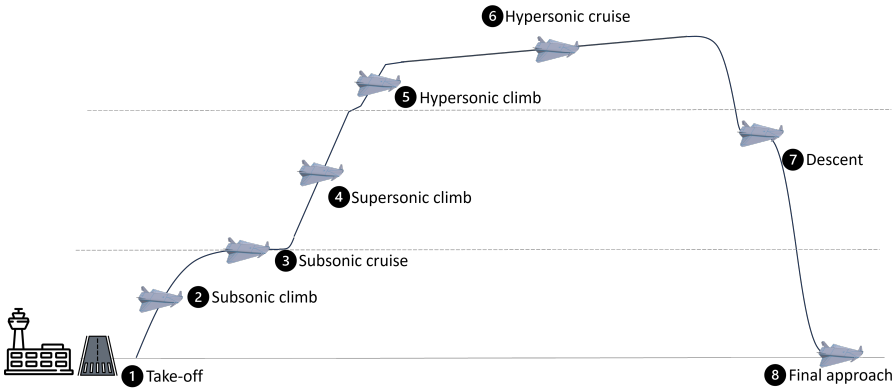

Fig. 3.9 Reference Mach 8 mission profile

3.5 MR5 Mach 5 waverider

The MR5 vehicle is a Mach 5 waverider designed to perform an antipodal route mission, with a maximum range of 19000 km. The configuration is derived from the STRATOFLY MR3 vehicle, which is described in section 3.4. It is essential to prompt a re-evaluation of the reference vehicle layout, while preserving a similar configuration in terms of aerodynamic and propulsive flow-path, to avoid compromising a concept that has demonstrated high aerodynamic efficiency and operational effectiveness at Mach 8. A complete overview of the redesign process conducted within the MORE&LESS project is reported in [86]. However, it is worth reporting the most important details about re-design process in this section briefly. First, the STRATOFLY MR3 vehicle has revealed an excess of lift throughout the Mach 5 regime, making it challenging to maintain the specific altitude during cruise. Moreover, the intake is not optimized to work at Mach 5 cruise flight, generating large amount of spillage. The nozzle should also be modified, because it is now working at a lower Mach number and altitude, and it is experiencing an overexpansion [86]. For that reason, some preliminary estimation have been conducted to re-design the air intake to minimize spillage at Mach 5. At the same time, the overall dimension of the vehicle have been reduced, to limit the generation of lift. Numerical simulation indicates that, at Mach 5 and an altitude of 25 km, the nozzle contributes to thrust generation only up to a horizontal coordinate of approximately 74 m (in relation to

the vehicle length). Conversely, the remaining portion is ineffective and, notably, contributes to drag. The initial method involves choosing a linear scaling factor to be implemented across all dimensions (x, y, z) of the vehicle. This approach aims to maintain the configuration while gradually reducing the overall layout. Conversely, the second approach concentrates on applying a linear scaling factor exclusively to the x dimension, intending to specifically reduce the length of the vehicle.

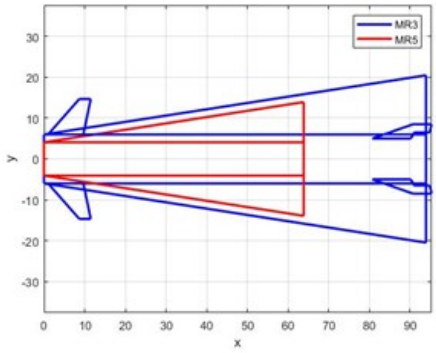

Fig. 3.10 Top view of MR5 vehicle layout with homogeneous scaling

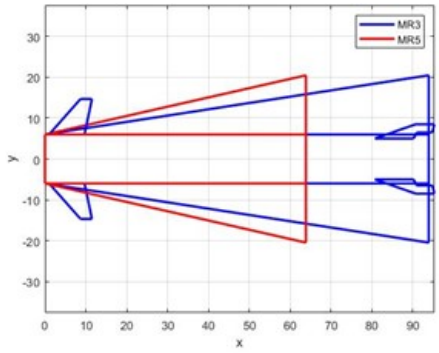

Fig. 3.11 Top view of MR5 vehicle layout with 1D scaling

The homogeneous scaling approach maintains the same aircraft configuration, preserving aerodynamic performance but rapidly reducing vehicle volume as a cubic function of the scaling factor. This method doesn't limit aerodynamic balance issues experienced in the original layout during cruise, as the reduction in overall mass outpaces the reduction in lifting surface due to the square-cubic law effect. Essentially, homogeneous scaling transfers existing problems to smaller dimensions while retaining issues related to excessive lengths of intake and nozzle elements. In contrast, the 1D scaling process results in a modified vehicle configuration with reduced slenderness: the overall length decreases while keeping the wingspan constant. Linearly influenced by the scaling factor, the reduction in main surfaces and volumes occurs at a slower rate compared to homogeneous scaling. Configuration parameters, such as wing sweep angle, are altered, and adjustments are required for canard and vertical tails to account for their changed proportions relative to the Centre of Gravity (CoG). Eventually, the 1D scaling is selected due to the more promising aerodynamic balance, volume feasibility and range capability [86].

The MR5 vehicle is equipped with a dorsal-mounted propulsion system, with 6 Air Turbo Rockets and a Dual Mode Ramjet. The ATRs are employed during the initial phase of the mission, encompassing both subsonic and supersonic velocities,

reaching up to Mach 4-4.5. The DMR becomes operational for the latter part of the ascent and throughout the cruising phase at Mach 5. The propulsion system is powered by the utilization of liquid hydrogen. Positioning the propulsion system at the top of the vehicle ensures the maximal utilization of the available planform area for generating lift while avoiding extra drag penalties, thus optimizing the internal volume. The vehicle's total length is equal to 75.16 meters, and it has a wingspan of 41 meters. The planform area measures $2000m^2$ and the internal volume layout is $8000m^3$. A summary of the geometric data is reported in Table 3.6, while a visual depiction of the vehicle is presented in Figure 3.12.

Table 3.6 MR5 waverider geometric data

Parameter	Value
Cruise Mach number [-]	5
Planform surface [m^2]	2000
Wingspan [m]	41
Fuselage length [m]	75.16
Internal volume [m^3]	8000
MTOM [Mg]	288
OEW [Mg]	150

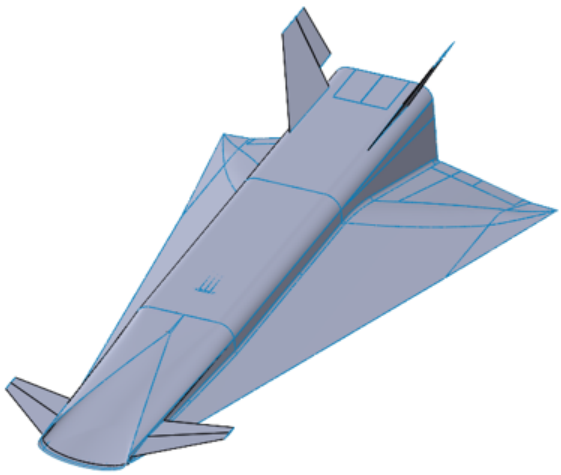

Fig. 3.12 Overview of MR5 waverider

3.5.1 Mach 5 reference mission

The reference mission of the Mach 5 configuration is similar to the one of the Mach 8 vehicle subsection 3.4.1. They are both designed to travel along antipodal routes, with a maximum range of 19000 km. The main difference between the two mission profile is the shorter climb phase of the Mach 5 vehicle with respect to the Mach 8 case study. This is of course due to the fact that it has to reach a lower Mach to start the cruise phase. Then, also the cruise altitude will be lower and equal to 30-32 km.

Chapter 4

Methodology

The design of complex and highly innovative aerospace systems could lead to an extension of the timeline necessary for the design, development, and production of new concepts. This research work focuses on the design phase and the development of methodology and tools for the conceptual design. The design process of innovative high-speed transportation systems is characterized by two main aspects, which add complexity to the design process. First, the vehicle design must deal with a high level of integration, which leads to the development of a methodology capable of managing different levels of detail, effectively tracing the influence of systems and subsystems integration back to the vehicle level. However, during the initial stages of conceptual design, the availability of high-fidelity data is limited, and in-depth analysis of vehicle configuration and performance becomes unfeasible. Thus, there is an imperative to leverage innovative and agile design methodologies that can capture the most influential design, performance, and operational characteristics. At the same time, the vehicle is directly influenced by (and can impact on) top-level requirements which can impose major changes in the vehicle concept. Therefore, a simultaneous consideration of both these elements is essential when dealing with the design of any high-speed vehicle. An overall overview of the methodology proposed in this work is reported in Figure 4.1. A multidisciplinary and multi-fidelity approach is suggested for the conceptual design of high-speed aircraft, where every stage combines multiple analyses with an equivalent level of detail. Different disciplines are involved, such as aerodynamics, propulsion, structures, etc... However, in this work, the focus is on the aerodynamic modelling and mission analysis, while the other elements, such as propulsive and vehicle geometry data, are considered as external inputs. At

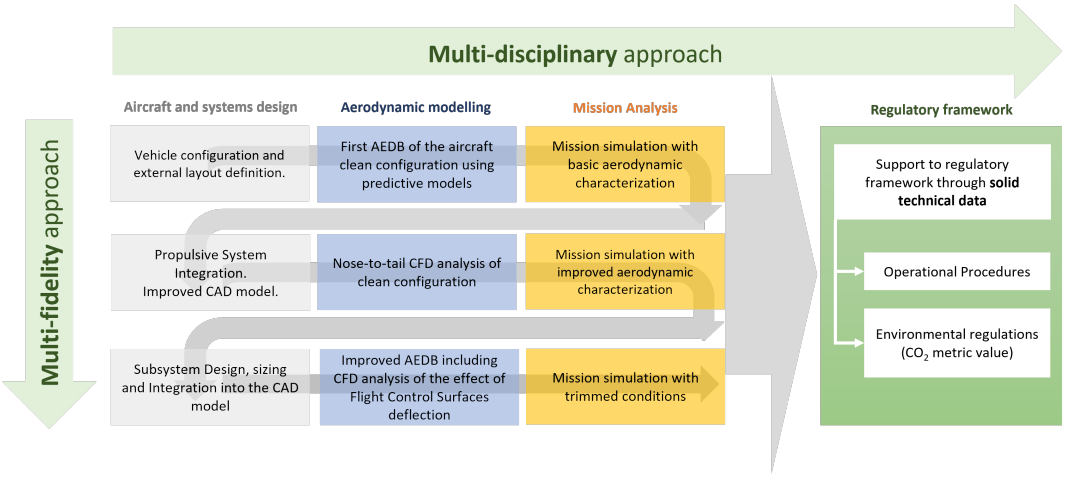

Fig. 4.1 Methodology overview

the beginning of the analysis, only a preliminary vehicle configuration and layout is defined. There is a need for a rapid evaluation of the vehicle's aerodynamic performance, since the configuration is not consolidated, and it can change in future iterations.

Then, for a first aerodynamic characterization, simple but accurate simplified formulation have been developed, starting from models already availabile in literature. These formulations are used to predict the aerodynamic performance of high-speed vehicles based on a limited set of input data, exploiting models already available in literature. These models allow for a first estimation of the vehicle performance along the reference trajectory. The mission simulation, typically considered as a final concept validation is here assured of a discipline role, ensuring more precise estimations of nominal ranges, fuel mass, fuel reserves, etc., at each step of the design phase.

The second step starts when the final configuration is assessed, and it is possible to exploit higher fidelity evaluation, such as CFD aerodynamic analysis. Aerodynamic data obtained from simplified models in the previous iteration can be compared to the higher fidelity data available at this step, to assess the accuracy of the first estimation. A second mission simulation is run to update vehicle performance along the reference mission, providing more precise validation of the mission concept.

Then, once the flight control system design is completed, and as soon as higher fidelity data are available for both the clean configuration and the contribution of the control surfaces deflections, the vehicle's stability and trimmability can be analysed.

The last step of the aerodynamic characterization results in a trimmed aerodynamic database, which can be used for an additional mission simulation.

The resulting set of technical data can be later used as input in support of the regulatory framework. In particular, two main aspects have been analysed in this thesis. First, the airport proximity operational procedures have been studied, focusing on the estimation of take-off and landing distance requirements, to evaluate the ability of the high-speed concepts to operate within the present airport infrastructure. Moreover, it should be considered that the development of new civil high-speed passenger aircraft configurations and missions is pushing international authorities to update the regulatory framework to limit nuisances on ground and the contribution to climate change. In particular, an aeroplane CO_2 standard exists for subsonic aircraft, while it is not defined for supersonic designs. The outcome of the different analyses can be used to support regulatory authorities' work towards a potential CO_2 emission standard specifically tailored for supersonic aeroplanes.

The complete methodology followed to perform the preliminary aerodynamic modelling is presented in section 4.1, while the process for the verification of the vehicle static stability and trim analysis is described in section 4.2 section 4.3 focuses on the description of the mission simulation. Eventually, section 4.4 presents the work to support the regulatory framework.

4.1 Aerodynamic modelling

From the beginning of the design phase, an in-depth exploration of aerodynamics stands as a pivotal element: employing effective preliminary methodologies, as emphasized by [11], proves valuable in conceptual design and trade studies, to define the most efficient configuration. However, it is imperative to acknowledge that these initial methodologies, while insightful, necessitate subsequent augmentation through more sophisticated analyses to progress towards the vehicle's final configuration. The aerodynamic characterization proposed here unfolds systematically, advancing through three distinct stages, each contributing to increased precision. Initially, simplified models come into play, providing foundational estimates during the preliminary stages of design. Then, CFD aerodynamic analysis is introduced, focusing on the clean configuration, that excludes the deflection of control surfaces. This stage introduces a more detailed and accurate assessment of the aerodynamic

performance. The final step in this process involves the evaluation of the additional impact stemming from the deflection of control surfaces. However, it is important to note that this thesis only covers the initial step of aerodynamic analysis, while the CFD results are treated as external inputs. An overview of the aerodynamic analysis workflow is reported in Figure 4.2.

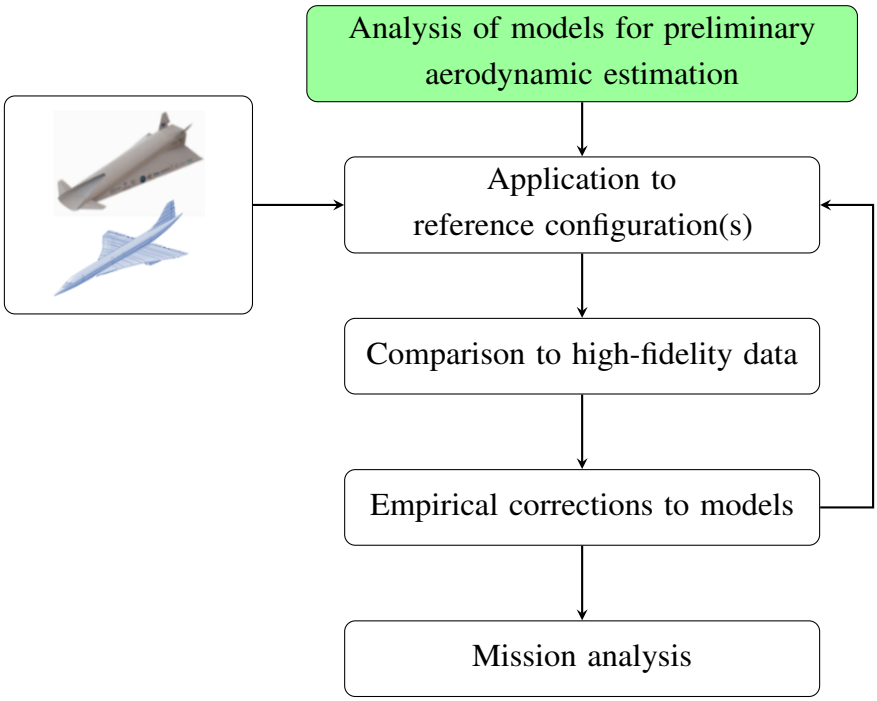

Fig. 4.2 Workflow for the aerodynamic analysis

Therefore, basic but quite reliable engineering tools have been employed to estimate the aerodynamic coefficients of new concepts design using a limited set of input data. In particular, for this study, two types of high-speed vehicles are considered: typical delta wing body configurations for supersonic Mach numbers (up to Mach $\simeq 3$) and waverider configurations for higher Mach numbers (Mach ≥ 5). In accordance with the specific configuration type, the coefficients are calculated and subsequently compared with more accurate data derived from CFD simulations, conducted for the respective aircraft. The primary objective underlying this comparative analysis is the identification of potential empirical refinements for the models, with the main aim of augmenting their capability to accurately represent the aerodynamic characteristics exhibited by other vehicles sharing analogous configurations. This iterative process ultimately contributes to the establishment of a preliminary aero-

dynamic database, which serves as a foundational resource for validating different vehicle concepts through comprehensive mission analyses. The significance of this phase lies in its capacity to quantify the reliability of the developed models, not only in terms of predicting aerodynamic performance but also in assessing the capability of the vehicles to execute their designated missions successfully.

4.1.1 All-body hypersonic model

The first aerodynamic model is the All-Body Hypersonic (ABH) model, originating from the work of [87]. This model pertains to a distinct aircraft configuration, characterized by a delta planform featuring an elliptical cone forebody and an elliptical cross-section afterbody, which forms a smooth transition surface from the end of the forebody to a straight-line trailing edge. The reference configuration is shown in Figure 4.3, and it can be characterized using three distinct and autonomous parameters:

- Leading-edge sweep angle (Λ_{le});
- Breakpoint length ratio (l_h/l), where l is the total body length and l_h is the position of the breakpoint between forebody and afterbody;
- Fatness ratio (S_{max}/S_{plan}), where S_{max} is the maximum cross-section area and S_{plan} is the total planform area.

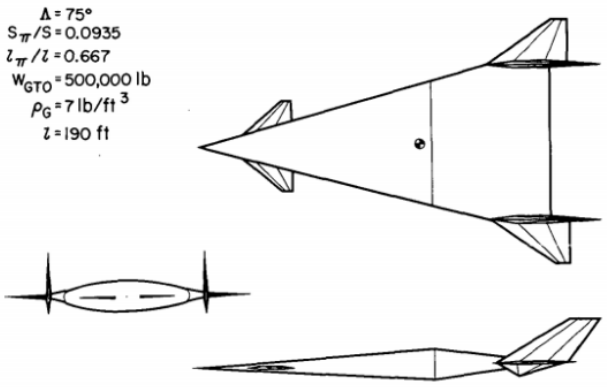

Fig. 4.3 All-Body Hypersonic reference vehicle [87]

An additional parameter, the forebody cross-section ellipse ratio, can be defined:

$$\frac{a}{b} = \frac{\pi(l_\pi/l)^2 cot(\Lambda_{le})}{S_{max}/S_{plan}} \tag{4.1}$$

where a is the semi-major axis of the ellipse, and b is the semi-minor axis. This model allows to calculate the lift and drag coefficients, taking into account not only the body's contribution, but also the one of any supplementary fins (such as the vertical tail, horizontal tail, and Canard). The lift coefficient C_L is computed as follows:

$$C_L = C_1 \sin(\alpha) + C_2 \sin(\alpha)^2 \tag{4.2}$$

where C_1 and C_2 are coefficients which are evaluated differently depending on the flight regime, as reported in Equation 4.3 and Equation 4.4.

$$\begin{cases} C_1 = \dfrac{\pi \cdot AR}{2} - 0.355 \cdot \beta^{0.45} \cdot AR^{1.45} & M \leq 1 \\ C_1 = \dfrac{\pi \cdot AR}{2} - 0.153 \cdot \beta \cdot AR^2 & M > 1 \; and \; \beta < 4/AR \\ C_1 = \dfrac{4.17}{\beta} - 0.13 & M > 1 \; and \; \beta \leq 4/AR \end{cases} \tag{4.3}$$

Where AR is the aspect ratio, $\beta = \sqrt{|M^2 - 1|}$ is the compressibility factor and M is the Mach number.

$$\begin{cases} C_2 = 0 & M \leq 1 \\ C_2 = linear \; interpolation \; on \; \beta & M > 1 \; and \; \beta < 4/AR \\ C_2 = e^{[0.955 - (4.35/M)]} & M > 1 \; and \; \beta \leq 4/AR \end{cases} \tag{4.4}$$

The total drag coefficient C_D can be determined by taking into account the contribution arising from the zero lift drag C_{D_0} and the induced drag C_{D_i} (see Equation 4.5).

$$C_D = C_{D0} + C_{Di} \tag{4.5}$$

The zero lift drag coefficient C_{D_0} (Equation 4.6) is given by the sum of body pressure drag $C_{D_{pB}}$, friction drag $C_{D_{fB}}$ and bluntness drag $C_{D_{bB}}$.

$$C_{D0} = C_{D_{pB}} + C_{D_{fB}} + C_{D_{bB}} \tag{4.6}$$

The body pressure drag is assumed to be zero at subsonic speed ($M \leq 0.8$), it is approximated as a linear variation with Mach number at transonic speeds ($0.8 < M < 1.2$), while it is evaluated from numerical integration of pressure distribution on body for $M \geq 1.2$.
The friction drag is evaluated through a relation based on turbulent boundary layer, flat-plate skin friction and contains an empirical correction for thickness induced pressure fields [87], for Mach numbers lower than 0.8. For $M \geq 1.2$, the skin friction can be obtained by numerical integration of the local skin-friction coefficient distribution. Also in this case, since there are no explicit relations to be used for the transonic regime, the skin friction is assumed to vary linearly with Mach (for $0.8 < M < 1.2$).
The bluntness drag is assumed to be negligible at subsonic velocities, while it is estimated using the Newtonian flow approximation for $M \geq 1$.

The induced drag coefficient is evaluated as:

$$C_{Di} = K_m \cdot C_L \cdot \tan(\alpha) \tag{4.7}$$

where K_m is an empirical coefficient based on experimental data, to account for the cone's rounded leading edge, and it can be computed as:

$$\begin{cases} K_m = 0.25 \cdot (1 + M) & M < 3 \\ K_m = 1 & M > 3 \end{cases} \tag{4.8}$$

4.1.2 Raymer model

The second model examined is derived from [11]. It pertains to a generic high-speed aircraft configuration characterized by a distinct separation between the fuselage and the delta wing, as can be seen in Figure 4.4. Each element of the aircraft (wing, fuselage, tails, nacelles, etc.) can be included to estimate the aerodynamic coefficients.

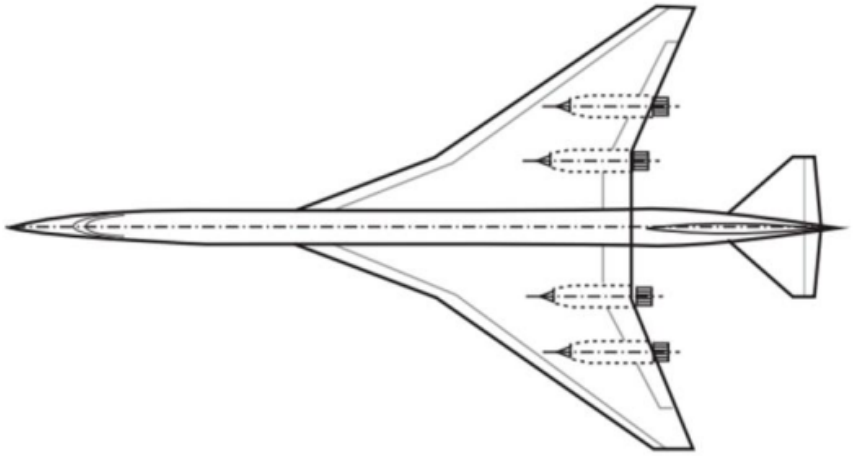

Fig. 4.4 Raymer model reference configuration [11]

The lift coefficient C_L can be expressed as a function of the angle of attack:

$$C_L = C_{L\alpha} \cdot \alpha \tag{4.9}$$

where C_{L_α} is the lift-curve slope and varies depending on the Mach number and flight regime. For subsonic Mach numbers it is evaluated as:

$$C_{L_\alpha} = \frac{2 \cdot \pi \cdot AR}{2 + \sqrt{4 + \left(\frac{AR \cdot \beta}{\eta}\right)^2 \left(1 + \frac{\tan^2(\Lambda)}{\beta^2}\right)}} \left(\frac{S_{exposed}}{S_{ref}}\right) F \tag{4.10}$$

where $\beta = 1 - M^2$, η is the airfoil efficiency which can be approximated to 0.95, $S_{exposed}$ is the exposed wing planform, and F is the fuselage lift factor which considers the lift generated by the fuselage of diameter d, and it is computed as:

$$F = 1.07 \left(1 + \frac{d}{b}\right)^2 \tag{4.11}$$

For supersonic Mach numbers the lift-curve slope can be expressed as:

$$C_{L_\alpha} = \frac{4}{\beta} \tag{4.12}$$

Where $\beta = \sqrt{M^2 - 1}$. This equation is valid for a wing in purely supersonic flow, i.e. when the Mach cone angle is larger than the leading edge sweep angle. However, it

must be highlighted that one of the main limitations of this model is that the lift at zero angle of attack C_{L_0} cannot be evaluated. For that reason, C_{L_0} is supposed to be zero as a first approximation.

The total drag coefficient is given by the sum of zero lift drag C_{D_0} and induced drag C_{D_i}:

$$C_D = C_{D_0} + C_{D_i} \tag{4.13}$$

C_{D_0} can be estimated for each element using a component build-up method. It is given by the sum of skin friction drag coefficient C_{D_f}, miscellaneous drag coefficient $C_{D_{misc}}$ and leakage and protuberance drag coefficient $C_{D_{L\&P}}$:

$$C_{D_0} = \frac{\sum(C_{f_c} \cdot FF_c \cdot Q_c \cdot S_{wet_c})}{S_{ref}} + C_{D_{misc}} + C_{D_{L\&P}} \tag{4.14}$$

where C_{f_c} represents the flat plate skin-friction, FF_c is a "form factor" which gives an overview of the component's pressure drag due to viscous separation, Q_c is a factor accounting for any interference effects on the component drag and S_{wet_c} is the wetted area of each element. The miscellaneous drag $C_{D_{misc}}$ allows to compute the contribution of any special features of an aircraft, such as flaps, unretracted landing gear, unswept aft fuselage, etc. The $C_{D_{L\&P}}$ accounts for the effect of leakages and protuberances.
The skin-friction coefficient can be evaluated differently depending on the flow type, which can be laminar or turbulent:

$$\begin{aligned} &Laminar: \\ &\quad C_f = 1.328/\sqrt{Re} \qquad (4.15) \\ &Turbulent: \\ &\quad C_f = \frac{0.455}{(\log_{10} Re)^{2.58} \cdot (1 + 0.144 \cdot M^2)^{0.65}} \qquad (4.16) \end{aligned}$$

where Re is the Reynolds number, which includes air density ρ, velocity V, length l and air viscosity μ. It is evaluated as $Re = \frac{\rho V l}{\mu}$. The component form factor FF_c allows to consider the effect of flow separation on pressure drag. It is an empirical correction, and it varies depending on the flight regime and on the type of element

considered (fuselage, wing, nacelle, etc.).

Wing :

$$FF = \left[1 + \frac{0.6}{(x/c)_m \left(\frac{t}{c}\right) + 100 \left(\frac{t}{c}\right)^4}\right] 1.34 \cdot M^{0.18} (cos\Lambda)^{0.28} \tag{4.17}$$

Fuselage :

$$FF = \left(0.9 + \frac{5}{f^{1.5}} + \frac{f}{400}\right) \tag{4.18}$$

Nacelle :

$$FF = 1 + 0.35/f \tag{4.19}$$

where $(x/c)_{max}$ is the chordwise location of the airfoil maximum thickness point, $\frac{t}{c}$ is the airfoil thickness to chord length ratio, Λ is the sweep angle of the wing, and $f = l/d$. The interference drag Q_c is also evaluated depending on the type of component considered, and it expressed as a factor which increases component drag, as can be seen in Table 4.1.

Table 4.1 Component interference drag

Component	Q_c
Fuselage	1
Wing	1
Nacelle	1.5
Tail surface	1.03

The supersonic parasite drag is evaluated considering the same contributions of the subsonic one, where the coefficients FF_c and Q_c are set equal to 1. Moreover, an additional contribution to drag is also included: the wave drag $C_{D_{wave}}$. It is a pressure drag that arises due to the presence of shocks, and it is linked to the volume distribution of the aicraft from nose to tail. The ideal distribution is represented by the Sears-Haack body, which has the minimum wave drag for a circular cross-section body with the same length and total volume [11]. However, it should be considered that a typical supersonic aircraft will have a configuration that deviates from the

ideal one, risulting in a wave drag that could be twice the one generated by the Sears-Haack body. Equation 4.20 can be used to estimate the wave drag D/q of a given aircraft, with respect to the Sears-Haack wave drag.

$$(D/q)_{wave} = E_{WD}\left[1 - 0.386\,(M-1.2)^{0.57}\left(1 - \frac{\pi\Lambda_{LE}^{0.77}}{100}\right)\right](D/q)_{Sears-Haack} \tag{4.20}$$

Where $(D/q)_{Sears-Haack}$ is the wave drag of the Sears-Haack body, while E_{WD} is an empirical wave drag factor, and represents the ratio between the real wave drag and the ideal one of the Sears-Haack body. Usually a supersonic transport aircraft has E_{WD} which ranges from 1.8 to 2.2.

The induced drag C_{D_i} can be considered proportional to the square of the lift coefficient, at low angles of attack:

$$C_{D_i} = k \cdot C_L^2 \tag{4.21}$$

where the coefficient k is function of the aspect ratio AR and the Oswald efficiency factor e. At subsonic Mach numbers, k can be written as:

$$k = \frac{1}{\pi \cdot AR \cdot e} \tag{4.22}$$

The Oswald efficiency factor accounts for the additional drag generated due to a non-elliptical lift distribution and flow separation. It depends on the wing sweeping angle Λ and can be written as:

$$\Lambda = 0:$$
$$e = 1.78(1 - 0.045\,AR^{0.68}) - 0.64 \tag{4.23}$$
$$\Lambda > 30:$$
$$e = 4.61(1 - 0.045\,AR^{0.68}) - (cos\Lambda)^{0.15} - 3.1 \tag{4.24}$$

For $0° < \Lambda < 30°$, e is evaluated by linear interpolation between the two previous cases. For supersonic Mach numbers, the k factor can be evaluated as:

$$k = \frac{AR \cdot (M^2-1) \cdot cos(\Lambda_{LE})}{\left(4 \cdot AR\sqrt{M^2-1}\right) - 2} \tag{4.25}$$

4.1.3 Torenbeek model

The last model analysed is derived from [27]. It is only applicable to the supersonic flight regime of a generic configuration with a delta or arrow wing. Figure 4.5 shows the reference wing geometry.

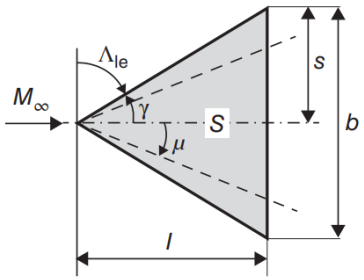

Fig. 4.5 Torenbeek reference delta wing geometry [27]

Linearized theory is used to estimate the basic aerodynamic properties of a flat plate. The Mach number component normal to the wing leading edge influences the aerodynamic forces acting on a wing. Depending on the flight regime (subsonic or supersonic) the relation is different. The flow on a flat delta wing is characterized by the leading edge flow parameter m:

$$m = \frac{\tan\gamma}{\tan\mu} = \beta \cdot \cot(\Lambda_{le}) \tag{4.26}$$

where γ is the complement of the leading edge sweep angle Λ_{le}, $\mu = \sin^{-1}(1/M_{\text{inf}})$ is the Mach angle and $\beta = \sqrt{M_\infty^2 - 1}$. The leading edge flow parameter m is greater than one for supersonic leading edges, while $m < 1$ for subsonic leading edges. The lift coefficient C_L can be evaluated depending on the value of m:

$$\begin{cases} C_L = \frac{4}{\beta}\alpha & , m > 1 \\ C_L = \frac{2\pi m}{E'(m)\cdot\beta} & , m < 1 \end{cases} \tag{4.27}$$

where $E'(m)$ can be written as $E'(m) = 1 + (\pi/2 - 1)m^\eta$, with $\eta = 1.226 + 0.15\pi \cdot (1 - \sqrt{m})$.
The drag coefficient C_D can be expressed as:

$$C_D = C_{D_0} + C_{D_i} = (C_{D_F} + C_{D_{WV}}) + (C_{D_{VL}} + C_{D_{WL}}) \tag{4.28}$$

where the zero-lift drag coefficient is given by the sum of the skin-friction drag coefficient C_{D_F} and the wave drag due to volume coefficient $C_{D_{WV}}$. The induced drag coefficient C_{D_i} is the sum of vortex induce drag coefficient $C_{D_{VL}}$ and the wave drag due to lift $C_{D_{WL}}$.

The skin friction coefficient can be evaluated as:

$$C_F = \frac{0.455}{r_T} \cdot (\log_{10} Re_l - 2.80 \log_{10} r_T)^{-2.58} \tag{4.29}$$

where r_T is a factor which accounts for the kinetic heating due to stagnation of the boundary layer, and can be computed as:

$$r_T = 1 + Pr^{1/3} \frac{\gamma - 1}{2} M_\infty^2 \tag{4.30}$$

where Pr is the Prandtl number, and it can be assumed equal to 0.71 for a turbulent layer in standard conditions Torenbeek2020. The total skin friction drag coefficient can be expressed as:

$$C_{D_F} = K_F \cdot C_F \cdot \frac{S_{wet}}{S} \tag{4.31}$$

where S_wet is the wetted surface, S is the reference surface. The factor K_F is also introduced, to account for non-ideal drag effects due to imperfections. Typically, $K_F = 1.05$ for the fuselage, while $K = 1.15$ for fins. The wave drag due to volume of slender bodies is evaluated considering the ideal Sears-Haack body and experimental data, and the wave drag due to volume coefficient can be expressed as:

$$C_{D_{WV}} = K_{WV} \cdot AR \left(\frac{t}{c} \right) \tag{4.32}$$

where K_{WV} is a factor that accounts for the difference with respect to the ideal Sears-Hack body, and it is related to the Sears-Hack factor K_{SH}:

$$K_{WV} = 2.2 \cdot K_{SH} = 2.2 \cdot \left[1.17 \frac{1 + 1.5\ \beta \cot \Lambda_{le}}{1 + 4\ \beta \cot \Lambda_{le}} \right] \ for\ \ 0.3 \leq \beta \cot \Lambda_{le} \leq 1 \tag{4.33}$$

The induced drag of a delta wing can be generally computed as:

$$C_{D_{VL}} = K_{VL} \frac{C_L^2}{\pi AR} \tag{4.34}$$

where K_{VL} is a factor that accounts for any deviation from the minimum vortex induced drag [27]. It is usually higher than 1 and can be approximated to 1.15 for the early design stages. Eventually, the wave drag due to lift coefficient is evaluated as:

$$C_{D_{WL}} = K_{WL}\frac{\beta\, AR}{8\pi}\beta C_L^2 \tag{4.35}$$

where K_{WL} can also be approximated to 1.15, similarly to the factor K_{VL}.

4.1.4 Comparison of the proposed aerodynamic models

The models presented in the previous sections show different characteristics and range of applicability. For this reason, a short summary is reported here, to highlight the main advantages and disadvanatages of each model. First, the ABH model can be exploited to predict the aerodynamic coefficient of waverider-like configurations, since it has been developed based on a similar (even if much more simple) reference configuration. The same model, indeed, cannot be used for more conventional aircraft shapes, since they differ significantly from the reference one. It can be applied to a wide range of flight regimes, from low Mach numbers to hypersonic velocities. However, its applicability is limited in the transonic regime, between Mach 0.8 and 1.2, due to the complexity of the aerodynamic behaviour in this range.

The other two proposed models, Raymer and Torenbeek, are more suitable to evaluate the aerodynamic coefficients of typical supersonic aircraft configurations. The range of applicability of the Raymer model varies from low subsonic to supersonic speeds at Mach 2. The same limitations of the ABH models exists for Mach numbers around 1. The Torenbeek model, instead, is limited to the supersonic regime and can be used for Mach numbers between 1.2 and 2. For this reason, during the analysis the Raymer model is preferred to compute the aerodynamic coefficients of the supersonic concepts analysed during the research activity.

4.2 Stability and trim analysis

The assessment of the Flight Control System's (FCS) influence on an aircraft layout and performance is a critical aspect when evaluating the feasibility of new concepts, particularly those designed for high-speed operations. Consequently, FCS assumes

a pivotal role in estimating the viability of such aircraft during the conceptual design phase. Once the geometric parameters of the control surfaces are defined and their impact on aerodynamic coefficients is assessed thoroughly, attention shifts to computing their effects on the stability and trimmability of the vehicle. It is essential to emphasize that, in the context of this study, the primary focus was predominantly on longitudinal static stability. The evaluation of lateral stability, although acknowledged as a crucial factor, has been deferred to a subsequent stage of the analysis. The comprehensive methodology employed in this study is summarized in Figure 4.6, which provides an overview of the approach used to address the complexities associated with stability and trim during the conceptual design of high-speed aircraft. This methodological framework ensures an exploration of the reciprocal influence between control surfaces, aerodynamic coefficients, and stability parameters, contributing to a broad understanding of the feasibility of new high-speed concepts.

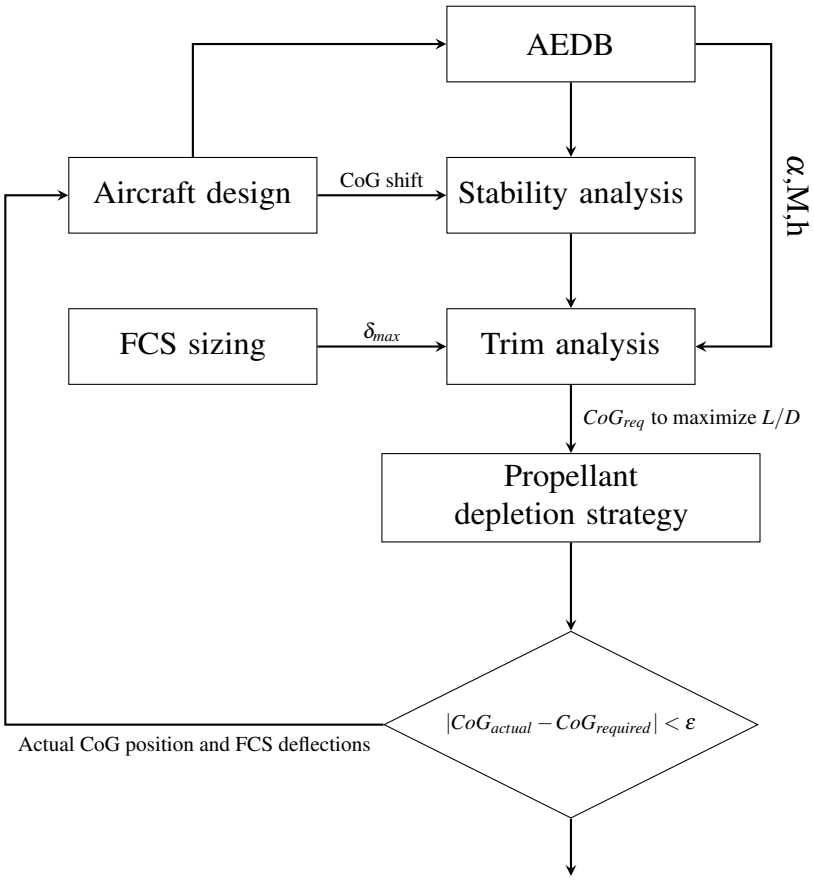

Fig. 4.6 Stability and trim analysis methodology

Moreover, the positioning of the Centre of gravity (CoG) emerges as a critical factor influencing in-flight aerodynamic performance. The location of the CoG plays a pivotal role in assessing the stability and manoeuvrability of an aircraft. Therefore, examining and implementing an appropriate tank distribution and depletion strategy is imperative to mitigate control surface movements, consequently decreasing their adverse impact on the aircraft's overall aerodynamic efficiency, specifically trim drag [85]. By strategically depleting propellant from specific tanks during flight, the CoG can be dynamically adjusted toward the most favourable positions in terms of resulting aerodynamic efficiency. Consequently, the CoG position becomes not only a crucial parameter in ensuring stability, but also a variable that can be actively manipulated to enhance aerodynamic performance. As depicted in Figure 4.6, the utilization of the aerodynamic database becomes instrumental in examining the stability of the vehicle, a factor directly tied to the positioning of the CoG, which is an outcome of the aircraft design process. The validation of longitudinal static stability involves assessing whether the pitching moment coefficient C_{M_y} exhibits a decrease with increasing angles of attack. The equation governing the pitching moment coefficient is presented in Equation 4.36.

$$C_{M_y} = C_{M_0} + C_{M_\alpha} \cdot \alpha \tag{4.36}$$

The total pitching moment coefficient can be evaluated following an incremental build-up approach [71]. First, the clean configuration, which consists of the external vehicle layout including undeflected control surfaces, is investigated. Then, once additional details on the integration of both the propulsive flow-path and the deflections of the control surfaces are available, the aerodynamic database can be updated including these new contributions. The total pitching moment coefficient can be evaluated as:

$$C_{M_y} = \left(C_{M_y}\right)_{clean} + \sum_{i=1}^{n} \left(\Delta C_{M_y}\right)_i + \left(\Delta C_{M_y}\right)_T \tag{4.37}$$

In Equation 4.37 the pitching moment coefficient is expressed as the sum of three contributions, which are the pitching moment coefficients of the clean configuration, the sum of the individual effects of the flight control surfaces and the additional effect due to the misalignment between the thrust vector and the vehicle's longitudinal axis. Given the Mach number and the position of the CoG, the assessment of aircraft stability and trim involves considering every combination of control surfaces deflections $(\delta_1, ..., \delta_{i-th})$. The contribution to the pitching moment coefficient associated with

each control surface deflection is known, and allows for the evaluation of the overall aerodynamic coefficients. First, longitudinal static stability is checked, examining the variation of the C_{My} as a function of α, verifying that:

$$C_{My_\alpha} = \partial C_{My}/\partial\alpha < 0 \tag{4.38}$$

Once the stability is verified, the trim conditions can be identified imposing that $C_{My} = 0$. It is noteworthy that achieving the same trimmed angle of attack, denoted as α_{trim}, is possible through various combinations of control surface deflections. In the context of high-speed vehicles, the choice of control surface deflection combinations that maximize the overall aerodynamic efficiency can be advantageous. Moreover, the position of the CoG can be modified, by selecting an appropriate propellant depletion strategy. This can be done iteratively, until the achieved position of the CoG at a given Mach number corresponds to the optimal one, given a certain error ε, selected depending on the configuration analysed. The algorithm delineated in Equation 4.39 has been employed to calculate the combinations of minimal deflection angles of the control surfaces δ_{min} required to achieve trim for a specific flight condition, characterized by a given Mach number and CoG position.

$$\begin{aligned} &given : Mach\ number,\ x_{CoG} \\ &find : \delta_{min} \rightarrow C_{My_{tot}} = 0,\ for\ each\ \alpha \end{aligned} \tag{4.39}$$

4.3 Mission simulation

Detailed mission simulation is typically reserved for later stages of the design process. However, the proposed methodology involves the utilization of mission simulation since the very early phases of the conceptual design stage. At each iteration, as soon as updated data becomes available, the simulation is exploited to assess the vehicle's performance along the trajectory and to verify the feasibility of the reference mission. The early integration of mission simulation not only facilitates a more robust evaluation of the conceptual design's viability but also ensures that potential design iterations are informed by a comprehensive understanding of the vehicle's anticipated performance within the mission context. Mission simulation is performed using the ASTOS software, by Astos Solutions GmbH [88]. The first step consists of providing three types of required inputs to the tool, which are the

environment, the vehicle model description and the different flight phases. The US standard atmosphere model [89] is used, and no cross-wind is considered. To specify the vehicle model accurately, it is necessary to provide the main geometric data of the vehicle:

- aircraft structural mass (which is equal to the Operative Empty Weight (OEW) plus the Payload);
- propellant mass;
- aircraft length;
- wing-span;
- aircraft height.

Moreover, the aerodynamic and propulsive databases are also exploited for the simulation. Typically, C_L and C_D coefficients are expressed as a function of altitude and angle of attack. To provide an example of the database structure, Table 4.2 reports an excerpt of the STRATOFLY vehicle aerodynamic database.

Table 4.2 Excerpt of the STRATOFLY aerodynamic database

Mach [-]	Alpha [deg]	C_L[-]	C_D[-]
0.5	-2	0.118	0.021
0.5	0	0.160	0.028
0.5	+2	0.220	0.041
...	...	...	...
8	-2	0.020	0.004
8	0	0.042	0.006
8	+2	0.064	0.010

The propulsive database contains the data of thrust and fuel massflow as a function of altitude, Mach and equivalence ratio. The last parameter is varied to achieve scaled thrust and mass flow, and it is considered here as a way to modify the throttle during the different phases of the mission. An example of the propulsive database is reported in Table 4.3.

Table 4.3 Excerpt of the STRATOFLY propulsive database

Altitude [km]	Mach [-]	Equiv ratio [-]	Thrust [kN]	Fuel massflow [kg/s]
0	0.30	0.5	1167.27	26.64
0	0.30	1	2334.55	53.28
0	0.44	0.5	994.15	26.68
0	0.44	1	1988.30	53.36
...	...	...	...	
32	8	0.5	164.38	11.71
32	8	1	523.49	22.34

Then, the mission phases should also be defined before performing the complete mission simulation. The following phases are generally considered for a generic high-speed passenger transport trajectory:

- Take-off
- Subsonic climb
- Subsonic cruise (if applicable)
- Supersonic climb
- Hypersonic climb (if applicable)
- Cruise
- Descent
- Final approach and landing

However, it should be highlighted that the simulation starts at the end of the take-off phase, since the runway acceleration cannot be properly simulated with ASTOS. For the same reason, the landing phase is also not considered. Moreover, the phases listed are supposed to represent a generic high-speed mission, but some phases can be neglected depending on the specific concept analysed. Eventually, once all the required data are available, the simulation can be initiated.

First, an initial mission simulation is conducted considering the preliminary aerodynamic data, evaluated through simplified models. Then, the higher fidelity

data of the vehicle's clean configuration is exploited for a second iteration. Eventually, after incorporating the impact of the flight control surfaces into the aerodynamic database, an additional simulation can be performed. However, there is one main limitation to consider: ASTOS cannot conduct a static stability and trim analysis. Due to this constraint, the trimmed conditions are evaluated independently for each Mach number (as described in section 4.2) and subsequently, they are used to generate a trimmed aerodynamic database. Therefore, as a final step, different mission simulations are carried out, considering the trimmed aerodynamic database and different possible routes.

4.4 Regulatory framework

High-speed passenger aircraft are anticipated to integrate into the established airport infrastructure, adhering to the standard operational procedures designed for subsonic aircraft. Despite this aim, the distinctive features of high-speed concepts may deviate from existing operations, potentially necessitating a re-assessment of operational procedures. When compliance with current standards proves challenging, a comprehensive analysis of requisite modifications to operational procedures becomes imperative. Drawing parallels to the historical case of the Concorde, the identified adjustments in operational procedures serve as a robust foundation for negotiating and formulating specialized operational procedures adapted for upcoming high-speed vehicles.

4.4.1 Take-off and landing distances

Initially, an examination of the compliance between required take-off and landing distances with the existing airports' infrastructure is conducted. This investigation places particular emphasis on comparing high-speed vehicle operations with traditional aircraft procedures, focusing on regulatory guidelines for take-off and landing distances in both standard and failure scenarios. To conform with global ground infrastructure standards, the maximum field lengths for both take-off and landing are set at 4000 m. This encompasses a 15% safety margin on the take-off path (as specified by CS 25.113 [90]) and a 66.7% safety margin on the landing path (as in CS 25.125 [90]). All calculations are conducted under the assumptions of a dry runway

and non-icing conditions at sea level. This analysis forms the basis for ensuring the compatibility of high-speed vehicles with current airport facilities and international aviation standards.

The following take-off reference available distances should be considered in the analysis [91][92], as shown in Figure 4.7:

- Take-Off Run Available (TORA), which is the length of the runway available and suitable for the ground run of an aircraft taking off;
- Accelerate-Stop Distance Available (ASDA), which is the length of runway plus the length of any associated stopway (if available);
- Take-Off Distance Available (TODA), which is the length of the runway plus the length of any associated clearway (if provided).

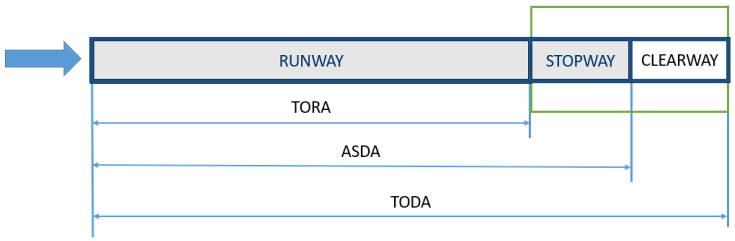

Fig. 4.7 Take-off reference distances

Three additional distances should be evaluated for the specific aircraft and later compared to the available distances: the calculated distances should be lower than the available ones to guarantee compliance with regulations.

First, the Take-Off Distance (TOD) is computed, which is defined as the greater value between:

- TOD_{n-1} (Figure 4.8): distance covered from the brake release to a point at which the aircraft is 35 ft above the take-off surface, assuming the failure of the critical engine at V_1;
- TOD_n (Figure 4.9): 115% of the distance covered from brake release to a point at which the aircraft is 35 ft above the take-off surface, assuming all engines operating.

where V_1 is the take-off decision speed, i.e. the velocity beyond which take-off should no longer be aborted. It can be evaluated considering that in the event of an engine failure at V_1, the distance required to perform the take-off is equal to the distance needed to stop the aircraft (CS 25.107) [90].

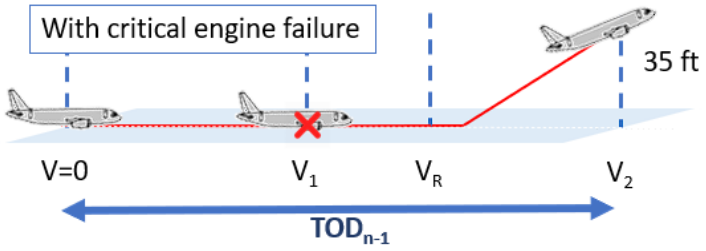

Fig. 4.8 Take-Off Distance with critical engine failure TOD_{n-1}

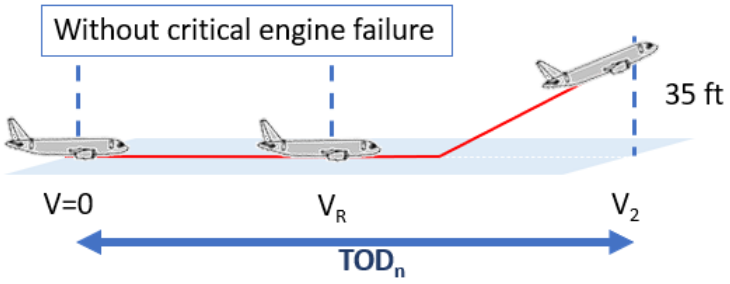

Fig. 4.9 Take-Off Distance (TOD) without critical engine failure TOD_n

The second distance is the Take-Off Run (TOR), which is defined as the greater between the following values:

- TOR_{n-1} Figure 4.10: distance covered from brake release to a point equidistant between the point at which V_{LOF} is reached and the point at which the aircraft is 35 ft above the take-off surface, assuming the failure of the critical engine at V_1.
- TOR_n Figure 4.11: 115% of the distance covered from brake release to a point at which the aircraft is 35 ft above the take-off surface, assuming all engines operating.

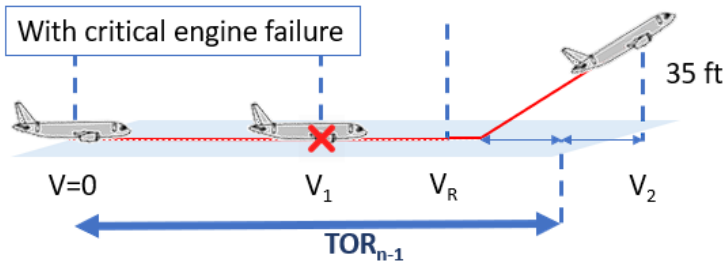

Fig. 4.10 Take-Off Run without critical engine failure TOR_n

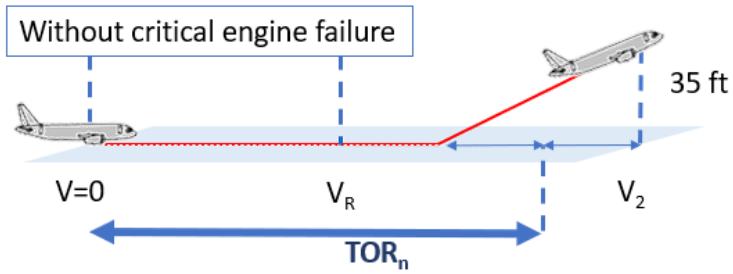

Fig. 4.11 Take-Off Run (TOR)

The third distance is the Accelerate&Stop Distance (ASD), which is the sum of the distances necessary to:

- accelerate the airplane with all engines operating to V_1, assuming the critical engines fail at V_1 and the pilot takes the first action to reject the take-off at V_1;
- a distance equivalent to 2 seconds at constant V_1 speed;
- distance necessary to come to a full stop.

The theoretical Take-Off Run at sea level can be computed as:

$$d_R = \frac{1}{2b} \cdot \left(\ln a - \ln(a - b \cdot V_2^2)\right) \tag{4.40}$$

with:

$$a = g \cdot \left(\frac{T}{g \cdot MTOW} - f\right) \tag{4.41}$$

$$b = \frac{\left(C_{D_0} - f^2/4k\right) \cdot \rho \cdot g}{2 \cdot MTOW \cdot g/S_{wing}} \tag{4.42}$$

where:

- a is the acceleration of the aircraft on ground;
- f is the rolling friction factor;
- C_{D_0} is the drag coefficient at zero lift;
- k is the Oswald correction factor;
- T is the take-off thrust;
- V_2 is the initial climb speed.

The total take-off distance shall also consider the lift-off distance and the manoeuvring distance, computed as:

$$d_{LO} = t_{LO} \cdot V_2 \tag{4.43}$$

$$d_M = \frac{V_2^2 \cdot sin(\gamma_0 \cdot \pi/180)}{(n_z - 1) \cdot g} \tag{4.44}$$

where:

- t_{LO} is the time required to perform the rotation.
- n_z is the contingency factor along z at take-off;
- γ_0 is the climb path angle;

Furthermore, a similar approach is followed for the landing phase, where the Landing Distance Available (LDA) is evaluated. It is defined as the length of the runway available and suitable for the ground landing run of an aeroplane. The landing distance for a given aircraft should be evaluated as the distance covered by the aircraft from a 50 ft obstacle above the runway threshold and the point where it comes to a complete stop, as shown in Figure 4.12.

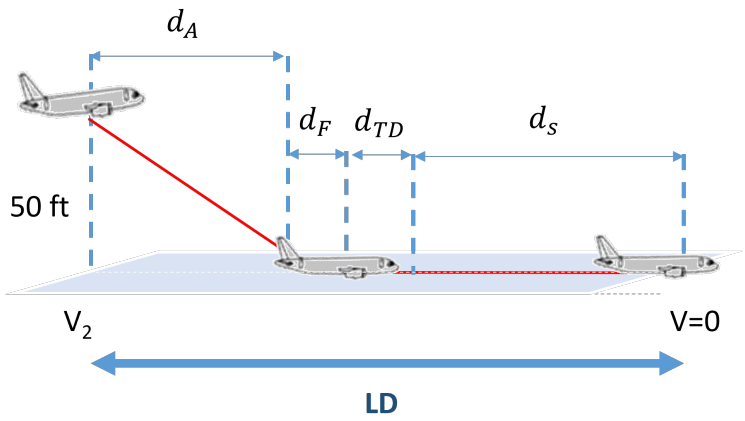

Fig. 4.12 Landing distance

The theoretical landing distance can be computed as:

$$d_{LDG} = d_A + d_F + d_{TD} + d_s \tag{4.45}$$

where d_A is the approaching distance (Equation 4.46), d_F is the flare distance (Equation 4.47), d_{TD} is the touch-down distance (Equation 4.48), and d_s is the landing run (Equation 4.49).

$$d_A = \frac{h_{0_{LDG}}}{\tan\gamma} \tag{4.46}$$

$$d_F = \frac{V_{LDG}^2}{(n_{z_{LDG}}) \cdot g} \left[\sin\gamma - \left(\frac{1-\cos\gamma}{\tan\gamma} \right) \right] \tag{4.47}$$

$$d_{TD} = V_{LDG} \cdot t_{TD} \tag{4.48}$$

$$d_s = \frac{V_{LDG}^2}{2 \cdot n_{x_{LDG}} \cdot g} \tag{4.49}$$

where:

- $h_{0_{LDG}}$ is the landing obstacle clearance;
- γ is the glide scope angle;
- V_{LDG} is the final landing speed;

- $n_{z_{LDG}}$ is the contingency load at landing along z-axis;
- $n_{x_{LDG}}$ is the contingency load at landing along x-axis;
- t_{TD} is the time required to complete touch-down.

4.4.2 Environmental regulations

As highlighted in section 2.3, there are multiple issues associated with high-speed flight, including greenhouse gases, pollutant and noise emissions. For subsonic aircraft, they are currently regulated through ICAO annex 16, in Volume I (noise), Volume II (pollutant emissions), and Volume III (CO_2 emission standard). The International Civil Aviation Organization's Committee for Aviation Environmental Protection (ICAO-CAEP) has embraced the task of examining noise and emissions features of contemporary supersonic transport. This initiative aims to reassess and enhance current standards while also formulating future certification criteria. Since the CAEP/10 cycle (2013-16), both CAEP's Working Groups, WG1 (focused on noise) and WG3 (concentrating on emissions), have incorporated tasks related to SSTs in their work program [5].

The research activity presented in this thesis is mainly focused on the CO_2 emissions standard, since it presents the major link with the aerodynamic and propulsive characteristic together with the aircraft's performance along the reference trajectory, which are the main topics analysed in this work.

A CO_2 emission standard has been established for subsonic airplanes, as outlined in ICAO Annex 16 Volume III [93]. The certification process of any aircraft type is connected to the assessment of a CO_2 metric value ($CO_2\ MV$), which is compared to the applicable limit defined in ICAO Annex 16 Volume III [93], as a function of the aircraft's certificated Maximum Take-Off Mass (MTOM). The CO_2 metric value is an estimation of the technology performance of a given aircraft related to its fuel efficiency, and can be expressed as:

$$CO_2\ MV = \frac{(1/SAR)_{avg}}{RGF^{0.24}} \tag{4.50}$$

where:

- SAR is the Specific Air Range (inverse of specific fuel consumption), which is evaluated in cruise conditions at three different aircraft weights;
- RGF is the Reference Geometry Factor, which is the area of the fuselage surface bounded by the maximum width of the fuselage outer mould line (OML) projected to a flat plane parallel to the main deck floor (Figure 4.13). It approximates the amount of usable space in the fuselage.

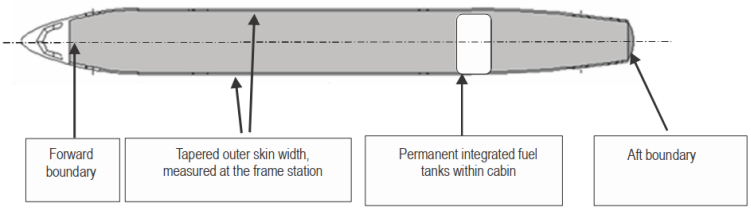

Fig. 4.13 Reference Geometry Factor

A notable characteristic of this metric system is its capacity to encompass all existing subsonic aircraft categories under a single regulatory level based on MTOM. According to present regulations, SAR is evaluated at three reference mass points in cruise, defined as:

$$\begin{aligned} &High\ gross\ mass\ point = 0.92 \cdot MTOM \\ &Low\ gross\ mass\ point = (0.45 \cdot MTOM) + \left(0.63 \cdot MTOM^{0.924}\right) \\ &Mid\ gross\ mass\ point = average\ of\ high\ and\ low\ masses \end{aligned} \tag{4.51}$$

These points are assessed in steady unaccelerated straight and level flight, considering the ICAO standard day atmosphere. However, it should be highlighted that reference gross masses are defined for subsonic aircraft only, and they may not be representative of typical cruise flight conditions of high-speed concepts. For this reason, the mass points are first evaluated according to the current regulations, to estimate to what extent they are capable of representing supersonic aircraft operations. In case this is not verified, possible corrections to the equations should be considered, to move towards a standard specifically tailored for high-speed vehicles. The difference between the subsonic and supersonic case is mainly due to the higher relative fuel consumption during the mission of a high-speed aircraft with respect to the subsonic case. Moreover, the comparable velocities of the subsonic categories permit the

exclusion of a speed-related term from the existing metric system. Nonetheless, for supersonic aircraft, the introduction of a speed parameter could be beneficial, and it could potentially increase the contribution of carrying capacity and range. On the contrary, the total amount of fuel consumption is higher, and it would be not possible to abide by the present regulatory framework.

Currently, no civil supersonic aircraft is operating, and acquiring adequate data may become challenging. Technical data are necessary to gain a more comprehensive understanding of attainable CO_2 emissions across a spectrum of aircraft sizes and configurations at various Mach numbers.

Moreover, high-speed aircraft operate within substantially distinct aerodynamic conditions, characterized by fundamentally different principles of physics when compared to subsonic flight, and they rely on significantly different propulsion and airframe technologies. Considering all these factors, it becomes clear that significant adjustments may be necessary to make the subsonic $CO2$ standard relevant and applicable to high-speed transport. A similar approach should be followed for the re-definition of the RGF, since it does not consider other factors than the surface of the cabin, while other parameters could be more fit to describe the cabin, such as its volume.

Chapter 5

Results

This chapter presents the results obtained following the proposed methodology, described in Chapter 4. First, the preliminary aerodynamic models are analysed to derive simplified formulations which can be used to predict the aerodynamic coefficients of a given high-speed configuration during the conceptual design stage. The results of this analysis conducted for both waverider vehicles and wing-body aircraft are presented in section 5.1. Then, the static stability and trim analysis has also been studied, considering the waverider STRATOFLY MR3 vehicle as a reference (section 5.2). The impact of the deflection of the control surfaces, needed to guarantee stable and trimmed flight, is also analysed and reported in subsection 5.2.1. The take-off and landing requirements have been also studied, and the results are shown in section 5.3. Eventually, the complete set of technical data evaluated during the research activity has been exploited as a baseline for the study on the $C0_2MV$, which is reported in section 5.4.

5.1 Aerodynamic modelling

This chapter presents the results of the preliminary aerodynamic analysis conducted evaluating different types of vehicle configurations depending on the flight regime:

- the classical wing-body configuration is considered for supersonic Mach numbers (up to Mach 3);
- the waverider configuration is considered for hypersonic Mach numbers.

Depending on the configuration type, the most appropriate reference model can be used to evaluate the aerodynamic coefficients, among the models presented in section 4.1: All-Body Hypersonic (subsection 4.1.1), Raymer (subsection 4.1.2) and Toreenbek (subsection 4.1.3). The All-Body Hypersonic is the most suitable for the waverider configurations, while the other two models can be used to characterize the wing-body configurations. The following sections present the results obtained applying those models to the case studies considered within the research activity.

5.1.1 Waverider configuration preliminary aerodynamic analysis

The first configuration to be analysed is the STRATOFLY Mach 8 waverider. The All-Body Hypersonic model is considered for the preliminary evaluation of the vehicle aerodynamic coefficients. The results are later compared to the CFD data available for this configuration to estimate the model accuracy and to derive possible modifications to improve its capability. The lift and drag coefficients calculated at subsonic Mach numbers equal to 0.5 and 0.7 are reported in Figure 5.1 and Figure 5.2, respectively. Here, the data obtained from the ABH model are compared to the ones evaluated through CFD analysis. The clean configuration is considered for both analyses, and the deflection of the flight control surfaces is not included.

Subsonic regime

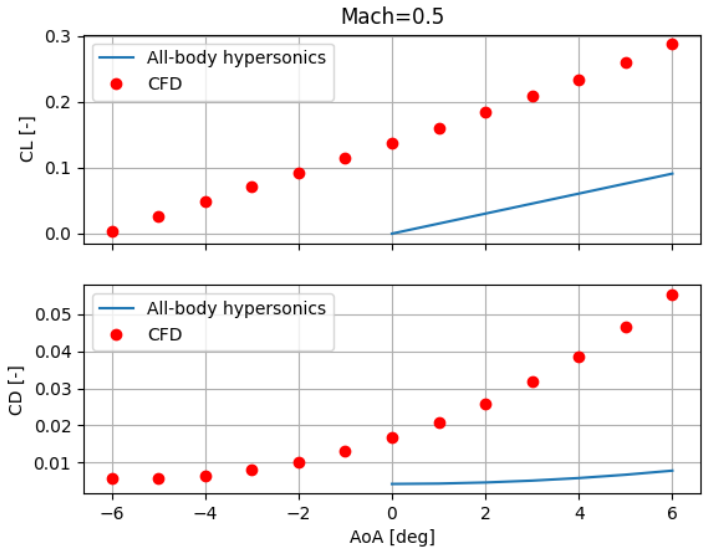

Fig. 5.1 Comparison of C_L and C_D evaluated with ABH model and CFD analysis at Mach 0.5

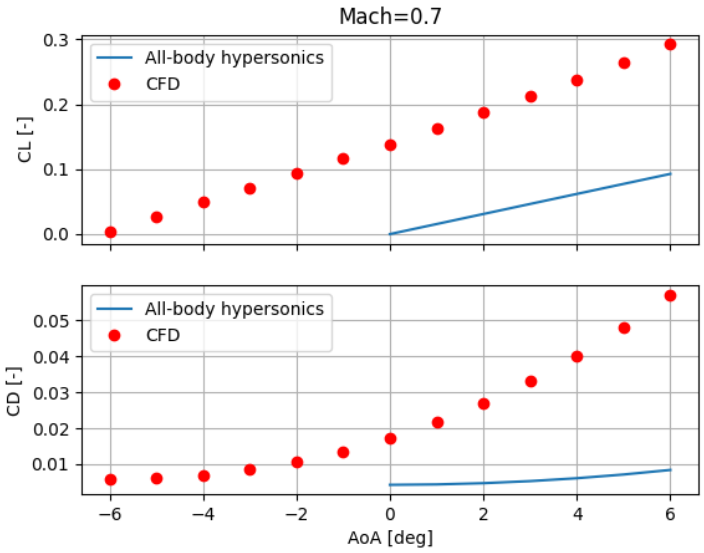

Fig. 5.2 Comparison of C_L and C_D evaluated with ABH model and CFD analysis at Mach 0.7

First, it can be noticed that the model cannot predict the lift coefficient at zero angle of attack C_{L_0}, which is assumed to be zero. The lift curve slope is also lower than the one of the CFD data, with a difference of $\sim 35\%$ between the model and the CFD data.
Then, the drag coefficient is computed and compared to the CFD data. The C_D computed by the ABH model is lower than the one estimated through CFD analysis. In particular, both the parasite and induced drag are lower than expected. This outcome can be explained by considering the higher complexity of the waverider configuration compared to the reference configuration, which was used as a baseline for developing the ABH model. The STRATOFLY MR3 vehicle has an asymmetric shape and an internal propulsive duct, which differs from the ABH model reference configuration. This has a significant impact on the overall aerodynamic performance.

Similar results are also found for the transonic regime, as can be seen in Figure 5.3 and Figure 5.4, for Mach 0.95 and Mach 1.2. The aerodynamic coefficients at Mach 2, Mach 5 and Mach 8 are reported in Figure 5.5, Figure 5.6 and Figure 5.7. The estimation of the lift curve slope is slightly more precise at higher Mach numbers, where the difference between the predicted slope and the CFD decreases to values between 20% and 30%. Quite the opposite, C_D is still underestimated at supersonic and hypersonic Mach numbers.

Transonic regime

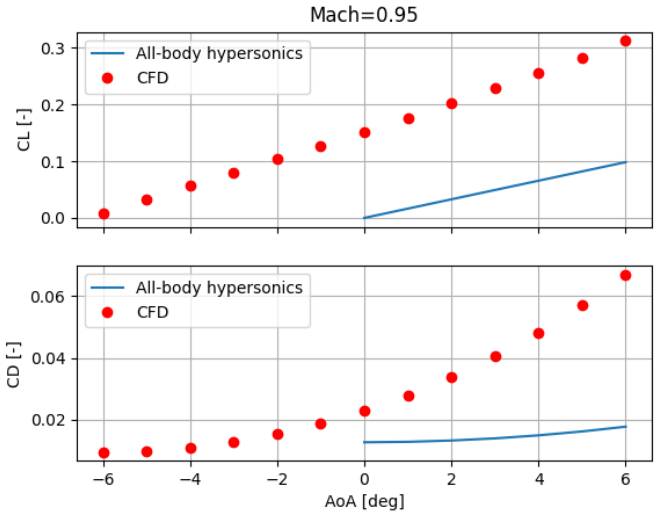

Fig. 5.3 Comparison of C_L and C_D evaluated with ABH model and CFD analysis at Mach 0.95

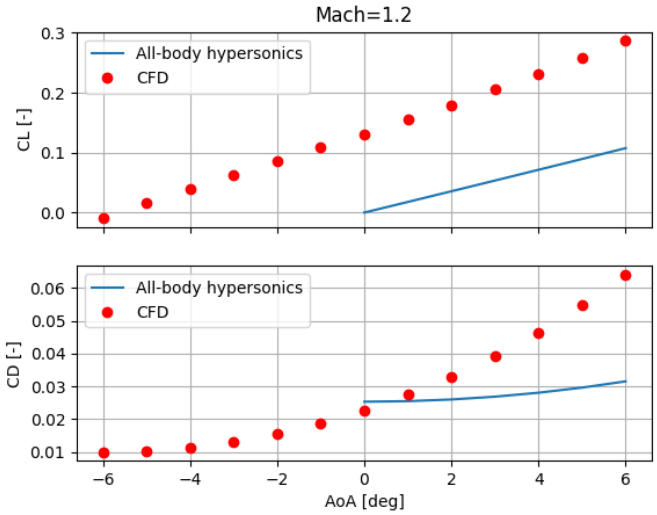

Fig. 5.4 Comparison of C_L and C_D evaluated with ABH model and CFD analysis at Mach 1.2

Supersonic regime

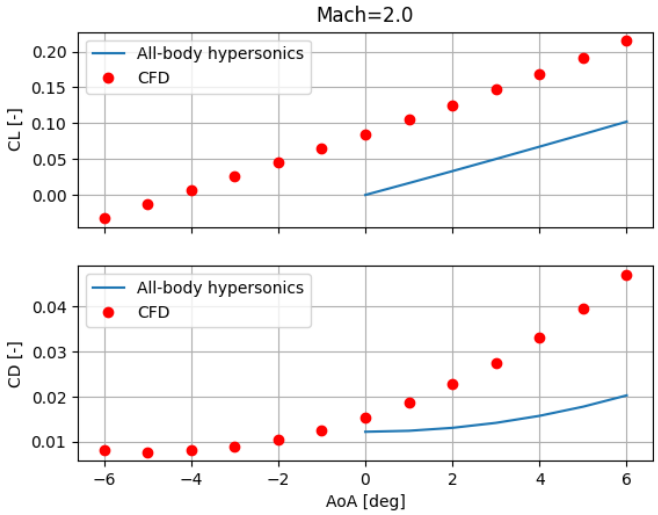

Fig. 5.5 Comparison of C_L and C_D evaluated with ABH model and CFD analysis at Mach 2

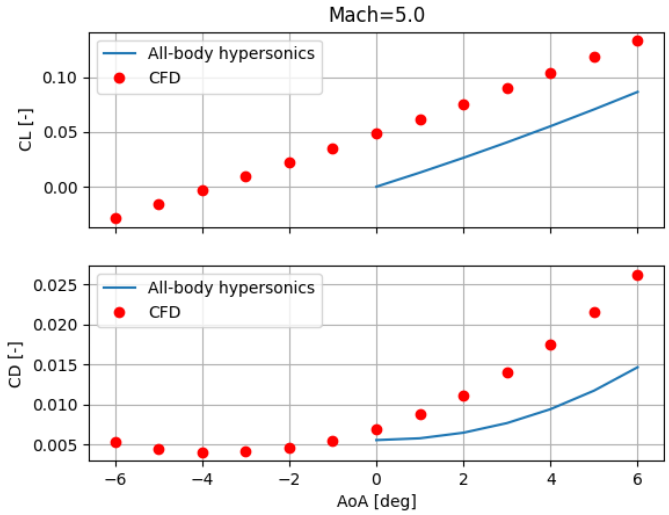

Fig. 5.6 Comparison of C_L and C_D evaluated with ABH model and CFD analysis at Mach 5

Hypersonic regime

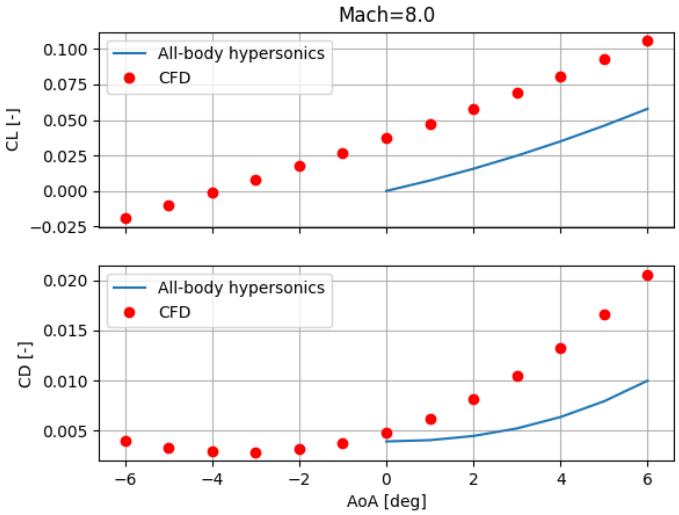

Fig. 5.7 Comparison of C_L and C_D evaluated with ABH model and CFD analysis at Mach 8

From previous comparisons, it is clear that some corrections are needed to improve the estimation of the aerodynamic coefficients through the ABH model. For that reason, the aerodynamic database of the STRATOFLY MR3 vehicle is considered as a basis to identify possible corrections. First, the lift coefficient at zero angle of attack is introduced, by exploiting the data available for this configuration. As there is no additional information on this parameter, the same C_{L_0} computed with CFD analysis has been included. It should be noted that this is a strong approximation, since C_{L_0} may vary depending on the shape of the wing and vehicle. However, considering that this model will be used to characterize the MR5 vehicle, which is directly derived from the STRATOFLY MR3, it is possible to suppose that those values will be still valid, as a first approximation. Moreover, since the estimation of the lift coefficient curve was already relatively precise at each Mach number, no other modifications are included for the evaluation of the C_L.
The updated values for the lift coefficient are also used as an input to re-evaluate the C_D at the different Mach numbers. In addition to that, the friction drag coefficient is computed exploiting a different formulation than the one suggested in the ABH model. An updated mathematical formulation for viscous effect corrective factor has been presented in [71], within the framework of the H2020 STRATOFLY project. The formulation, already available in the literature, has been modified to better

capture the peculiarities of highly integrated waverider configurations:

$$C_{D_{fB}} = \alpha \cdot \frac{1}{[\log(Re)]^{2.58}} \cdot \frac{1}{(1+\beta \cdot M^2)^{\gamma}} \cdot \frac{S_{wet}}{S_{ref}} \tag{5.1}$$

The parametric formulation presented in Equation 5.1 originates from the turbulent flat plate theory $\frac{1}{[\log(Re)]^{2.58}}$, which is corrected to account for compressibility effects through the factor $\frac{1}{(1+\beta \cdot M^2)^{\gamma}}$. Moreover, the parameters α, β and γ can be customized depending on the configuration type. The original formulation was derived for the SpaceShip2 aerodynamic characterization. However, due to the very different shape of the STRATOFLY MR3 and the SpaceShip2 vehicle, the three parameters have been evaluated again [71], considering the STRATOFLY configuration:

$$\alpha = 0.43,\ \beta = 0.31\ and\ \gamma = 0.37 \tag{5.2}$$

Eventually, an additional modification is included for the computation of the drag coefficient. The ABH model refers to a simple symmetric configuration, so the computed C_D vs α are also symmetric with respect to $\alpha = 0$. For the specific case of the analysed waverider vehicle, this is not verified any more. The CFD data show a different trend, and the minimum drag is found for an angle of attack lower than zero. To account for this shift of the drag coefficient curve, a translation of the curve is included in the modified version of the ABH model. An increased angle of attack of 4° is considered when evaluating the C_D. Even if the actual angle varies with the Mach number, the minimum drag is always found in the close range of $\alpha = -4^\circ$, which is selected as the reference value for all the Mach numbers. The Equation 4.5 can now be written as:

$$C_D = C_{D_0} + C_{D_i} = C_{D_0} + [k_m \cdot C_L \cdot \tan(\alpha + \mathbf{4})] \tag{5.3}$$

The results for the subsonic regime are reported in Figure 5.8 and Figure 5.9, while Figure 5.10 and Figure 5.11 show the results for Mach 0.95 and Mach 1.2. The aerodynamic coefficient evaluated at mach 2, Mach 5, and Mach 8 are reported in Figure 5.12, Figure 5.13, and Figure 5.14. The comparison of the lift coefficient obtained with the modified ABH model and the one resulting from CFD analysis shows good accordance between the two cases for the entire Mach numbers range. The accuracy in the evaluation of the drag coefficient is also increased, thanks to the proposed modifications. The C_D is slightly overestimated at low Mach numbers, and

at supersonic speed a similar trend is also found. At subsonic Mach numbers, the error between the C_D estimated with ABH model and CFD is in the range between 75% and 85%, while it decrease to values between 10%-19% if the suggested corrections are included. For transonic speeds, the error is reduced from 45%-60% to 15%-27%, depending on the Mach number and angle of attack at which the C_D is computed. At Mach 2 and $\alpha = 0°$, the same accuracy is found for both cases ($\simeq 20\%$), even if C_D is slightly underestimated intially, and then overestimated with the corrected model. For higher angles of attack the modified ABH model shows improved estimations: for example at $\alpha = 2°$ the error decreases from 42% to 24%. Similar results are also found for Mach 5, where at $\alpha = 2°$ the error with respect to the CFD data is reduced from 42% to 33%. Finally, at cruise Mach number equal to 8 there is not an improvement at $\alpha = 0°$, while for higher angles of attack ($\alpha = 2°$) the error decreases from 45% to 17%.

Subsonic regime

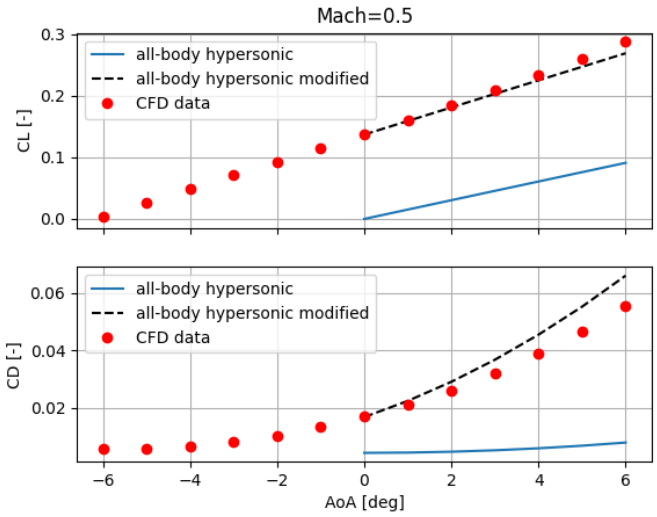

Fig. 5.8 Comparison of C_L and C_D evaluated with ABH model, modified version of ABH model and CFD analysis at Mach 0.5

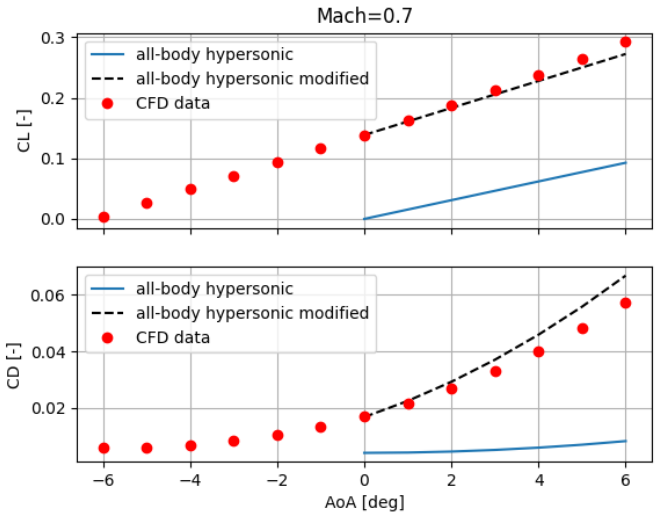

Fig. 5.9 Comparison of C_L and C_D evaluated with ABH model, modified version of ABH model and CFD analysis at Mach 0.7

Transonic regime

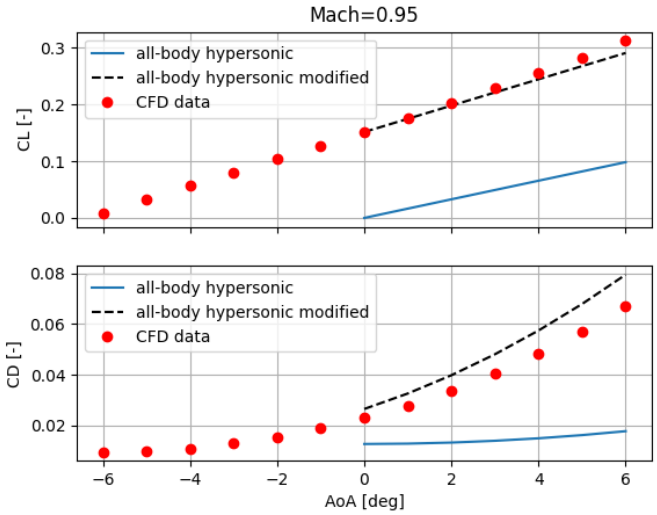

Fig. 5.10 Comparison of C_L and C_D evaluated with ABH model, modified version of ABH model and CFD analysis at Mach 0.95

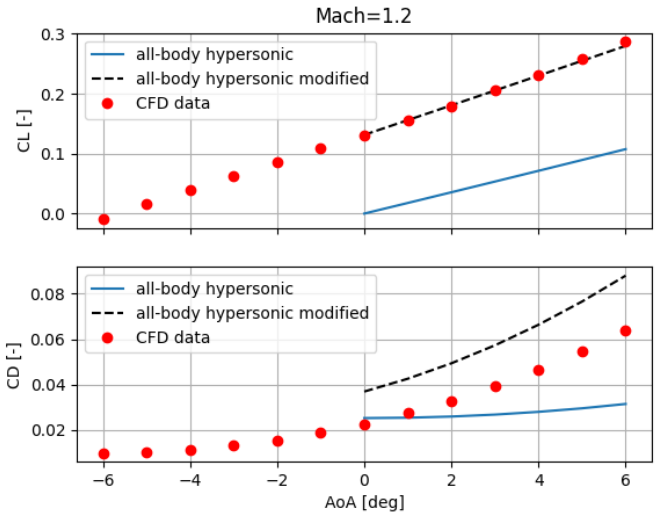

Fig. 5.11 Comparison of C_L and C_D evaluated with ABH model, modified version of ABH model and CFD analysis at Mach 1.2

Supersonic regime

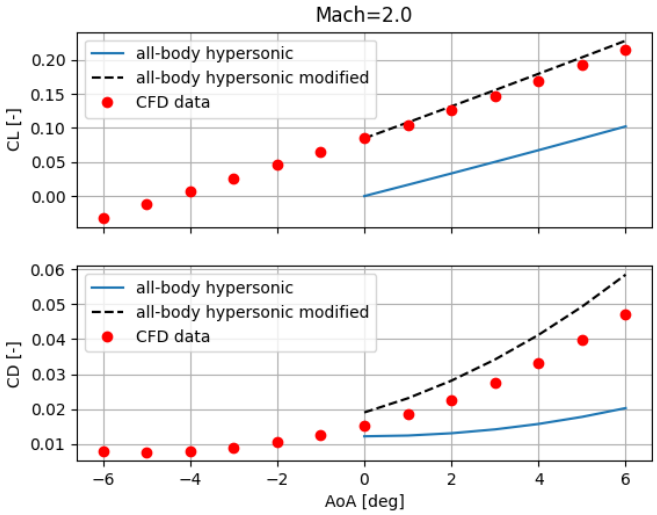

Fig. 5.12 Comparison of C_L and C_D evaluated with ABH model, modified version of ABH model and CFD analysis at Mach 2

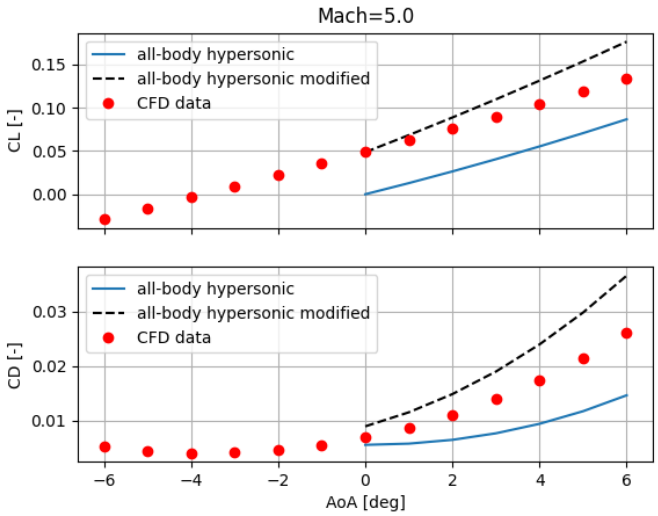

Fig. 5.13 Comparison of C_L and C_D evaluated with ABH model, modified version of ABH model and CFD analysis at Mach 5

Hypersonic regime

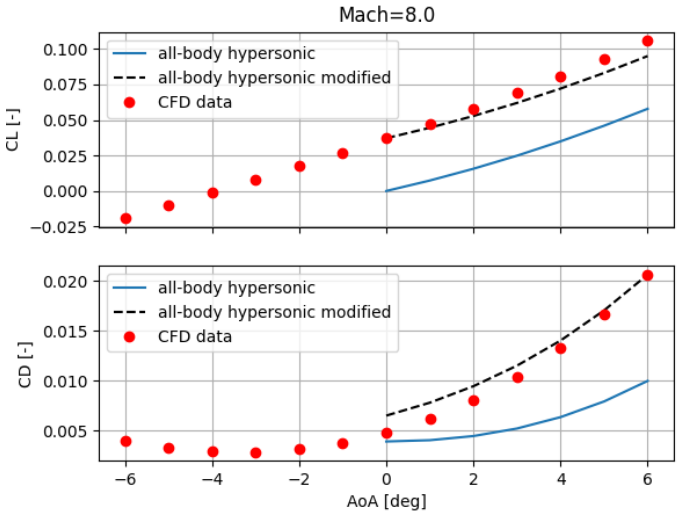

Fig. 5.14 Comparison of C_L and C_D evaluated with ABH model, modified version of ABH model and CFD analysis at Mach 8

C_L and C_D as a function of Mach number are also reported in Figure 5.15 and Figure 5.16, for $\alpha = 0°$ and $\alpha = 1°$. At subsonic Mach numbers, the C_D is largely underestimated if the ABH model is used, and the difference between the

C_D computed with the reference ABH and CFD data is equal to $\simeq 75\%$. When the proposed modifications are introduced, this error decreases to 1%-5%. However, at higher speed the original ABH model is already relatively accurate in predicting the C_D. Here, the error is in the order of the 20%. When the modifications are introduced, the drag coefficient is overestimated of approximately 25%-30%. Even if the accuracy is not increased at $\alpha = 0^\circ$, the major benefits are seen for higher angles of attack. For example, at $\alpha = 2^\circ$ the error decreases from 40%-45% to 16%-33% between Mach 5 and 8. An overview of the computed accuracy of the ABH model and the modified version is reported in Table 5.1. As mentioned previously, the improvements are clear for subsonic Mach numbers, while at supersonic speed the major achievements are obtained for increasing angles of attack. At $\alpha = 0^\circ$ the accuracy of the modified model is similar or reduced with respect to the original one. However, the latter is underestimating the drag coefficient, while the ABH modified model is overestimating it. This can be considered as a conservative estimation, which could guarantee still a sufficiently good evaluation of the vehicle performance. Moreover, this choice allow to obtain a more realistic trend of the drag coefficient variation at increasing Mach numbers.

Table 5.1 Summary of computed errors in estimating the C_D for the original and modified ABH model with respect to CFD data of the MR3 vehicle

	$\alpha = 0^\circ$		$\alpha = 2^\circ$	
Mach	ABH [%]	ABH modified [%]	ABH [%]	ABH modified [%]
0.5	75	1	82	12
0.7	75	2	82	9
0.95	45	15	60	18
1.2	11	65	20	50
2.0	20	24	42	24
5.0	20	30	41	33
8.0	19	35	45	16

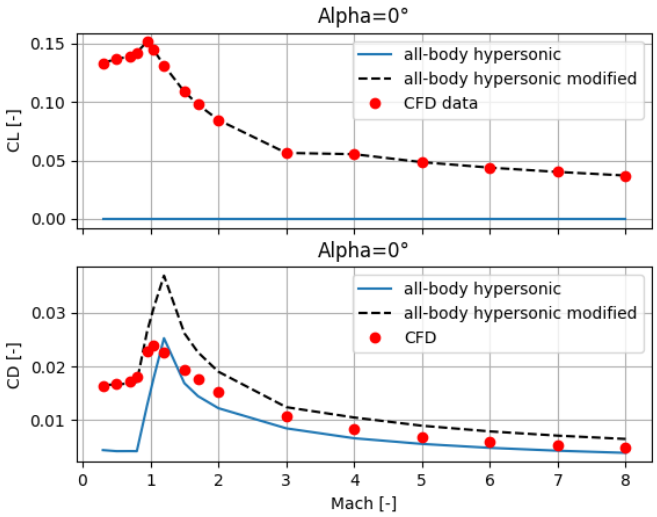

Fig. 5.15 Comparison of C_L and C_D evaluated with ABH model and CFD analysis at $\alpha = 0°$

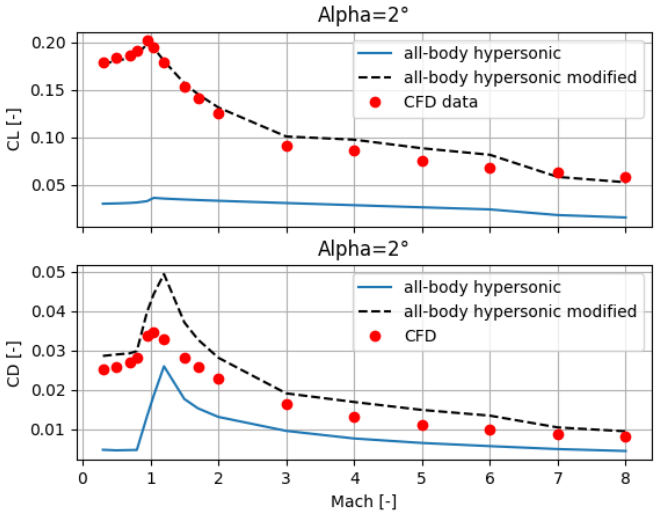

Fig. 5.16 Comparison of C_L and C_D evaluated with ABH model and CFD analysis at $\alpha = 2°$

5.1.2 Waverider configuration preliminary aerodynamic analysis: validation with Mach 5 waverider

The additional case study of a Mach 5 waverider, presented in section 3.5, is considered as a validation case for the modified equations of the ABH model. The

lift and drag coefficients are evaluated considering the ABH formulation with and without the proposed corrections, developed in subsection 5.1.1. The results are also compared to the CFD data available for this case study. The results for Mach 0.6 and Mach 0.8 are reported in Figure 5.17 and Figure 5.18. The modified ABH model is quite precise in evaluating the lift coefficient trend as a function of the angle of attack. However, it must be highlighted that the same C_{L_0} of the Mach 8 vehicle is considered here: since the Mach 5 configuration is directly derived from the Mach 8 one, it is not unexpected that a similar value for the lift coefficient at zero angle of attack is found also in that case. Moreover, the model proves its ability to estimate the slope of the lift curve quite accurately, without any modification needed to the original formulation. The drag coefficient is also computed and compared to the CFD data available. The comparison shows that the C_D is now underestimated with respect to the one obtained with the higher fidelity data. However, the overall trend shows a good accuracy between the two datasets. Similar results are also found for Mach 0.95, as shown in Figure 5.19. Quite the opposite at Mach 1.2, the C_D appears to be overestimated with respect to the CFD data. However, it should be mentioned that the accuracy of the ABH model is reduced in the transonic regime, since there are no specific formulations to compute the aerodynamic coefficient in this speed regime, and a linear interpolation is used. The estimation of both lift and drag coefficient becomes more accurate at higher Mach numbers, such as at Mach 2, as can be seen in Figure 5.21. Similar considerations can be made for the results at the cruise Mach number, which are reported in Figure 5.22.

Subsonic regime

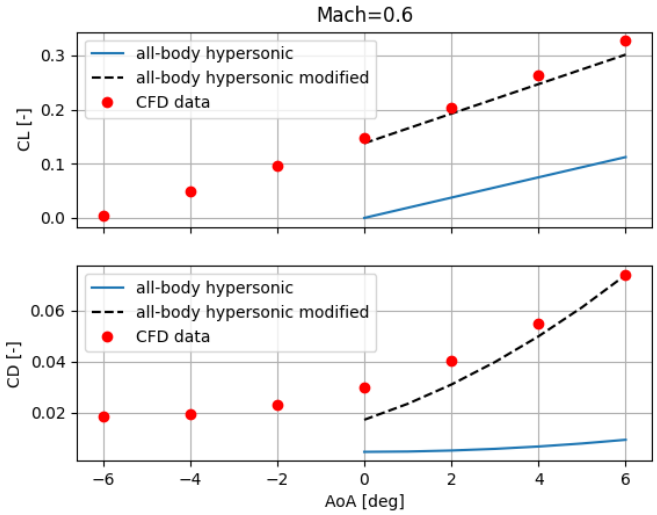

Fig. 5.17 Comparison of C_L and C_D evaluated with ABH model, modified version of ABH model and CFD analysis at Mach 0.6

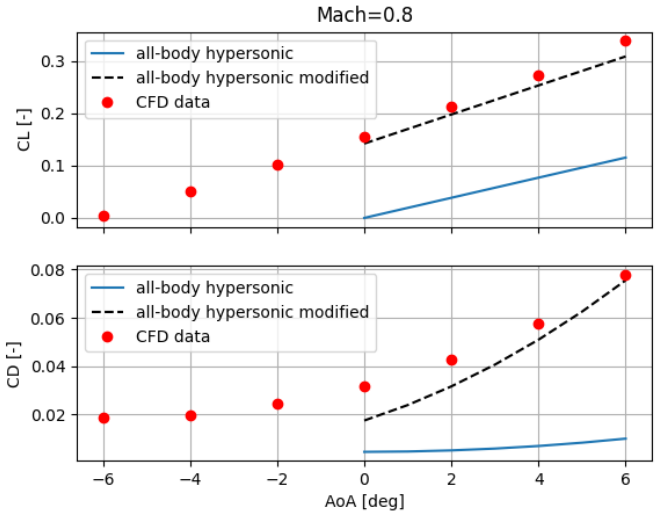

Fig. 5.18 Comparison of C_L and C_D evaluated with ABH model, modified version of ABH model and CFD analysis at Mach 0.8

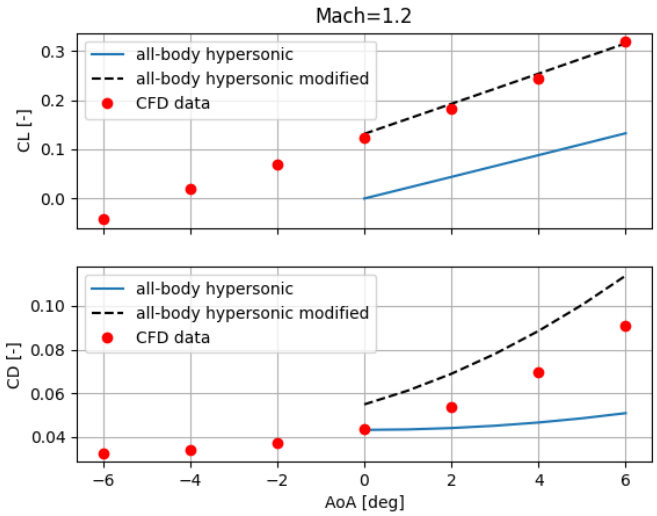

Fig. 5.20 Comparison of C_L and C_D evaluated with ABH model, modified version of ABH model and CFD analysis at Mach 1.2

Transonic regime

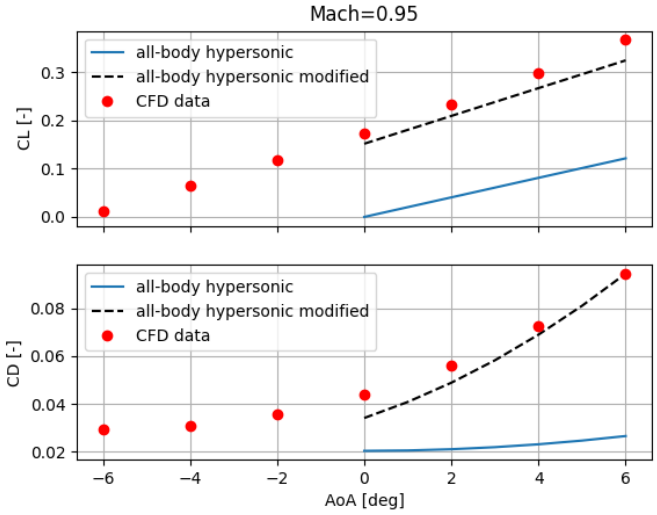

Fig. 5.19 Comparison of C_L and C_D evaluated with ABH model, modified version of ABH model and CFD analysis at Mach 0.95

Supersonic regime

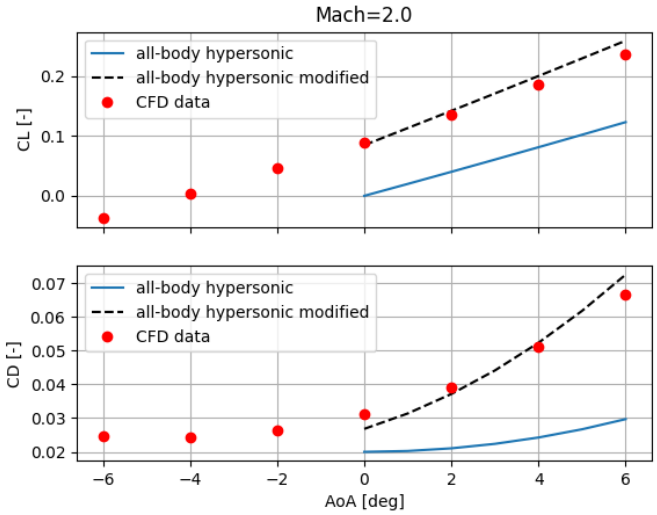

Fig. 5.21 Comparison of C_L and C_D evaluated with ABH model, modified version of ABH model and CFD analysis at Mach 2

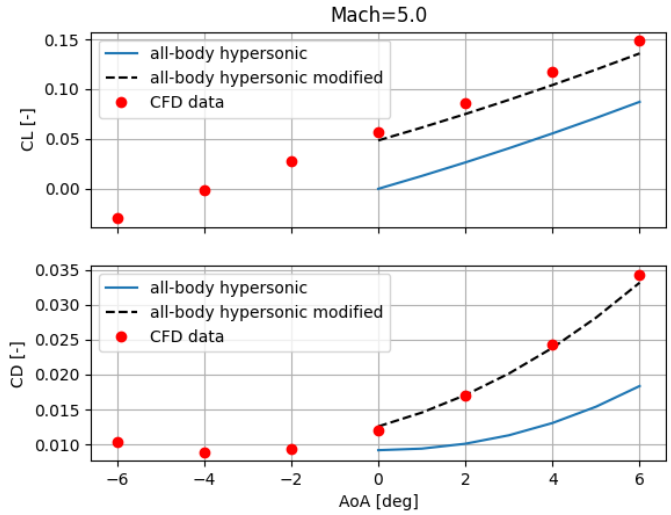

Fig. 5.22 Comparison of C_L and C_D evaluated with ABH model, modified version of ABH model and CFD analysis at Mach 5

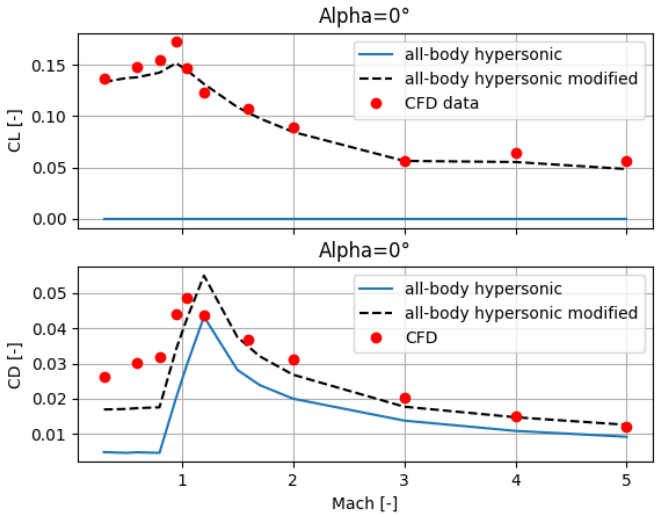

Fig. 5.23 Comparison of C_L and C_D evaluated with ABH model and CFD analysis at $\alpha = 0°$

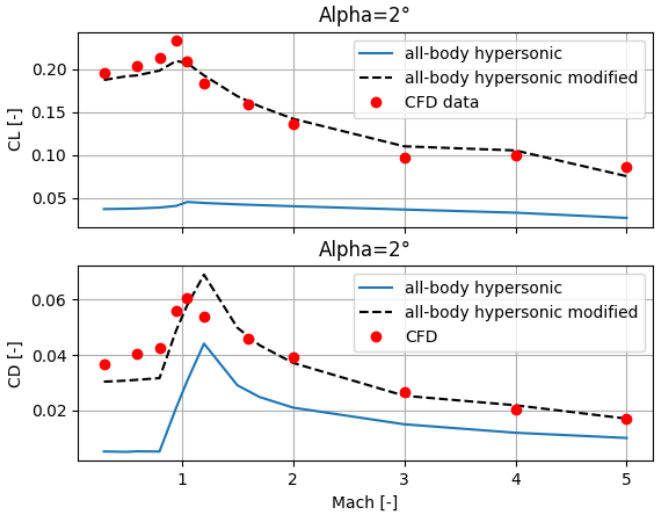

Fig. 5.24 Comparison of C_L and C_D evaluated with ABH model and CFD analysis at $\alpha = 1°$

Lift and drag coefficients are also reported as a function of Mach number for $\alpha = 0°$ and $\alpha = 2°$ in Figure 5.23 and Figure 5.24. The plots clearly show that the trend of the lift coefficient evaluated with the modified ABH model is very similar to the one obtained through CFD analysis, except for the transonic regime. Similarly, the drag coefficient is also evaluated accurately, at least for higher Mach numbers. Quite the opposite, at subsonic Mach numbers the ABH model underestimates the

C_D. A complete overview of the difference between the data computed with the ABH formulation and CFD data is reported in Table 5.2, for both the original ABH model and the modified ABH model. It can be seen that the proposed modifications are useful to improve the aerodynamic characterization of the selected configuration. At subsonic speed the difference between the estimated C_D and the one evaluated with CFD analysis decreases from 84-88% to 26-45%, depending on the Mach number and α considered. Quite the opposite, at Mach 1.2 the error increases if the modified formulations are used. However, the model is not able to capture the behaviour of the vehicle at Mach numbers around 1, and interpolations between the subsonic and supersonic regime are used to compute the coefficients. This means that the evaluation is directly influenced by the corrections applied to both the subsonic and supersonic regimes. Moreover, these modifications are required for higher Mach numbers, such as at Mach 5, where the error decreases from 24-40% to values below 4%.

Table 5.2 Summary of computed errors in estimating the C_D for the original and modified ABH model with respect to CFD data of the MR5 vehicle

	$\alpha = 0°$		$\alpha = 2°$	
Mach	ABH [%]	ABH modified [%]	ABH [%]	ABH modified [%]
0.5	84	42	87	23
0.7	85	45	88	26
0.95	54	22	62	13
1.2	1	25	18	27
2.0	36	14	46	5
5.0	24	4	40	1

5.1.3 Preliminary vs high-fidelity aerodynamic: impact on mission simulation

Eventually, it is worth estimating which is the impact of the different aerodynamic datasets on the performance of the vehicle along the reference trajectory. Two different mission simulations are considered, exploiting first the aerodynamic data obtained with the corrected preliminary model and, then, the data from CFD analysis. The resulting altitude profile is reported in Figure 5.25, while the Mach profiles are shown in Figure 5.26. The resulting profiles are almost overlapped, and only the

cruise altitude of the CFD case is slightly higher than the one of the preliminary estimations. A significant discrepancy can be observed in the variation of propellant mass when high-fidelity data is taken into account. The main difference is visible during the climb phase, due to the fact that the simplified model underestimates the total drag with respect to the CFD case. However, the fuel consumption during the cruise phase is similar, suggesting a good estimation of the aerodynamic performance in this phase. The resulting aerodynamic efficiency is reported in Figure 5.28, while the angle of attack is shown in Figure 5.29. The L/D decreases considerably during the climb phase when the high-fidelity data are considered, while at Mach 5 it is lower than the first estimate value (L/D decreases from 4.9 to 4.5). This can be explained by looking at the angle of attack, which is set to -0.3°, slightly lower than in the preliminary case.

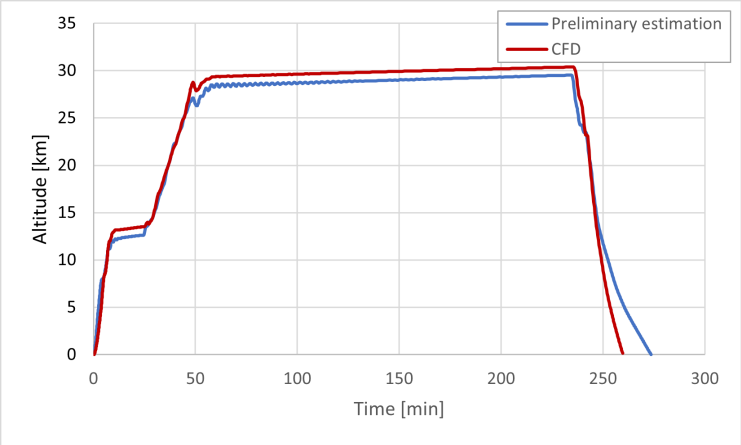

Fig. 5.25 Altitude profiles comparison betweem preliminary data and CFD data

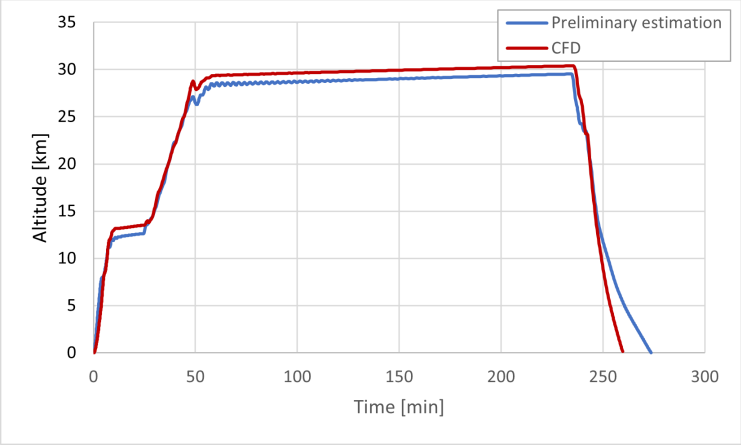

Fig. 5.26 Mach profiles comparison betweem preliminary data and CFD data

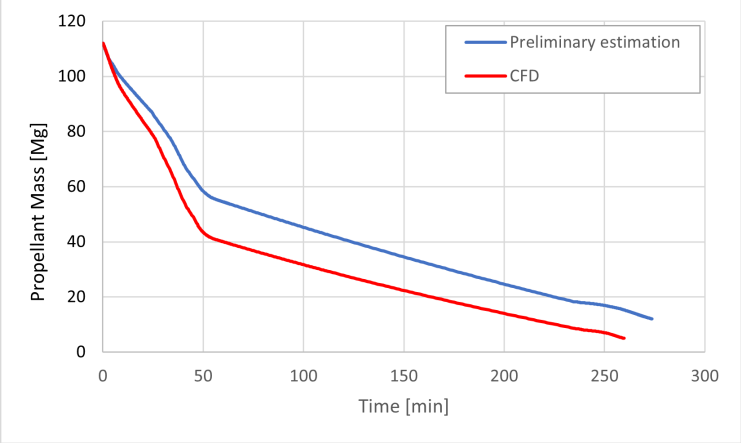

Fig. 5.27 Propellant mass trend comparison betweem preliminary data and CFD data

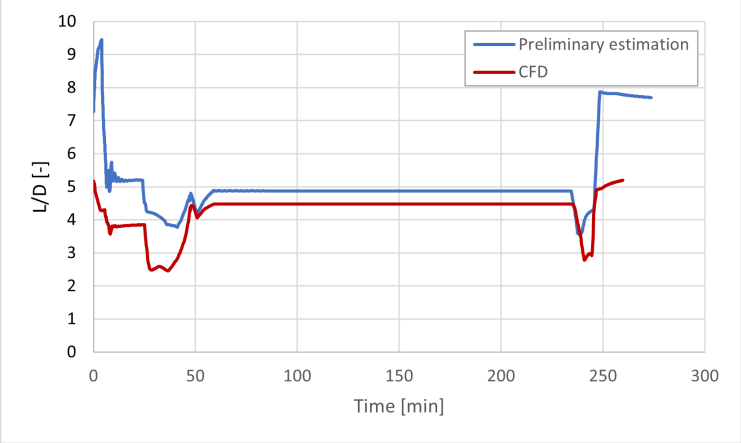

Fig. 5.28 L/D trend comparison betweem preliminary data and CFD data

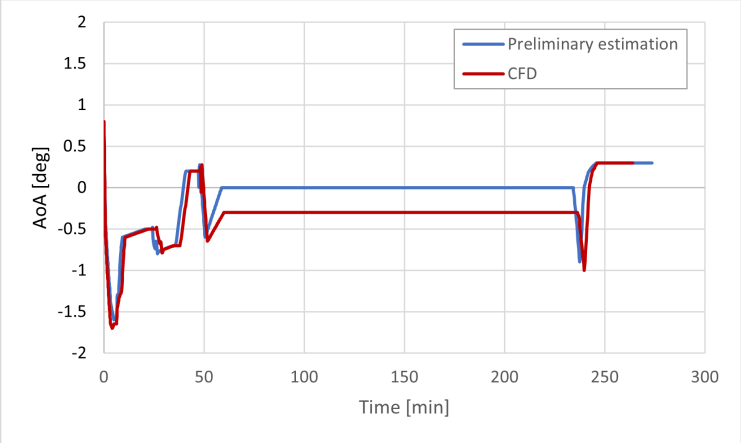

Fig. 5.29 AoA comparison betweem preliminary data and CFD data

5.1.4 Wing-body configuration preliminary aerodynamic analysis

The same procedure adopted for the waverider case studies can be used to complete the preliminary aerodynamic analysis of wing-body configurations case studies. Among the preliminary aerodynamic models presented in section 4.1, both Raymer [11] and Toreenbek [27] reference model can be suitable for this case.
A first comparison has been carried on between those two models, to analyse their accuracy in predicting the aerodynamic coefficients. Then, the drag curves have been evaluated accordingly, and compared to the results of the CFD analysis. For example, the three curves computed at Mach 2 are reported in Figure 5.30. The Raymer data approximates quite precisely the lift and drag coefficients at low angles of attack (i.e. in the range of values around $C_L = 0$). For higher α instead, the slope of the drag curve is lower than the higher fidelity one. Quite the opposite, the Torenbeek model underestimates the C_D, and the minimum drag is almost half the one evaluated with CFD analysis.

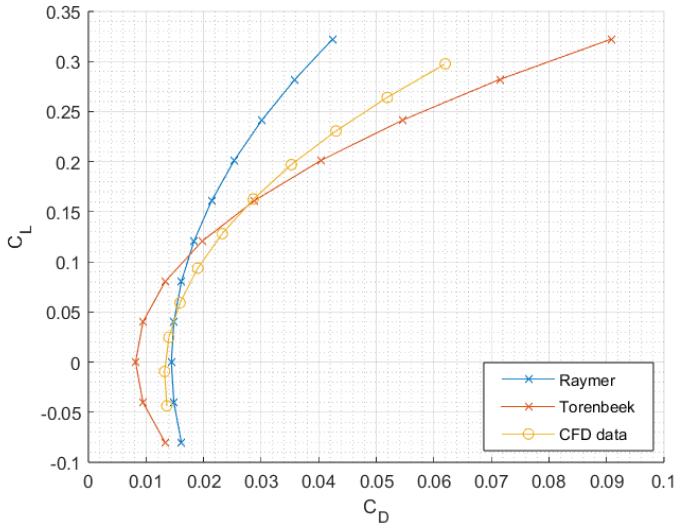

Fig. 5.30 Comparison of drag curve evaluated with Raymer model, Torenbeek model and CFD data at Mach 2

Moreover, the Torenbeek model allows for the estimation of the aerodynamic coefficient only in supersonic flight regime. For those reasons, for the purpose of this thesis, the Raymer formulations are selected as the reference model for the preliminary aerodynamic estimation. First, the Mach 2 aircraft is analysed. The aerodynamic lift and drag coefficients are evaluated by exploiting the Raymer model for the entire Mach range and angles of attack between $-5°$ and $11°$. Figure 5.31 and Figure 5.32 show the lift and drag coefficients evaluated with the Raymer model (blue line) and compared to the actual CFD results (red points), for Mach 0.3 and 0.6, respectively. The slope of the lift coefficient curve is lower than the one evaluated with higher fidelity data. The computed slope is $\sim$58% lower for both Mach numbers. This behaviour can be explained considering that the Mach 2 aircraft is equipped with an ogival delta wing derived from the one of the Concorde, which leads to higher aspect ratios and greater aerodynamic efficiency at low speed, with respect to other wing type. For the evaluation of the lift coefficient, the Raymer model suggests a combination of both theoretical and empirical equations. In particular, the corrective factors which account for real effect on a typical wing may be too conservative for the ogival wing considered here, which could generate high lift at subsonic speeds.
Moreover, the lift coefficient at zero angle of attack cannot be evaluated, and is assumed to be zero, even if the CFD data highlight that this value is not negligible.

Furthermore, the comparison of the drag coefficient shows that the Raymer model underestimates both parasite and induced drag.

Subsonic regime

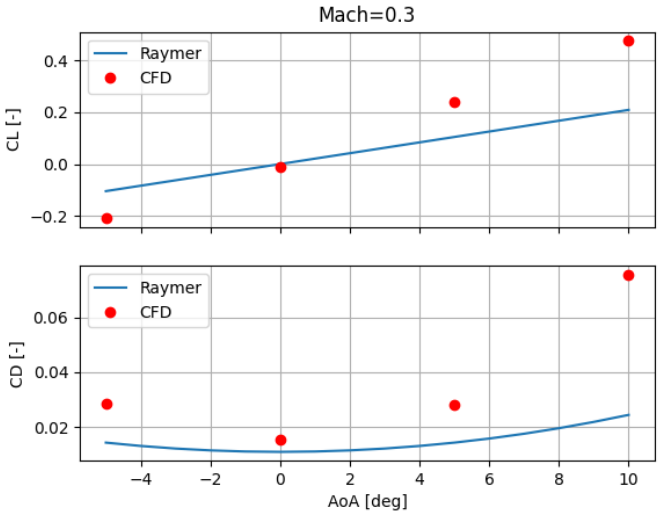

Fig. 5.31 Comparison of C_L and C_D evaluated with Raymer model and CFD analysis at Mach 0.3

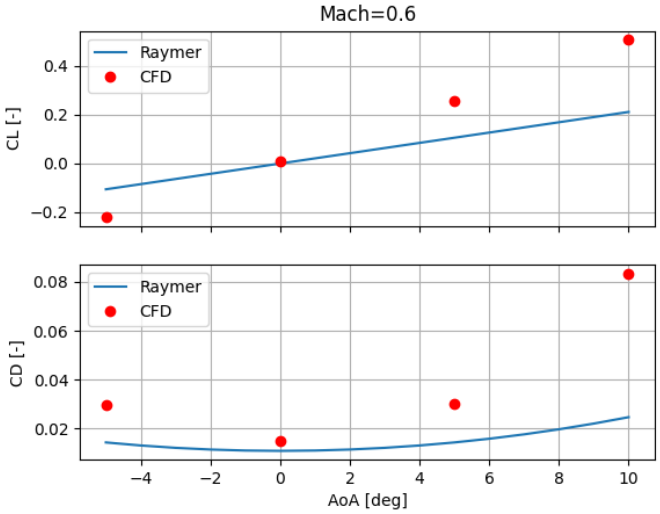

Fig. 5.32 Comparison of C_L and C_D evaluated with Raymer model and CFD analysis at Mach 0.6

The coefficients computed for Mach 0.95 and Mach 1.2 are shown in Figure 5.33 and Figure 5.34. The evaluation of the C_L is more precise at Mach 0.95, where the error decreases to 13%, while the curve slope is higher than the one of the CFD data at Mach 1.2 ($\simeq$), with an error of $\sim$55%. In the transonic regime, C_{D_0} calculated with the Raymer model is similar to the one of the CFD, while the slope of the C_D curve is lower. The coefficients for the supersonic regime are reported in Figure 5.35 and Figure 5.36 for Mach 1.6 and Mach 2. Moreover, the evaluation of the lift coefficient is more precise for high-speed velocities. It must be noted that, at cruise Mach number, the computed lift coefficient is almost juxtaposed to CFD data, with an error of $\sim$17%. The drag coefficient comparison shows that the model slightly overestimates parasite drag, while it underestimates the induced drag, as can be seen from the lower slope of the curve at increasing angles of attack. Indeed, the viscous separation strongly influences drag at angles of attack. When lift coefficients are high, the drag polar deviates from the parabolic shape typically depicted by a constant value of the coefficient k [11], which is included in the Raymer model to estimate the induced drag in Equation 4.25.

Transonic regime

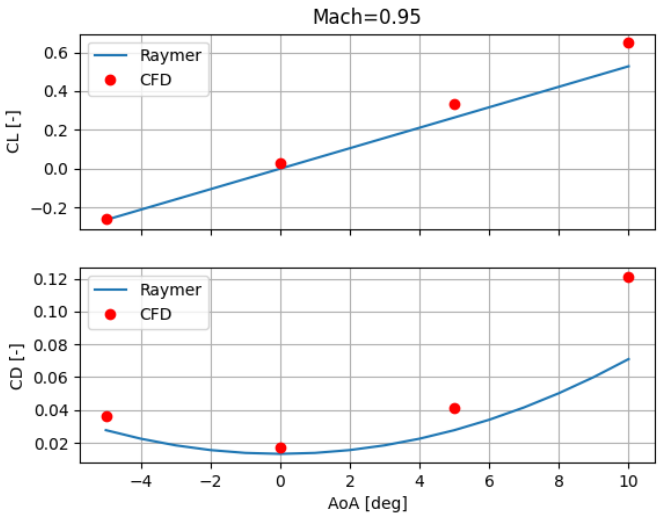

Fig. 5.33 Comparison of C_L and C_D evaluated with Raymer model and CFD analysis at Mach 0.95

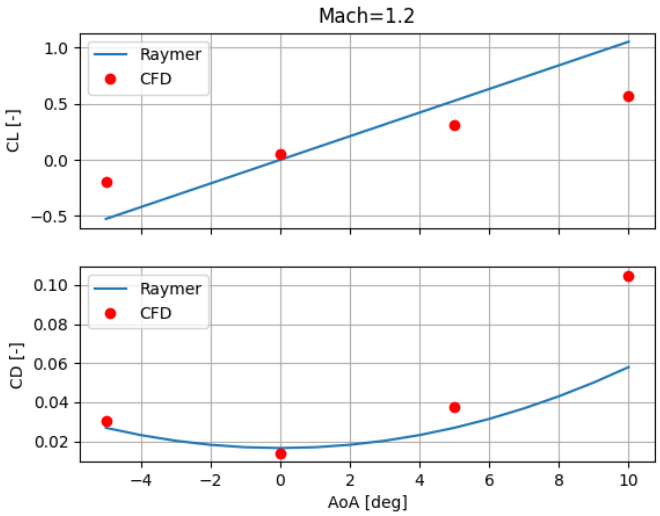

Fig. 5.34 Comparison of C_L and C_D evaluated with Raymer model and CFD analysis at Mach 1.2

Supersonic regime

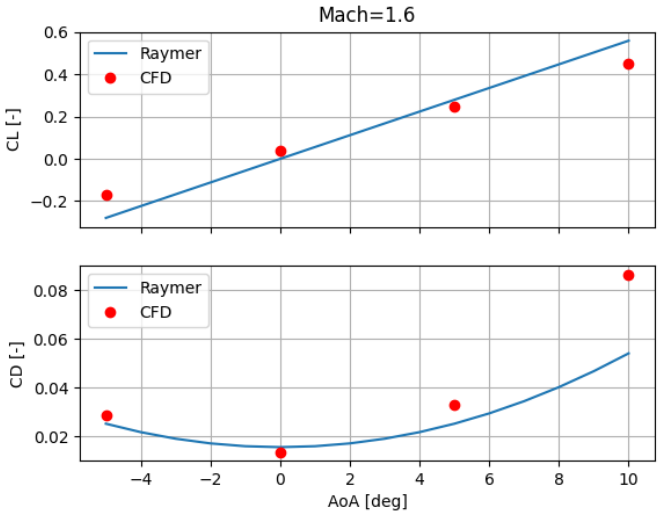

Fig. 5.35 Comparison of C_L and C_D evaluated with Raymer model and CFD analysis at Mach 1.6

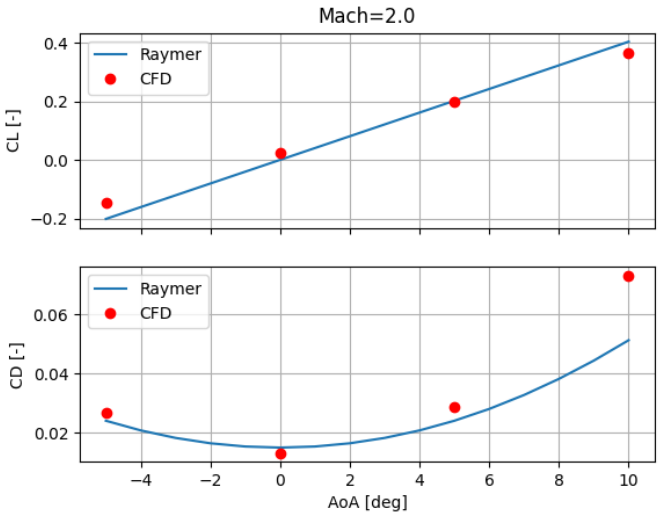

Fig. 5.36 Comparison of C_L and C_D evaluated with Raymer model and CFD analysis at Mach 2

Considering that the slope of the lift coefficient curve in the subsonic regime is lower than the reference one, Equation 4.10 has been modified to increase the computed value. A multiplicative factor of 2.25 has been chosen for a more precise estimation of C_{L_α}. The modified equation can now be written as:

$$C_{L_\alpha} = \mathbf{2.25} \cdot \left[\frac{2 \cdot \pi \cdot AR}{2 + \sqrt{4 + \left(\frac{AR \cdot \beta}{\eta}\right)^2 \left(1 + \frac{\tan^2(\Lambda)}{\beta^2}\right)}} \left(\frac{S_{exposed}}{S_{ref}}\right) F \right] \tag{5.4}$$

The comparison between the results obtained with the modified equation and the reference one is reported in Figure 5.37 and Figure 5.38, for Mach 0.3 and Mach 0.6. The new formulation results in better estimations of the C_L values at subsonic speeds, where the error decreases to $\sim 5\%$. C_D is evaluated again considering the updated values of C_L, and the results are shown in Figure 5.37 and Figure 5.38. The sole modification to C_L guarantees good estimations of the drag coefficient, especially at low angles of attack ($-5° \leq \alpha \leq 5°$). For the supersonic regime, no modifications are included to estimate the lift coefficient, since it is already considered sufficiently accurate for preliminary analysis. Quite the opposite, additional modifications are required for a better evaluation of the drag coefficient. Since the C_D at zero angle of attack is similar to the one computed through CFD analysis, the main focus is

shifted to the induced drag. In particular, the coefficient k is analysed. The following modified equation is proposed, where a multiplicative factor of 1.5 is introduced to Equation 4.25:

$$k = \mathbf{1.5} \cdot \frac{AR \cdot (M^2 - 1) \cdot cos(\Lambda_{LE})}{\left(4 \cdot AR\sqrt{M^2 - 1}\right) - 2} \tag{5.5}$$

The comparison of the aerodynamic coefficients evaluated through the Raymer model, the modified version and the CFD data is reported in Figure 5.41 and Figure 5.42.

Subsonic regime

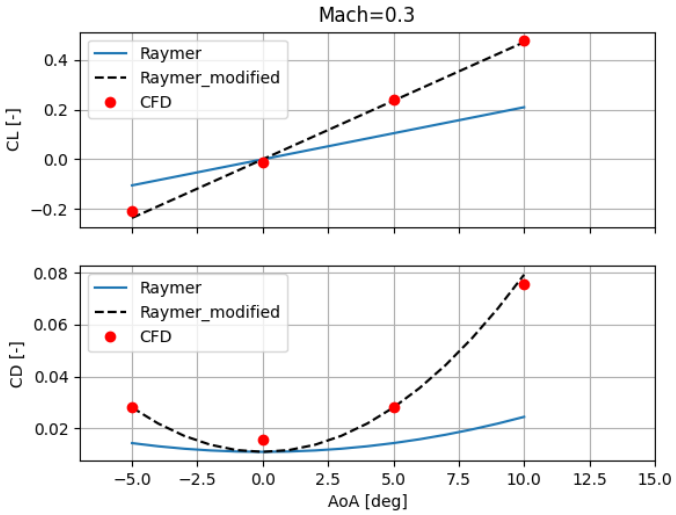

Fig. 5.37 Comparison of C_L and C_D evaluated with Raymer model, modified version of Raymer model and CFD analysis at Mach 0.3

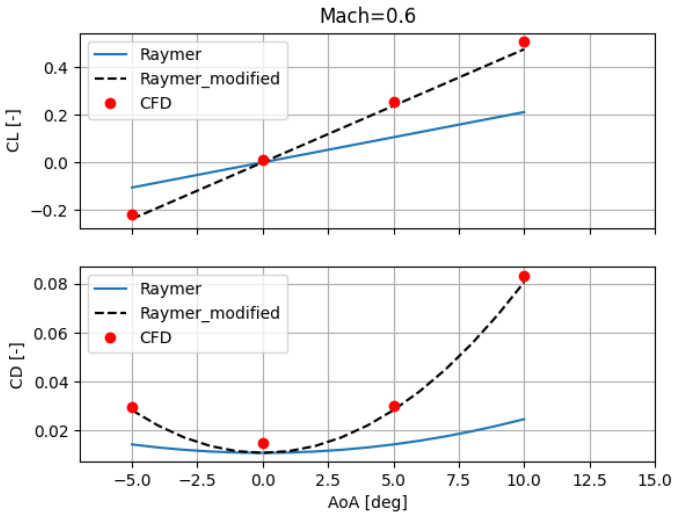

Fig. 5.38 Comparison of C_L and C_D evaluated with Raymer model, modified version of Raymer model and CFD analysis at Mach 0.6

Transonic regime

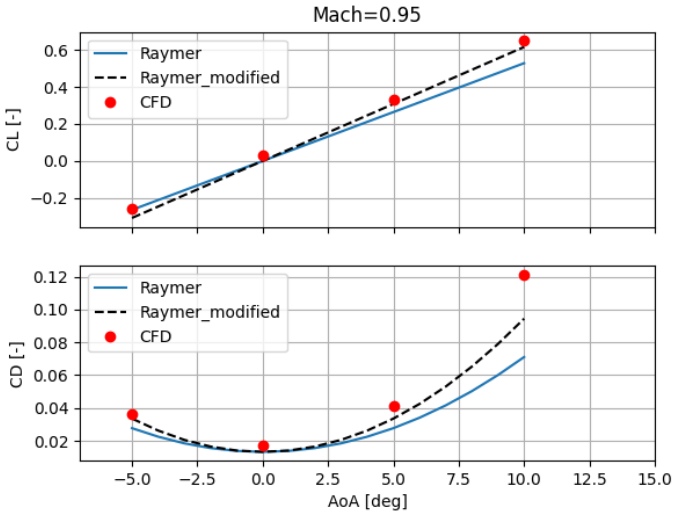

Fig. 5.39 Comparison of C_L and C_D evaluated with Raymer model, modified version of Raymer model and CFD analysis at Mach 0.95

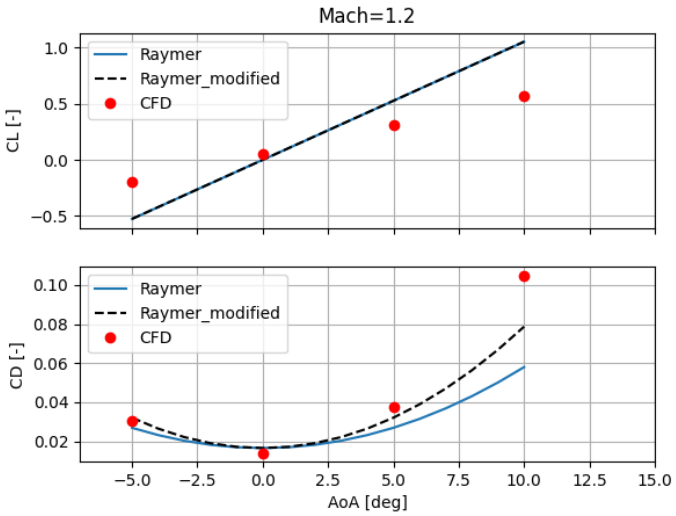

Fig. 5.40 Comparison of C_L and C_D evaluated with Raymer model, modified version of Raymer model and CFD analysis at Mach 1.2

Supersonic regime

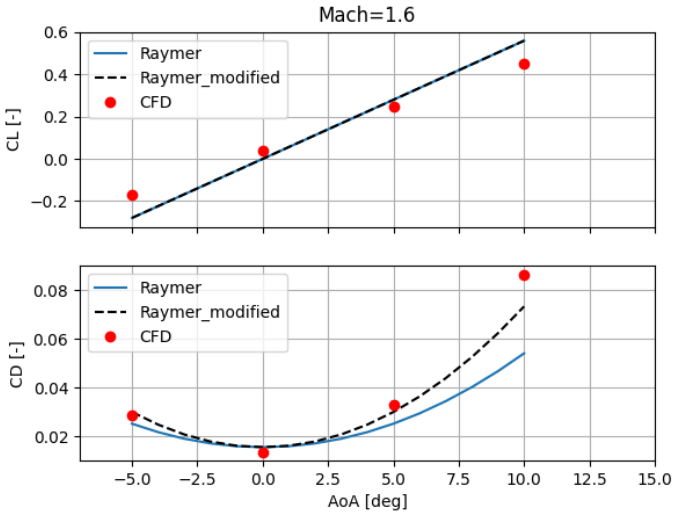

Fig. 5.41 Comparison of C_L and C_D evaluated with Raymer model, modified version of Raymer model and CFD analysis at Mach 1.6

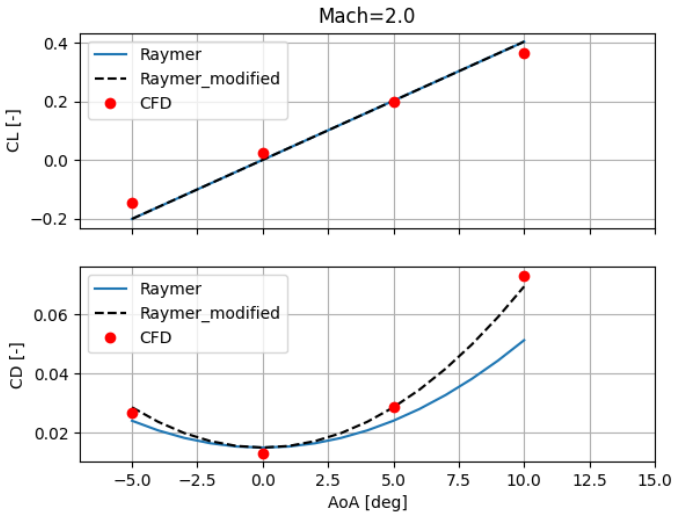

Fig. 5.42 Comparison of C_L and C_D evaluated with Raymer model, modified version of Raymer model and CFD analysis at Mach 2

The lift and drag coefficients are reported for different Mach numbers at AoA=5° and AoA=10° in Figure 5.43 and Figure 5.44. The modified lift curve slope in subsonic regime allows for a more precise estimation of the lift coefficient up to Mach 0.8. However, the C_L in transonic flight is overestimated, due to the fact that the model is not able to cover this flight regime properly. Eventually, the lift coefficient estimation at cruise Mach number = 2 is accurate. Similarly, the drag coefficient is calculated accurately at both subsonic and supersonic speeds, while it is largely underestimated between Mach 0.95 and 1.5.

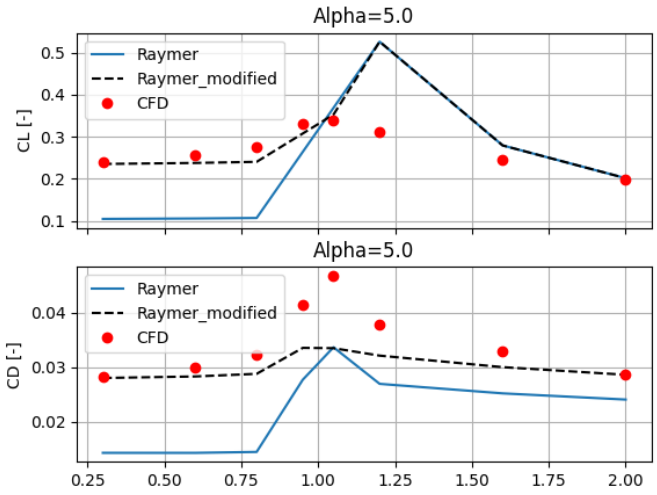

Fig. 5.43 Comparison of C_L and C_D evaluated with Raymer model, modified version of Raymer model and CFD analysis at AoA=5°

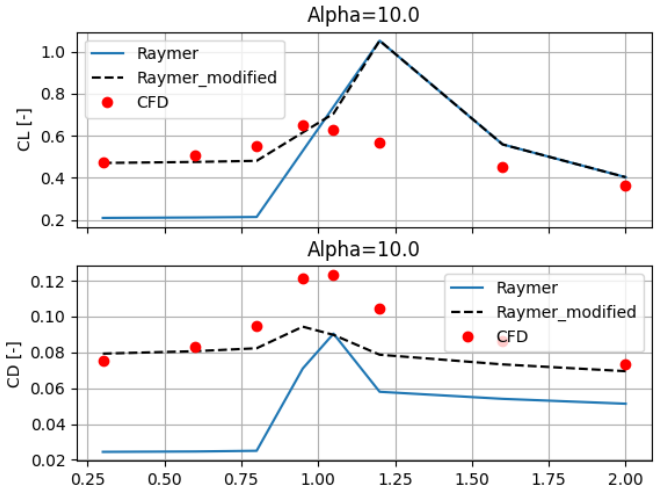

Fig. 5.44 Comparison of C_L and C_D evaluated with Raymer model, modified version of Raymer model and CFD analysis at AoA=10°

5.1.5 Wing-body configuration preliminary aerodynamic analysis: validation with Mach 1.5 configuration

The modified Raymer model is validated using an additional case study of a Mach 1.5 business jet. The lift and drag coefficients are evaluated considering the Raymer formulation with and without the proposed corrections, developed in subsection 5.1.4, and then compared to the CFD data available. The results for Mach 0.3 and Mach 0.6 are reported in Figure 5.45 and Figure 5.46. The proposed modifications are useful to better estimate the lift coefficient slope, which is otherwise underestimated. The error between low-fidelity and high-fidelity data decreases from $\sim 60\%$ to $\sim 18\%$. The evaluation of the induced drag is also improved due to the more precise estimation of the C_L. Indeed, the parasite drag is underestimated, i.e. the drag at zero angle of attack is lower. A similar trend is also found at Mach 0.95, as can be seen in Figure 5.47. At Mach=1.2 (Figure 5.48), instead, the C_D appears to be overestimated at AoA=0°, while the induced drag is lower than the CFD data. At cruise speed equal to Mach 1.5, C_L is similar to the one resulting from CFD, while C_D is overestimated at low angles of attack, as shown in Figure 5.49.

The previous results show that the modified Raymer equations are not sufficient to characterize the aircraft's aerodynamic performance at all Mach numbers with high precision, even if accuracy is increased with respect to the unmodified formulation. However, it should be highlighted that the Mach 1.5 business jet configuration is a very different configuration if compared to the Mach 2 large aircraft considered in subsection 5.1.4, which results in different aerodynamic characteristics. For that reason, these results can be still considered as a good first guess for the preliminary aerodynamic estimation. As a next step, the application of the modified formulations to another type of supersonic aircraft would be useful to further verify the ability of the proposed model to preliminarily assess the aerodynamic performance during conceptual design.

Subsonic regime

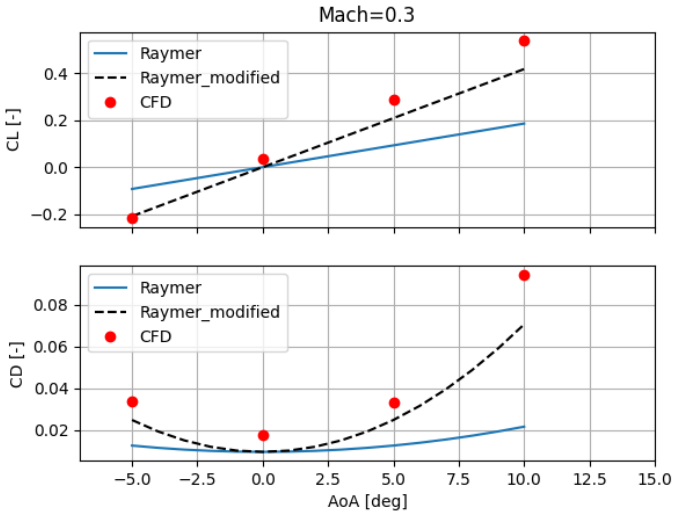

Fig. 5.45 Comparison of C_L and C_D evaluated with Raymer model, modified version of Raymer model and CFD analysis at Mach 0.3

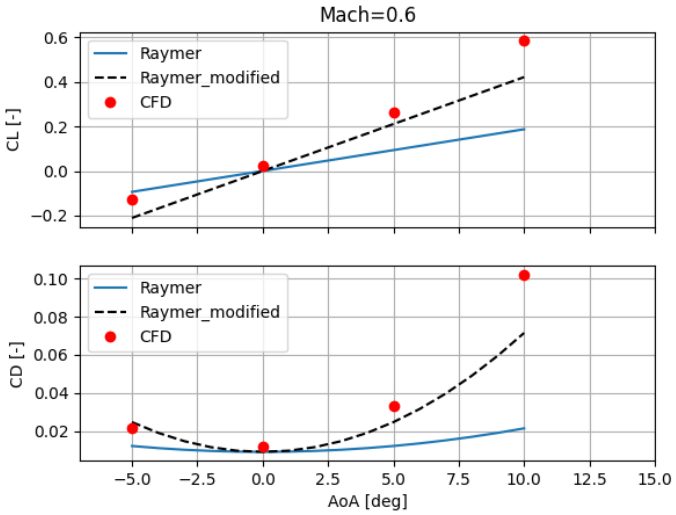

Fig. 5.46 Comparison of C_L and C_D evaluated with Raymer model, modified version of Raymer model and CFD analysis at Mach 0.6

Transonic regime

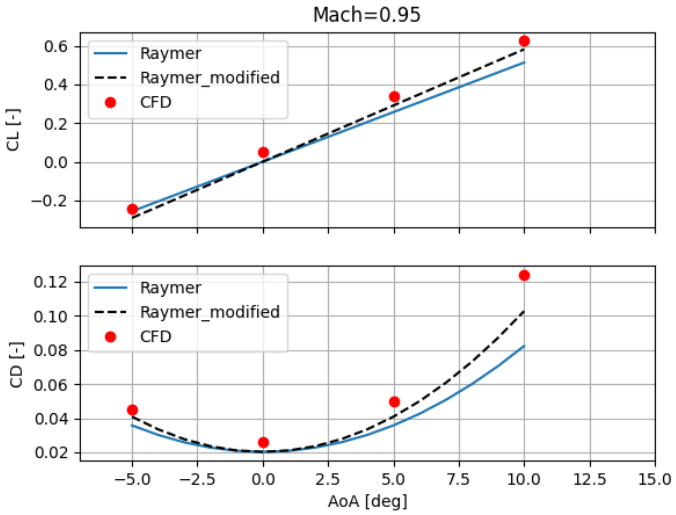

Fig. 5.47 Comparison of C_L and C_D evaluated with Raymer model, modified version of Raymer model and CFD analysis at Mach 0.95

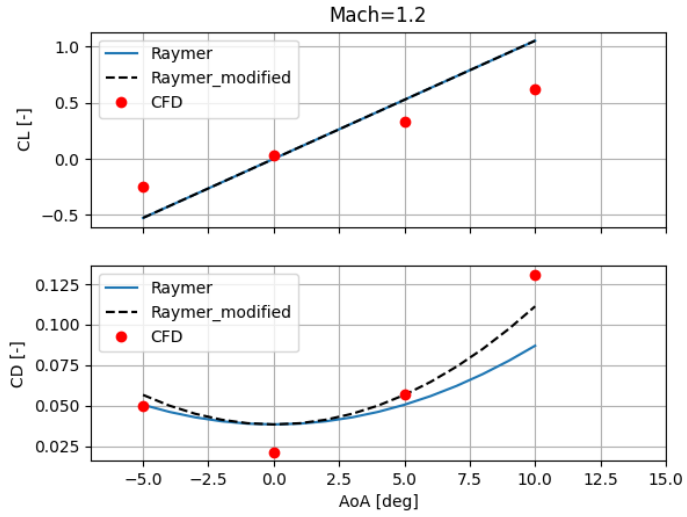

Fig. 5.48 Comparison of C_L and C_D evaluated with Raymer model, modified version of Raymer model and CFD analysis at Mach 1.2

Supersonic regime

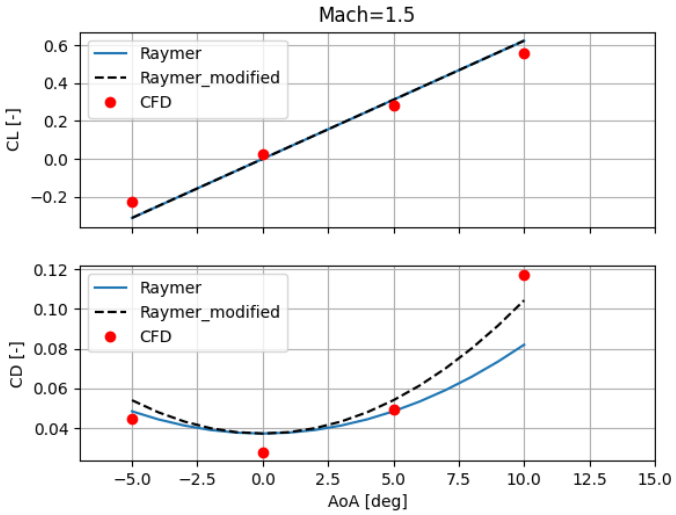

Fig. 5.49 Comparison of C_L and C_D evaluated with Raymer model, modified version of Raymer model and CFD analysis at Mach 1.5

5.2 Stability and trim analysis: STRATOFLY MR3 vehicle case study

The Flight Control System (FCS) is recognized as a key enabler for future high-speed aircraft and, therefore, the preliminary evaluation of its impact on aircraft layout and performance is fundamental to assess the viability of concepts under development. Previous studies [71, 94, 2, 95] have demonstrated that the aerodynamic efficiency can decrease up to 30% with respect to the maximum theoretical value for a high-speed aircraft, due to control surfaces deflections. The required control surfaces deflections are evaluated by checking the stability and trimmability of the aircraft along the entire Mach range.

The results of the STRATOFLY MR3 vehicle are presented here, as a baseline to illustrate the work carried on during the research activity. First, the longitudinal static stability is verified imposing that the slope of the pitching moment coefficient C_{M_y} as a function of α is negative. For the specific case study of a Mach 8 waverider, the total pitching moment is given by the sum of three different effects: clean configuration, the individual effect of the control surfaces, and the additional moment generated

due to misalignment of the thrust vector with respect to the longitudinal vehicle axis, as reported in Equation 4.37. The position of the centre of gravity x_{CoG} is expected to vary between 48 m and 53 m, while the vehicle's total length is equal to 94 m. The first position refers to the conditions in which the fuel tanks are empty, while the second one is referred to the condition in which the vehicle's total mass is equal to the MTOM. The pitching moment coefficient is evaluated for both those positions, at different Mach numbers. First, the static stability of the vehicle's clean configuration is analysed, without considering the deflections of the flight control surfaces. The results show an unstable behaviour at low speeds ($0.3 \leq M \leq 0.8$) for the most rearward position of the CoG, while at Mach 0.95 the slope of the pitching moment coefficient is negative (Figure 5.50). Figure 5.51 shows that, at higher Mach numbers ($M > 2$), the vehicle's stability is verified. Moreover, if the most forward position of the CoG is considered, the vehicle is stable for all Mach numbers (Figure 5.52 and Figure 5.53). However, the values of the C_{M_y} are always below zero, suggesting that there are no trim conditions in the range of angles of attack considered ($-6° \leq \alpha \leq 6°$). Therefore, it is clear that flight control surfaces should be introduced to guarantee stable and trimmed conditions at each Mach number and for the required α.

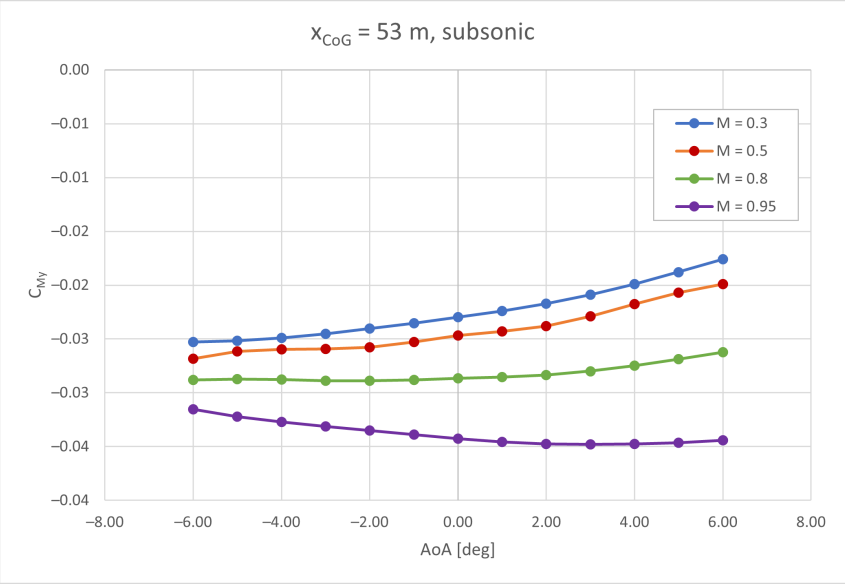

Fig. 5.50 C_{M_y} vs α at subsonic Mach number, $x_{CoG} = 53$m

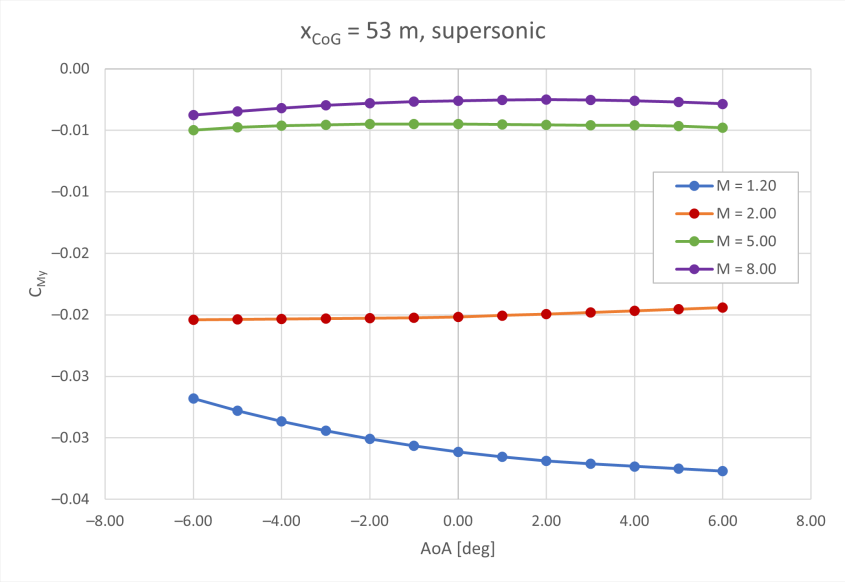

Fig. 5.51 C_{M_y} vs α at supersonic Mach number, $x_{CoG} = 53$m

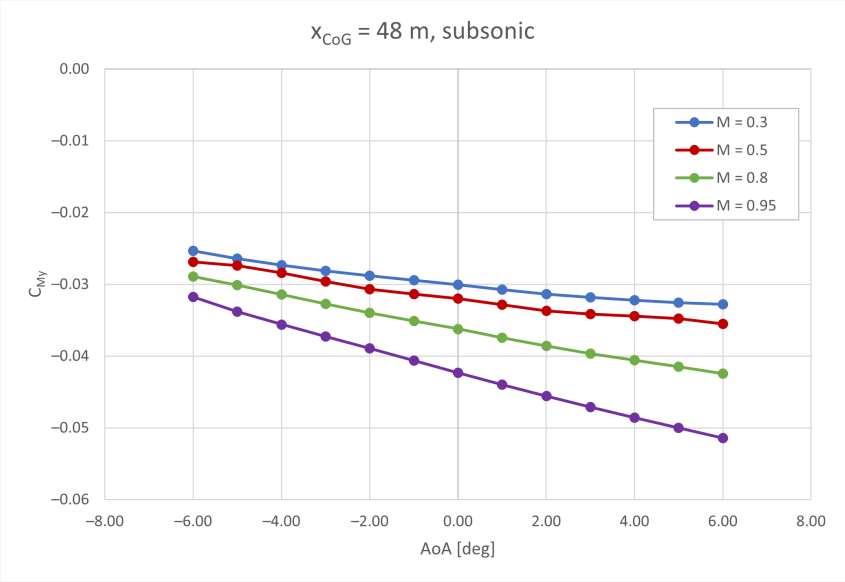

Fig. 5.52 C_{M_y} vs α at subsonic Mach number, $x_{CoG} = 48$m

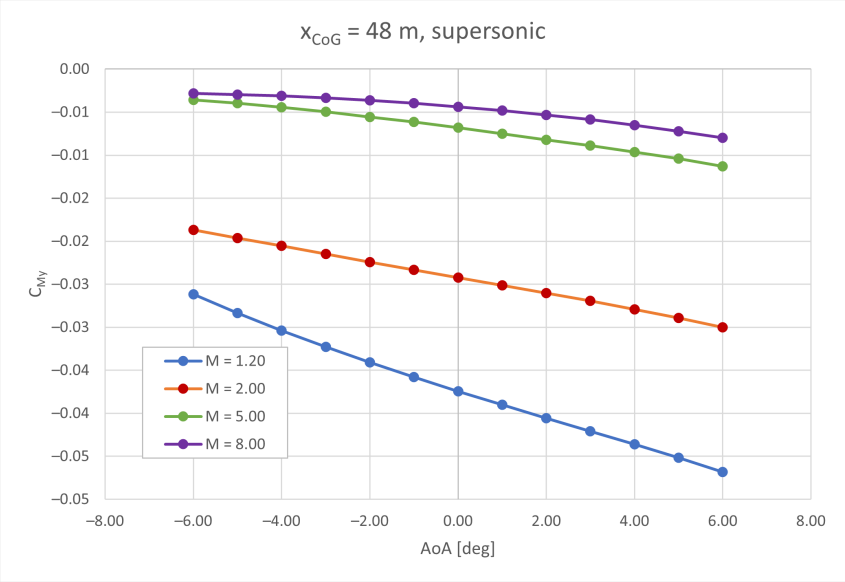

Fig. 5.53 C_{M_y} vs α at supersonic Mach number, $x_{CoG} = 48$m

Once the configuration of the flight control surfaces is defined, attention should shift towards the determination of the most favourable surfaces deflections to ensure trim conditions are maintained throughout the mission, minimizing the negative effect on the overall aerodynamic efficiency of the vehicle. Equation 4.37 can be expanded, imposing that $C_{M_y} = 0$ and including the following terms:

$$C_{M_y} = C_{M_{y\ clean}} + C_{M_{y\ flap}} + C_{M_{y\ canard}} + C_{M_{y\ bodyflap}} + C_{M_{y\ thrust}} = 0 \tag{5.6}$$

For a given Mach number, the pitching moment coefficient varies depending on x_{CoG}, which is expected to shift during the mission. For the purpose of this study, x_{CoG} varies between 51% (48m, empty tanks) and 56% (53m, full tanks) of the vehicle length. The algorithm presented in Equation 4.39 is exploited to evaluate the most favourable flight control surfaces deflections which can guarantee stability and trim, given Mach number and x_{CoG}. For example, the value of the minimum deflection is evaluated for the STRATOFLY MR3 vehicle. The required deflections are lower as the CoG shifts forward for this case. Figure 5.54 reports the minimum required deflection needed to achieve stability and trim for different Mach numbers and positions of the CoG. As mentioned previously, the required deflections decrease when the position of the CoG shifts from 53 m to 48 m. It is also interesting to highlight that the transonic/low supersonic flight regime is the most demanding in

terms of required deflections, even if x_{CoG} approaches its minimum value. This has a significant impact on the aerodynamic efficiency in that Mach range.

		CoG position [m]										
		53	52.5	52	51.5	51	50.5	50	49.5	49	48.5	48
Mach	0.3	-30	-25	-25	-25	-25	-25	-20	-20	-20	-10	0
	0.5	-30	-25	-25	-25	-25	-20	-20	-20	-10	0	0
	0.7	-25	-25	-25	-20	-20	-20	-10	0	0	0	0
	0.8	-25	-25	-25	-20	-20	0	0	0	0	0	0
	0.95	-20	-20	-20	-15	0	0	0	0	0	0	0
	1.05	-25	-20	-20	0	0	0	0	0	0	0	0
	1.2	-25	-20	-20	0	0	0	0	0	0	0	0
	1.5	-25	-25	-20	-20	-20	0	0	0	0	-10	-10
	1.7	-25	-25	-25	-20	-20	-20	-15	-10	-10	-10	-10
	2	-25	-25	-25	-20	-20	-20	-20	-15	-10	-10	-10
	3	-25	-25	-25	-25	-25	-25	-20	-20	-20	-20	-15
	4	-25	-25	-25	-20	-20	-20	-15	-15	-10	0	0
	5	-25	-25	-25	-20	-20	-20	-15	0	0	0	0
	6	-25	-25	-20	-20	-20	-20	-15	-15	0	0	0
	7	-25	-25	-20	-20	-20	-20	-15	0	0	0	0
	8	-25	-25	-20	-20	-20	-20	-15	-15	-15	-10	0

Fig. 5.54 Minimum bodyflap deflections to achieve stability and trim

The previous results are exploited to define an ad-hoc propellant depletion strategy to minimize surfaces deflections [96]. The outcome of the selected propellant depletion sequence is reported in Figure 5.55, where the position of the CoG at each Mach number is shown.

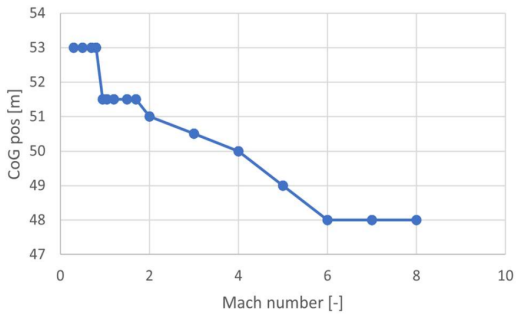

Fig. 5.55 Position of the CoG at different Mach numbers

The main outcome of the trim analysis is a set of trim maps at each Mach number and x_{CoG}, where the angle of attack which guarantees trimmability α_{trim} is reported for different control surfaces deflections. For example, the 3D trim map for Mach 0.5 and $x_{CoG} = 53$m is reported in Figure 5.56, while the 2D trim map is shown in Figure 5.57, for a fixed deflection of the bodyflap ($\delta_{bodyflap} = -25°$). The trim maps for Mach 0.8 are reported in Figure 5.58 and Figure 5.59. The deflections required to trim the vehicle in the subsonic regime are greater than $\pm 10°$, which results in high trim drag. This is the most demanding flight regime, due to the unfavourable

position of the CoG, which is placed towards the rear of the aircraft at low Mach numbers.

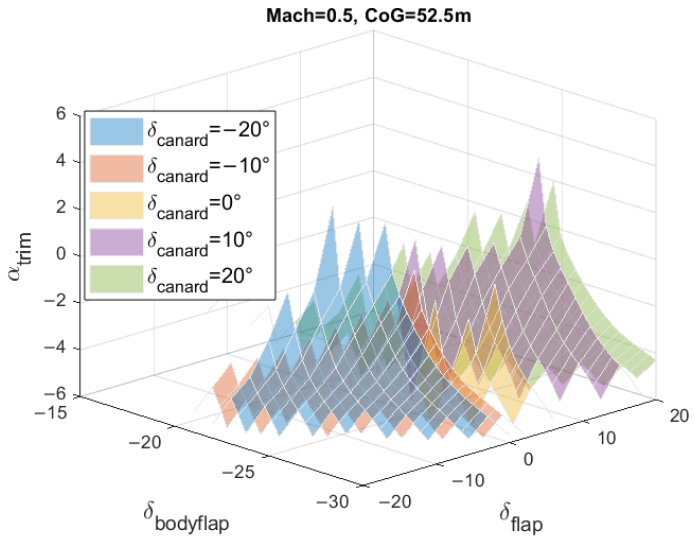

Fig. 5.56 3D trim map at Mach 0.5 and $x_{CoG} = 52.5$m

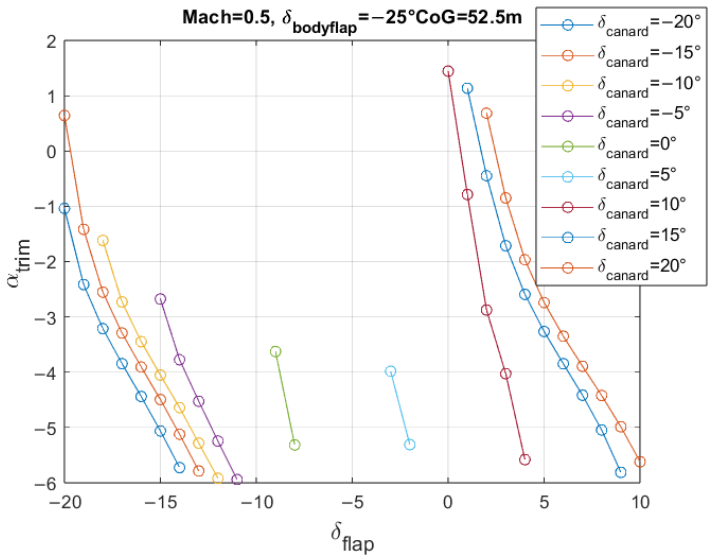

Fig. 5.57 2D trim map at Mach 0.5, $x_{CoG} = 52.5$m and $\delta_{bodyflap} = -25°$

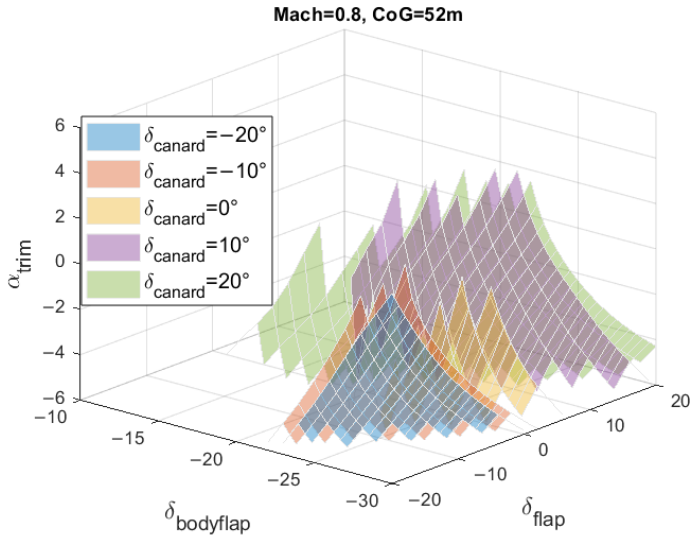

Fig. 5.58 3D trim map at Mach 0.8 and $x_{CoG} = 52$m

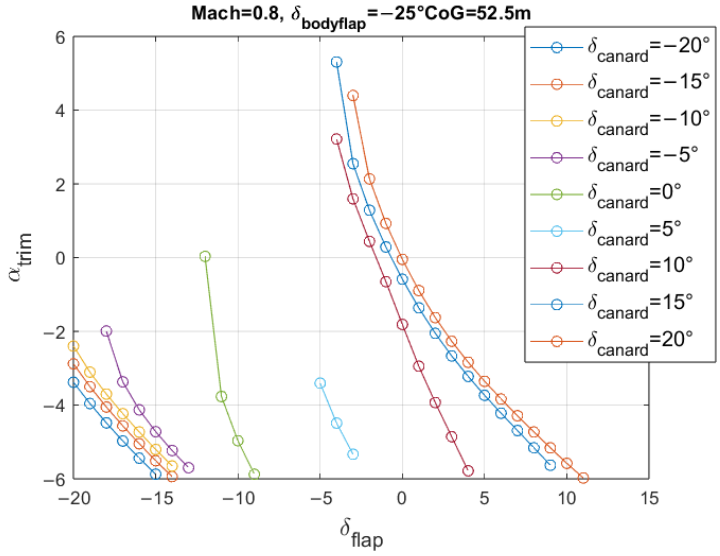

Fig. 5.59 2D trim map at Mach 0.8, $x_{CoG} = 52$m and $\delta_{bodyflap} = -25°$

Similar trim maps are also reported for Mach 1.2 in Figure 5.60 and Figure 5.61, while the results for Mach 2 are shown in Figure 5.62 and Figure 5.63. The deflections required to trim the vehicle in this flight regime are lower than in the previous case, since the position of the CoG is shifting forward, towards less demanding conditions in terms of trimmability.

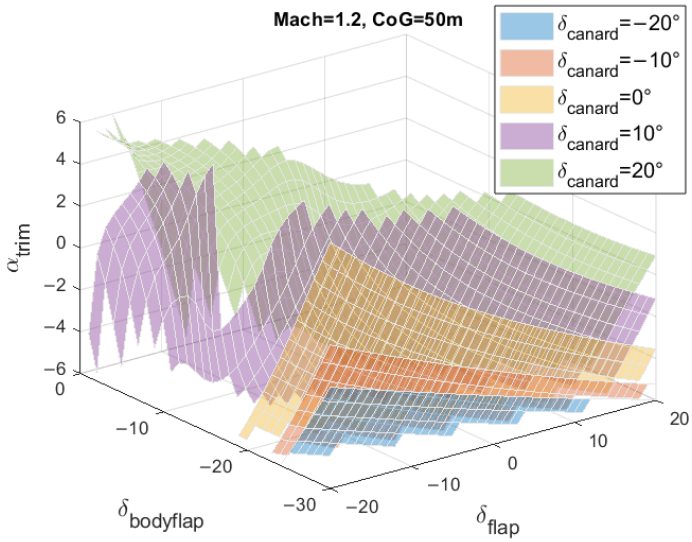

Fig. 5.60 3D trim map at Mach 1.2 and $x_{CoG} = 50$m

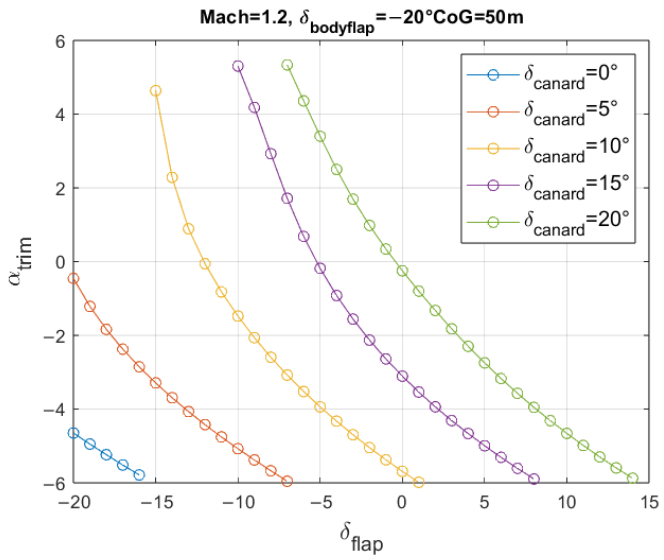

Fig. 5.61 2D trim map at Mach 1.2, $x_{CoG} = 50$m and $\delta_{bodyflap} = -20°$

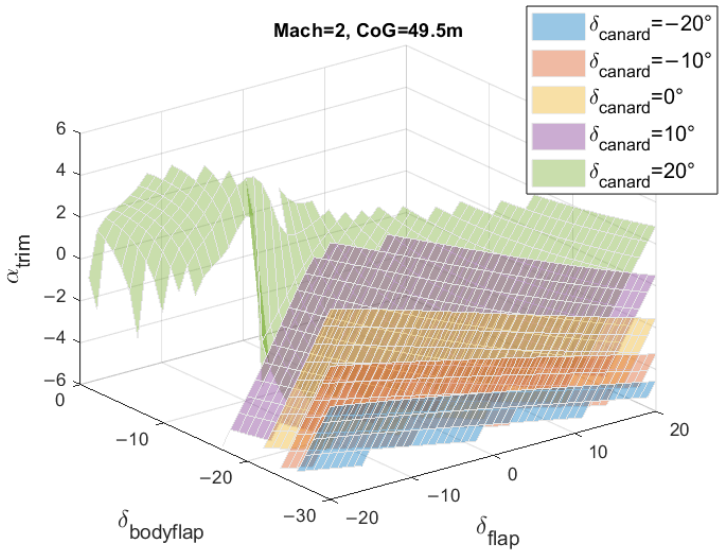

Fig. 5.62 3D trim map at Mach 2 and $x_{CoG} = 49.5$m

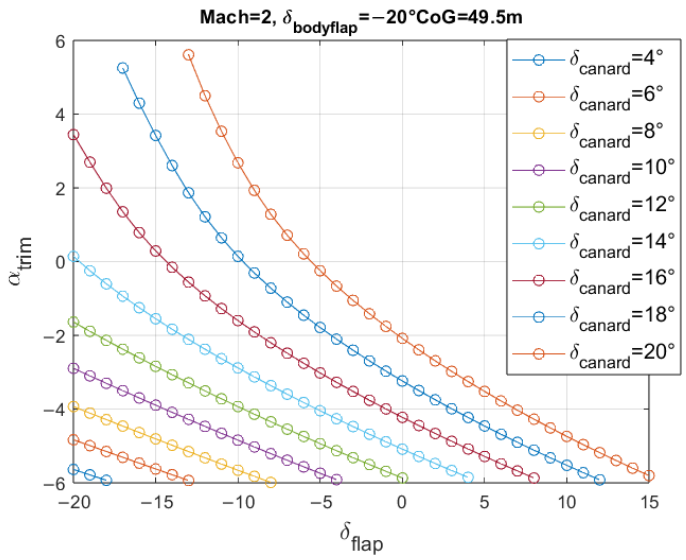

Fig. 5.63 2D trim map at Mach 2, $x_{CoG} = 49.5$m and $\delta_{bodyflap} = -20°$

Eventually, the trim maps are also computed for the hypersonic flight regime, and are reported in Figure 5.64 and Figure 5.65 for Mach 5. The values for the cruise Mach number are also evaluated and reported in Figure 5.66 and Figure 5.67.

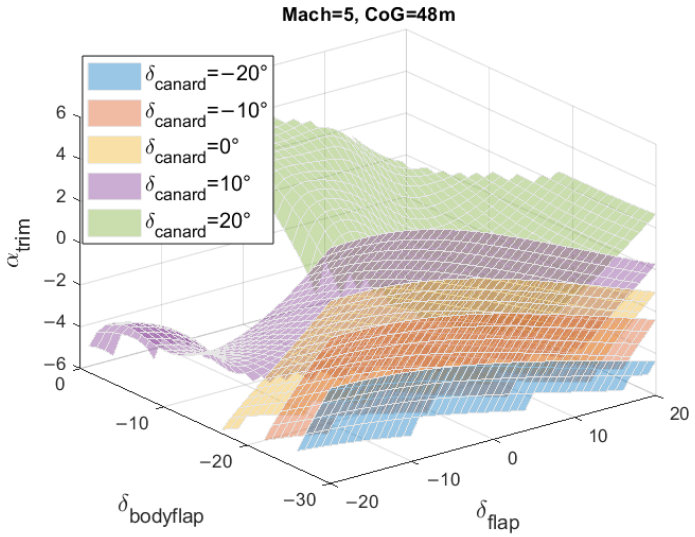

Fig. 5.64 3D trim map at Mach 5 and $x_{CoG} = 48$m

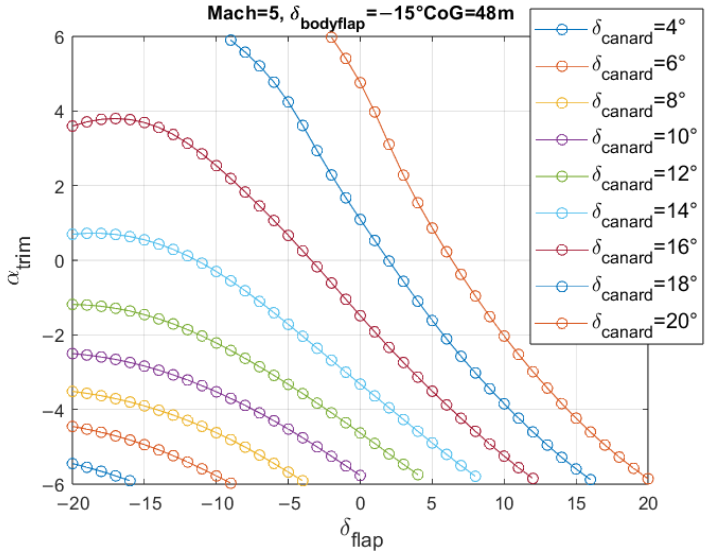

Fig. 5.65 2D trim map at Mach 5, $x_{CoG} = 48$m and $\delta_{bodyflap} = -15°$

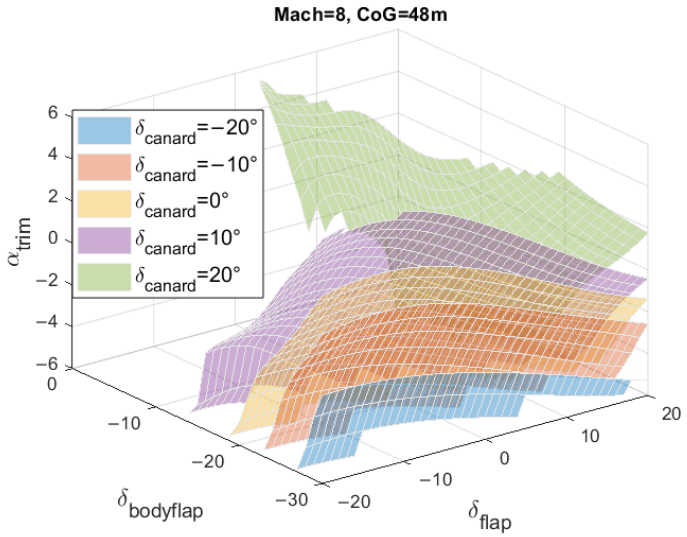

Fig. 5.66 3D trim map at Mach 8 and $x_{CoG} = 48$m

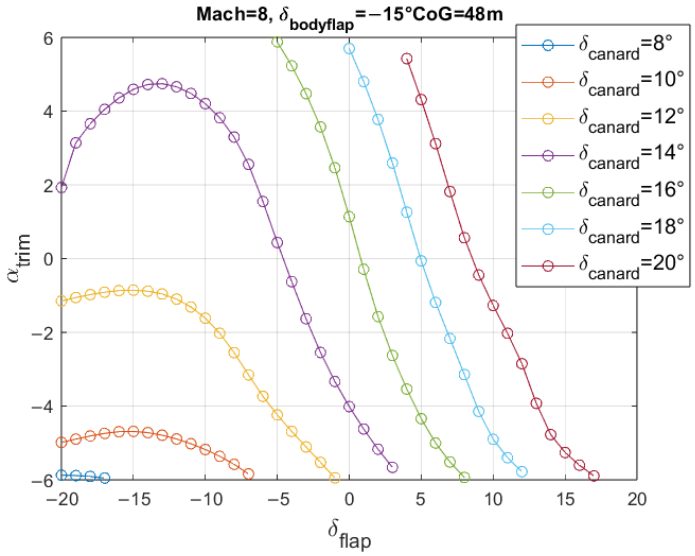

Fig. 5.67 2D trim map at Mach 8, $x_{CoG} = 48$m and $\delta_{bodyflap} = -15°$

As can be seen from the previous plots, a certain α_{trim} can be achieved through different combinations of control surface deflections. In this case, the combination which guarantees the highest aerodynamic efficiency is selected among the available options. The aerodynamic data evaluated considering both the clean configuration and the trimmed case can now be compared, to estimate the impact of the control surfaces deflections on the overall aerodynamic performance. The lift and drag

coefficients at $\alpha = 0°$ are reported in Figure 5.68 and Figure 5.69. The lift coefficient is affected by the deflections of the control surfaces especially at low speeds, where the C_L is higher. However, the major effect is seen on the C_D which is increasing significantly both in subsonic and supersonic regimes, up to Mach 4. The impact is also visible for higher Mach numbers, even if the drag increase is limited. As a consequence, the aerodynamic efficiency is also decreased along the entire Mach range, as shown in Figure 5.70.

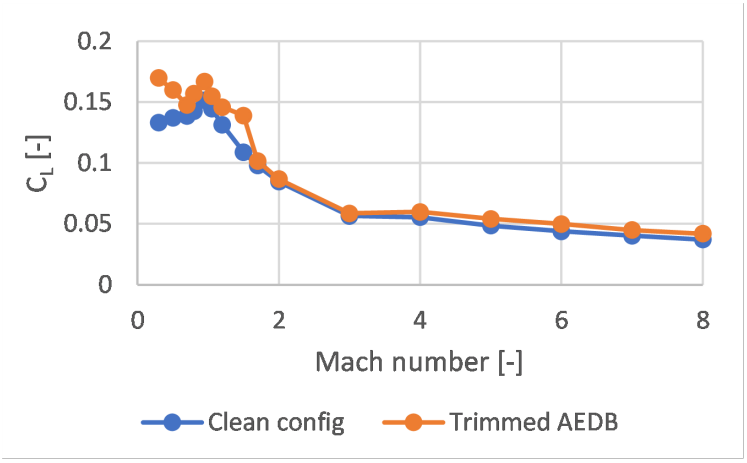

Fig. 5.68 Comparison between clean and trimmed lift coefficient

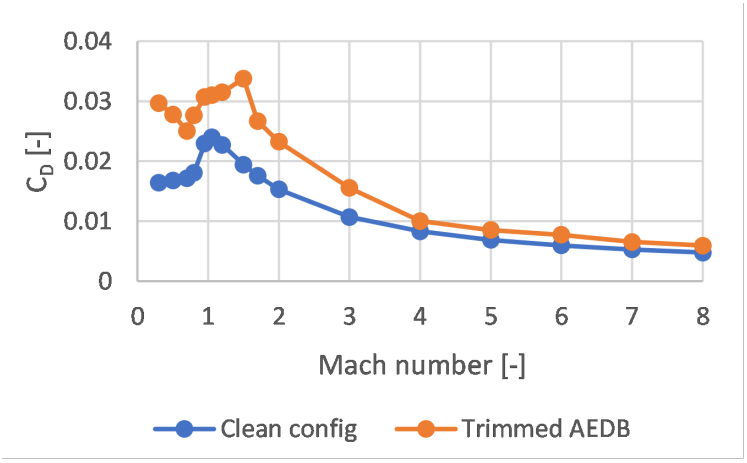

Fig. 5.69 Comparison between clean and trimmed drag coefficient

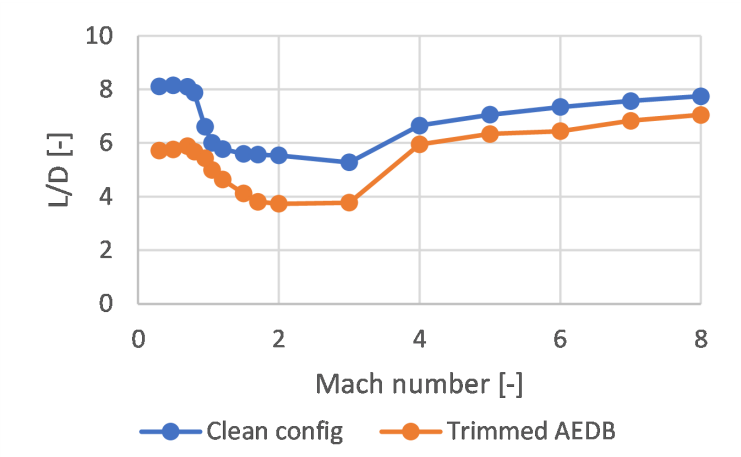

Fig. 5.70 Comparison between clean and trimmed aerodynamic efficiency

The lowest aerodynamic efficiency is found at supersonic speed, between Mach 0.9 and Mach 3, where L/D is equal to ~ 3.5. A further attempt to improve the aerodynamic performance can be carried out, relaxing the stability requirements in the transonic/low supersonic regime, and exploiting the modern, robust, and fast guidance equipment, flying unstable for a short part of the mission. Therefore, the constraint on longitudinal static stability can be neglected, and trim conditions can be evaluated accordingly. This could allow the aircraft to fly even if it is unstable. However, this condition poses great limitations for civil passenger aircraft, since they are currently designed and certified to meet stringent safety standards, which include stability requirements to ensure paseenger and crew safety. The main outcomes of this further analysis are shown in Figure 5.71, where the aerodynamic efficiency considering trimmed stable and unstable configurations are reported.

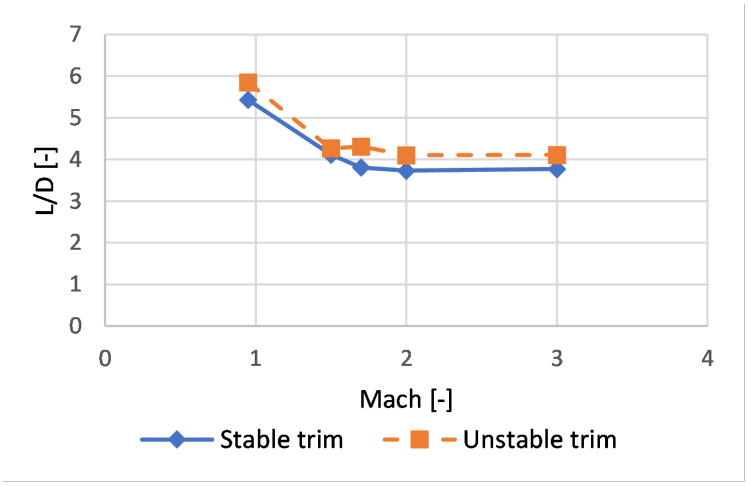

Fig. 5.71 Comparison between stable and unstable trim aerodynamic efficiency

5.2.1 Clean vs trimmed configuration: impact on mission simulation

Once the control surfaces are introduced, the performance of the vehicle along the reference mission (from Brussels to Sydney) can be computed for both the clean and trimmed configuration. The STRATOFLY propulsive database is considered for the simulation [72, 97]. The resulting altitude profiles are reported in Figure 5.72. The climb phase is completed in a shorter time with respect to the trimmed case, if the clean configuration is considered. This is due to the absence of trim drag, which results in lower total drag. However, the time difference between the two climbs is limited to less than 10 minutes. The Brussels to Sydney mission can be completed with a total travel time of less than $3h\ 30min$, for both cases. A similar trend is found looking at the Mach profiles, which are reported in Figure 5.73. The propellant mass variation over time is shown in Figure 5.74. The highest propellant consumption rate is found during the first part of the mission, when the vehicle performs the climb. As expected, during each mission phase the fuel consumption is higher for the trim configuration, due to increased drag force resulting from the deflections of the control surfaces. However, the total fuel available on-board is sufficient to complete the reference mission for both cases. Figure 5.75 reports the angle of attacks considered during the simulation. The AoA range is limited between $-2° \leq \alpha \leq 1°$, as expected for a waverider vehicle, where the α range is limited to values near $0°$. Moreover, slightly negative AoAs are needed throughout the entire

mission. This is due to the reference longitudinal body axis being parallel to the upper side of the vehicle, resulting in a windward side of the wing being at a positive angle with respect to the flow even when $AoA = 0°$. If $AoA \neq 0°$, the MR3 vehicle is in non-optimal conditions from the point of view of the aerodynamic and propulsive performance. However, low AoAs are required to avoid that the vehicle generates too much lift due to its large lifting surface, which would result in a fast gain and/or loss of altitude and an increase in the rate of climb/descent.

Eventually, the aerodynamic efficiency is also reported in Figure 5.76. The impact of the control surfaces deflections is visible. The trimmed L/D is reduced for each mission phase: the lower value equal to 3 is found during the supersonic climb, while the aerodynamic efficiency at Mach 4 is decreasing from 8 to 7, which is in accordance with the initial vehicle requirements.

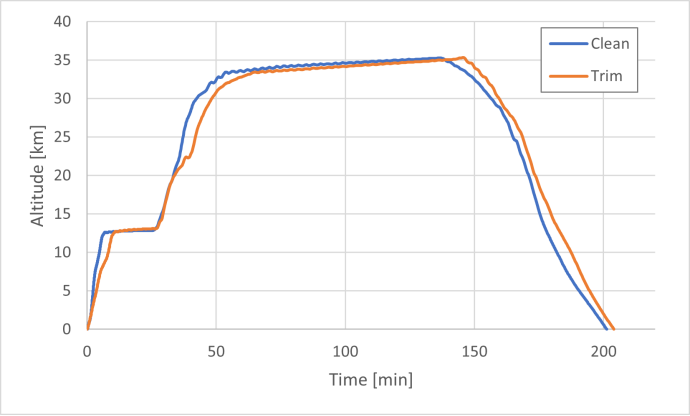

Fig. 5.72 Altitude vs time comparison for clean and trimmed aerodynamic configuration

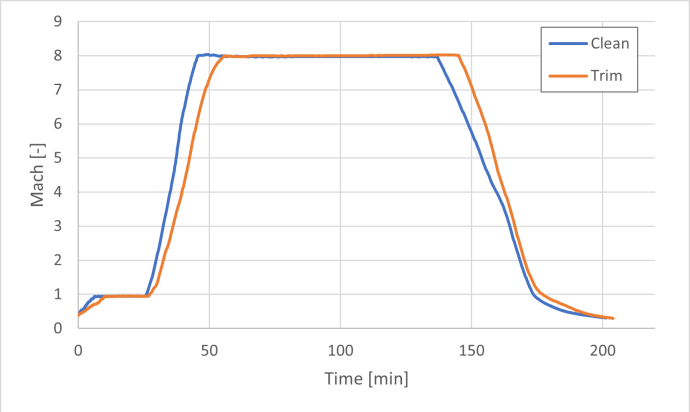

Fig. 5.73 Mach vs time comparison for clean and trimmed aerodynamic configuration

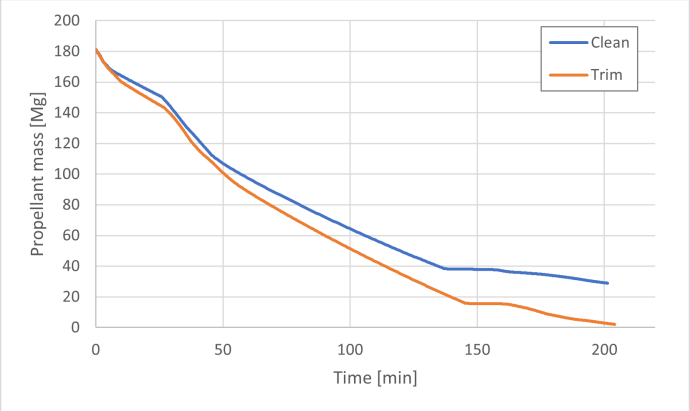

Fig. 5.74 Propellant mass vs time comparison for clean and trimmed aerodynamic configuration

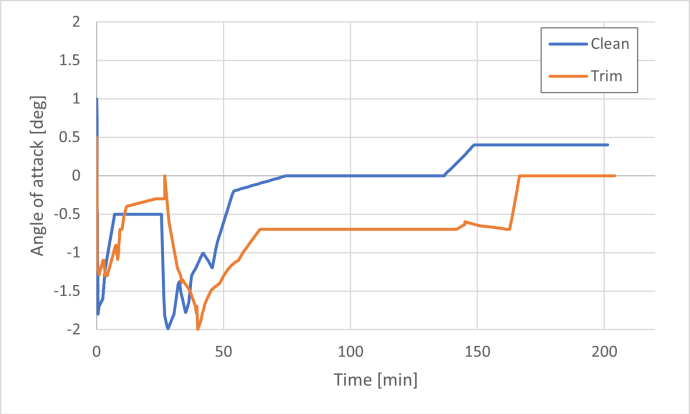

Fig. 5.75 Angle of attack vs time comparison for clean and trimmed aerodynamic configuration

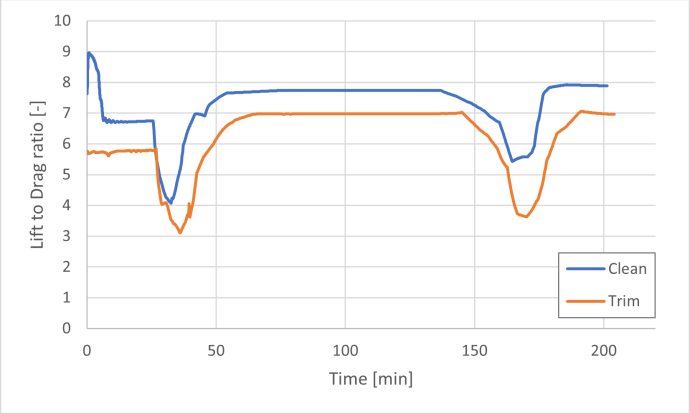

Fig. 5.76 Lift to drag ratio vs time comparison for clean and trimmed aerodynamic configuration

5.3 Take-off and landing requirement: STRATOFLY MR3 vehicle case study

High-speed passenger concepts are expected to operate within the existing ground infrastructures. For that reason, take-off and landing manoeuvres should be analysed to verify compliance with present regulations. The STRATOFLY MR3 vehicle is again considered as a reference case study, and its take-off and landing distances have been computed, according to the most updated aerodynamic and propulsive databases in subsonic conditions. The main objective of this analysis is to verify the compliance of take-off and landing requirements from current existing airports. Two different scenarios for take-off can be identified to meet the requirements specified above, depending on the thrust value considered at take-off. From the propulsive database, it is possible to derive the available thrust at sea level at Mach=0.3, which is the Mach number considered for the take-off phase. The net thrust is equal to 2334 kN. For the first scenario, 100% of the net thrust is used at take-off. For the second scenario, instead, a given thrust power rating is considered, which is equal to 47% of the net thrust. The three distances (TOR, TOD, ASD) should be computed for the MR3 vehicle and compared to the airport's maximum runway length, which has been set to 4000m. First, it is possible to compute the Balanced Field Length (BFL) for the rated thrust level (assuming engine failure(s) during the take-off run and neglecting the possibility of providing full thrust to the remaining ones). This

leads to the identification of a proper decision speed V_1 to be used as a reference in normal take-off procedures. Considering the aircraft configuration with six ATR engines and taking into account that V_1 shall be established as the speed at which the critical engine is assumed to fail, the STRATOFLY MR3 vehicle can theoretically sustain a failure during take-off run even before decision speed without stopping (i.e. it is possible to climb with 75% thrust after lift-off, so only 5 engines are necessary and OEI take-off distance is still compliant with the 4000m requirement). The BFL diagram can be evaluated considering a V_2 of about $104\mathrm{m/s}$ and a proper deceleration capability. Particularly, the STRATOFLY MR3 vehicle has very limited braking devices, concentrating 80% of the braking force in its landing gear. Typical airliners use lift dampers, spoilers and thrust reversers that together constitute 60% of deceleration capability, while for MR3 only rudders and body flaps can be partially used for this purpose. For safety reasons, a reduced deceleration of $-1.47\mathrm{m/s^2}$ is considered to compute the BFL, even if the braking assembly is sized to guarantee a typical deceleration value of about $-3.14\mathrm{m/s^2}$, while conventional aircraft have values around $-3.5\mathrm{m/s^2}$. The first acceleration phase is performed with all engines operative until the velocity V_1 is reached. The segments considered for the evaluation of the V_1 are (Figure 5.77):

- Segment A: acceleration to V_1;
- Segment B: ACC&GO, distance to perform lift-off with OEI;
- Segment C: ACC&GO, distance to clear the 35 ft obstacle;
- Segment D: ACC&STOP, reaction distance to start braking;
- Segment E: ACC&STOP, deceleration run.

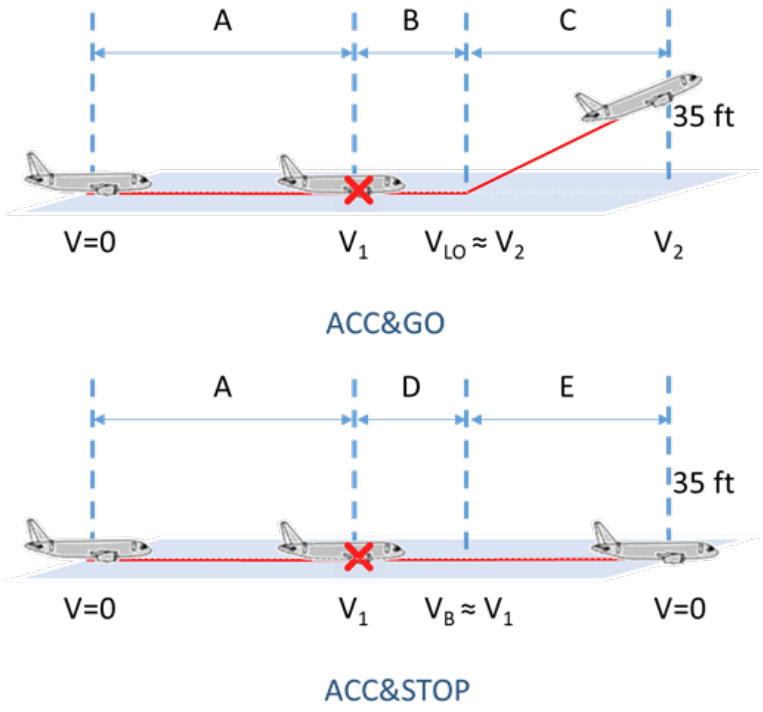

Fig. 5.77 Segments for the computation of the BFL

As a result of these considerations, Figure 5.78 and Figure 5.79 allow identifying the speed (V_1) at which, in case of engine failure (OEI) the distance required for the aircraft to stop (Accelerate & Stop scenario) and the distance required for the aircraft to continue the take-off safely (Accelerate & Go) are equal.

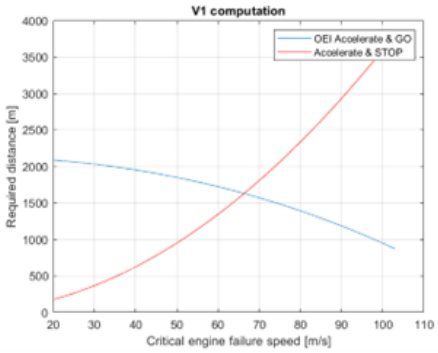

Fig. 5.78 Accelerate&Go and Accelerate&Stop distances of STRATOFLY MR3 with full thrust

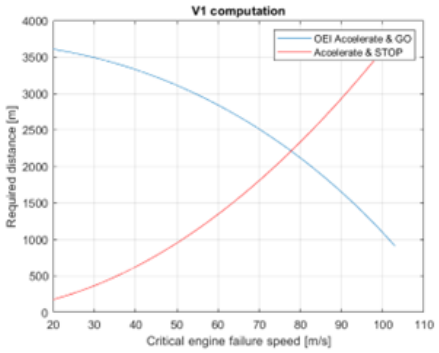

Fig. 5.79 Accelerate&Go and Accelerate&Stop distances of STRATOFLY MR3 with rated thrust

Then, the take-off distances have been evaluated accordingly for the full thrust case, and the results are reported in Table 5.3.

Table 5.3 Take-off distances computed for full thrust scenario

	Computed value[m]	Prescribed value[m]
Take-off run	1671	1922
Take-off distance	1885	2168
Acc&Stop distance	2039	-

The full thrust scenario results in a very low take-off distance, while the rated values could represent more realistic conditions. The selected approach is to consider a proper rating value for thrust at take-off, evaluating the thrust required to satisfy the reference distance of 4000m (including a 15% margin), which is a TODA valid for most runways of main international airports. A realistic value of rated thrust is computed, considering the 47% of the maximum thrust. The distances are evaluated accordingly and reported in Table 5.4. According to CS 25.113[90], the prescribed take-off distance shall include a 15% margin on the total take-off distance for safety reasons.

Table 5.4 Take-off distances computed for full rated scenario

	Computed value [m]	Prescribed value [m]
Take-off run	2865	3295
Take-off distance	3445	3542
Acc&Stop distance	3395	-

Eventually, it is possible to calculate the following velocities for the different scenarios:

- $V_{1_{FullThrust}} = 66.3\text{m/s}$;
- $V_{1_{RatedThrust}} = 77.78\text{m/s}$

These results are evaluated for sea-level conditions only. However, the STRATOFLY MR3 vehicle is supposed to operate from airports located at different altitudes equipped with a runway that satisfies the 4000m requirement. Therefore, the take-off

distances can be computed for different altitudes in the range between 0m and 4000m. The results are reported in where the TOD is computed for different altitudes and thrust ratings. The ability to perform the take-off is verified in the selected altitude range and for different thrust rating R, as can be seen in Figure 5.80.

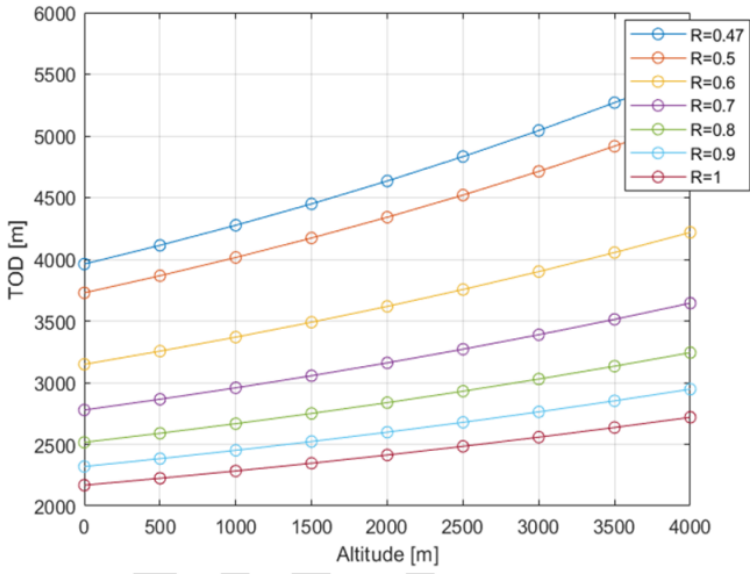

Fig. 5.80 Take-off distance at different thrust rates and altitudes

Eventually, the prescribed landing field length can be evaluated, considering that it is 66.7% higher than the theoretical value for safety margins (CS OPS 1.515). The maximum deceleration of $-3.14\text{metre}/\text{s}^2$ is assumed, while the initial speed of landing run is supposed to be equal to V_2. The resulting landing distances are computed:

- Landing run $=$ 1723m
- Theoretical landing distance $=$ 2360m
- Prescribed landing field length (CS OPS 1.515) $=$ 3935m

5.4 Environmental regulations: CO2 metric value

An aeroplane CO_2 emissions standard exists for subsonic aircraft, as defined in ICAO Annex 16 Volume III [93]. The CO_2 emission standard is a fuel-efficiency standard

which is calculated based on the Specific Air Range (SAR) and the Reference Geometric Factor (RGF). However, this standard does not extend to supersonic aircraft designs. To support the development of a potential CO_2 emissions standard for supersonic aircraft, SAR and RGF should be further analysed. For the purpose of this study, the Mach 1.5 and Mach 2 configurations are analysed. First, the reference mass points can be evaluated according to the current regulations (Equation 4.51), and the results are reported in Table 5.5.

Table 5.5 Mass points evaluated for Mach 2 and Mach 1.5 case study

	Mach 2	Mach 1.5
High-mass [Mg] $0.92 \cdot MTOM$	162.7	36.1
Low-mass [Mg] $(0.45 \cdot MTOM) + \left(0.63 \cdot MTOM^{0.924}\right)$	124.1	28.7
Mid-mass [Mg] average of high and low masses	143.4	32.4

The evaluated mass points should be compared to the actual masses of the aircraft along its reference trajectory, to understand if the subsonic formulations are valid for the supersonic cases. This can be done considering the Mach and altitude profiles derived from mission simulation, and expressed as a function of mass over MTOM ($M/MTOM$). First, the Mach 2 case study is analysed. Figure 5.81 and Figure 5.82 show that the mass points are not placed correctly at the beginning/mid/end of the cruise phase, but are shifted towards the earlier phases of the mission. The high mass point, in particular, is found during the final part of the climb phase, while the other two points are placed in cruise conditions. This result suggests that a re-definition of the mass point formulation can be required to better represent the cruise phase.

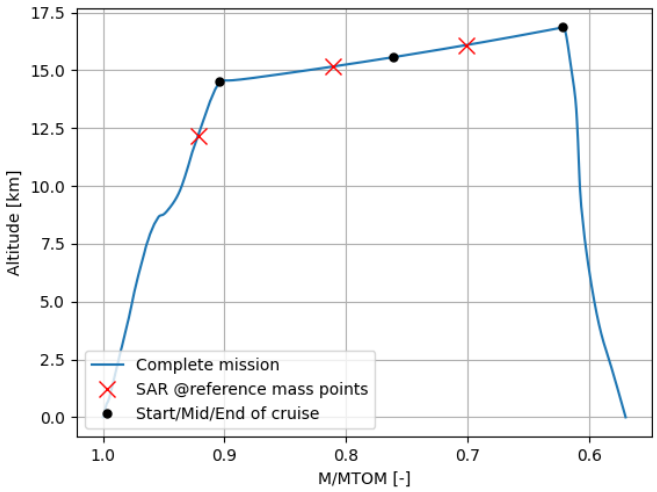

Fig. 5.81 Altitude and reference mass points evaluated along the reference mission of Mach 2 case study

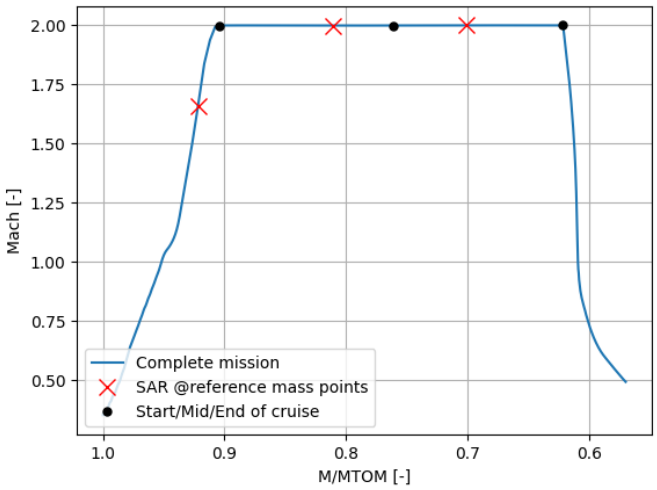

Fig. 5.82 Mach number and reference mass points evaluated along the reference mission of Mach 2 case study

Moreover, the results for the Mach 1.5 case study are also analysed, and they are slightly different with respect to the Mach 2 case. As can be seen in Figure 5.83 and Figure 5.84, the high mass point is placed correctly at the beginning of the cruise, while the other mass points are found too early during the mission, similarly to the previous case.

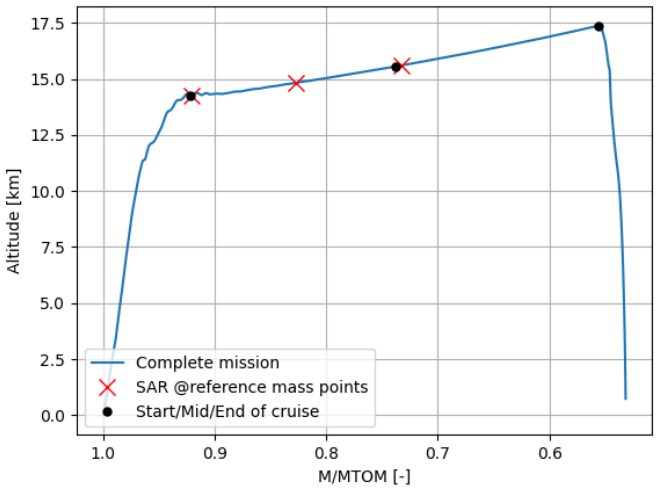

Fig. 5.83 Altitude and reference mass points evaluated along the reference mission of Mach 1.5 case study

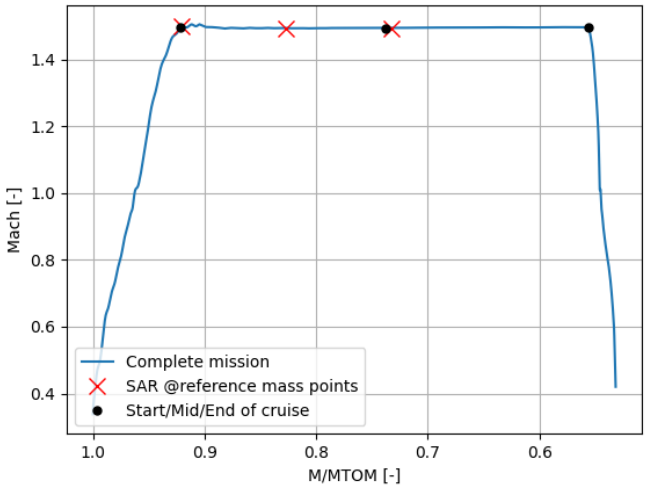

Fig. 5.84 Mach number and reference mass points evaluated along the reference mission of Mach 1.5 case study

Looking at the previous results, it becomes clear that the present regulations are not suitable to be directly applied to supersonic aircraft. Then, it could be useful to think of new formulations to be implemented for the specific case of high-speed vehicles. For that reason, the first analysis conducted during the research activity

focused on the evaluation of the actual mass points for each case study, based on the simulated trajectory at Begin Of Cruise (BOC), Mid Of Cruise (MOC), and End Of Cruise (EOC), to obtain more representative cruise mass points.

Table 5.6 Mass fractions ($M/MTOM$) at BOC, MOC and EOC for Mach 2 and Mach 1.5 case study

	M/MTOM	
	Mach 2	Mach 1.5
BOC	90%	92%
MOC	74%	73%
EOC	62%	55%

SAR values can now be computed based on the reference gross masses for the subsonic CO_2 standard and the modified reference gross masses at BOC, MOC and EOC, as can be seen in Table 5.7. It should be highlighted that those values are obtained for the cruise Mach number and do not represent optimal SAR cruise conditions. Moreover, they include the effects of the cruise climb rate, and they are not evaluated for steady, steady and level flight, as prescribed by ICAO Annex 16 [93]. However, the difference between those two conditions at the same mass value can be considered negligible.

Table 5.7 SAR values computed for reference gross masses

	High-mass	Mid-mass	Low-mass	BOC	MOC	EOC
Mach 2	0.048	0.094	0.108	0.082	0.100	0.122
Mach 1.5	0.169	0.189	0.214	0.170	0.212	0.283

Then, SAR is also evaluated along the reference trajectory, as reported in Figure 5.85 for the Mach 2 aircraft and in Figure 5.86 for the Mach 1.5 aircraft.

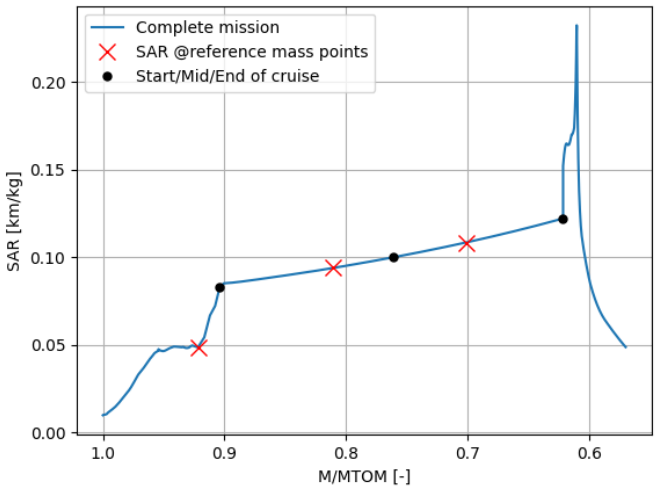

Fig. 5.85 SAR profile along the reference trajectory for Mach 2 case study

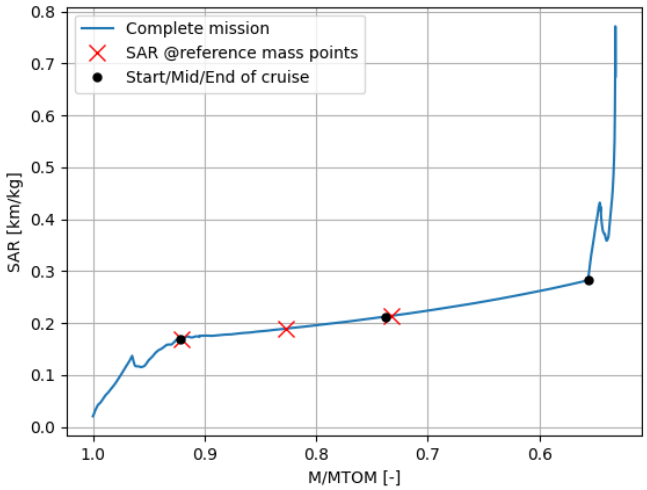

Fig. 5.86 SAR profile along the reference trajectory for Mach 1.5 case study

Since the present formulations have demonstrated to be inaccurate and/or not meaningful when used for supersonic concepts, it can be useful to identify modified reference mass-points, which should be representative of a supersonic mission cruise phase.

Moreover, it is essential to evaluate how mass-points can vary depending on the type of supersonic aircraft being considered. During previous ICAO CAEP WG3

working papers proposals for modified reference mass-points formulations have been included as functions of MTOM. For example, it is possible to consider different percentages of MTOM to evaluate the mass-points for supersonic aircraft. The equation is derived from the present subsonic regulations, where the coefficients for the evaluation of the three mass points can be modified according to the supersonic case. It can be generally expressed as:

$$modified\ mass\ points = \mathbf{a} \cdot MTOM / \mathbf{b} \cdot MTOM / \mathbf{c} \cdot MTOM \tag{5.7}$$

where **a**, **b** and **c** are three coefficients for the evaluation of high, mid and low mass points, which could be representative of the cruise phase of a general supersonic mission. Exploiting the three case studies analysed during the research activity, it has been found that the values of the three coefficients can vary depending on the cruise Mach number of each configuration. The percentage of MTOM at the beginning of cruise for the Mach 1.5, Mach 2 and Mach 5 case studies has been evaluated, and it is reported in Figure 5.87.

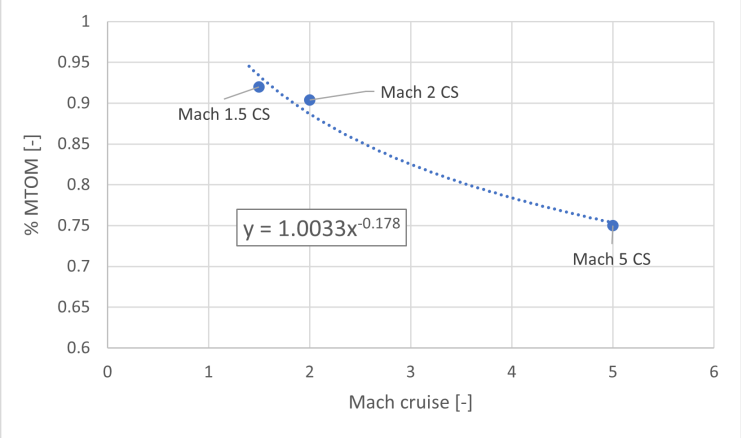

Fig. 5.87 Percentage of MTOM at begin of cruise as a function of cruise Mach number

A possible trendline is derived from the data available, to represent the MTOM percentage at BOC depending on the cruise Mach number of a given supersonic aircraft:

$$(\%MTOM)_{BOC} = 1.0033 \cdot (M_{cruise})^{-0.178} \tag{5.8}$$

Of course, this is merely a first tentative estimation, which needs to be refined considering more case studies, especially in the Mach regime between 1.4 and 2,

which is a speed where the majority of supersonic passenger aircraft is expected to fly at.

Moreover, an alternative option can also be evaluated, considering that the mass points can be expressed as a function of the fuel mass m_{fuel} instead of MTOM. This could allow for a better estimation of the cruise condition, since the mass variation is directly related to the amount of fuel burnt during the different mission phases. A general formulation is reported in Equation 5.9, where the Maximum Zero Fuel Mass (MZFM) and the fuel mass (m_{fuel}) are considered.

$$MZFM + \mathbf{a}/\mathbf{b}/\mathbf{c} \cdot \left(m_{fuel}\right) \tag{5.9}$$

As in the previous case, the three coefficient **a**, **b** and **c** have been evaluated considering the available case studies at Mach 1.5, Mach 2 and Mach 5. Table 5.8 reports the values of m_{fuel} percentage at begin of cruise for each case study.

Table 5.8 Percentage of m_{fuel} at BOC

$Mach_{cruise}$	% m_{fuel}
1.5	0.83
2.0	0.80
5.0	0.37

As can be seen, the values for the Mach 1.5 and Mach 2 concepts are very different from the ones found for the Mach 5. This can be explained considering the diverse types of vehicle included in the analysis. While the Mach 1.5 and Mach 2 case studies are characterized by a wing-body configuration, the Mach 5 case study is a waverider vehicle, which completes a different type of mission. While for all aircraft the value of fuel consumption is higher during the climb phases with respect to the cruise, where the aicraft flies in optimal conditions, the relative percentage of fuel burnt during those two phases can vary depending on the vehicle type. Indeed, waverider concepts are characterized by longer ranges, which means that the cruise phase is relatively longer than the one of a conventional low supersonic aircraft. This results in a larger amount of fuel consumed during cruise with respect to the total amount of fuel on-board.

Eventually, an additional analysis on SAR is carried on, to further study the cruise performance. The aircraft's cruise Mach number is varied from low speed to the

maximum design speed, to cover each potential cruise point. At the same time, the altitude is varied from 0 km up to the aircraft's maximum cruise altitude. Different aircraft gross weights are also considered and expressed as fractions of the MTOM (from $0.5 \cdot MTOM$ to $MTOM$). First, the relation between SAR and Mach number is analysed for different constant weights at SAR-optimal altitude, (the altitude where SAR is maximum for a specific weight and Mach number). Figure 5.88 reports the results for the Mach 2 case study.

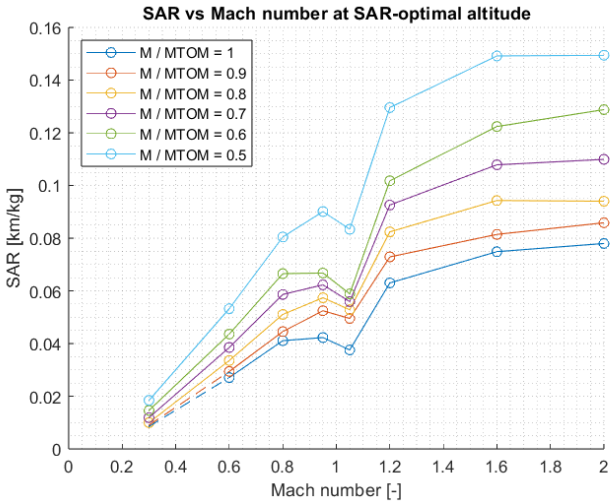

Fig. 5.88 SAR values for different Mach numbers at SAR-optimal altitude

For higher Mach numbers SAR is also higher, and the optimal SAR is found for the design Mach number equal to 2. This trend is valid for each weight considered. However, SAR decreases in the transonic regime, where the aerodynamic efficiency is lower, due to higher drag, higher required thrust, and relatively higher fuel consumption. Moreover, the variation of SAR for different altitude at SAR-optimal Mach number is also analysed Figure 5.89. SAR values are higher for increasing altitudes, and the optimal SAR is observed at the maximum altitude of 18 km. The same trend is found for all the weights considered.

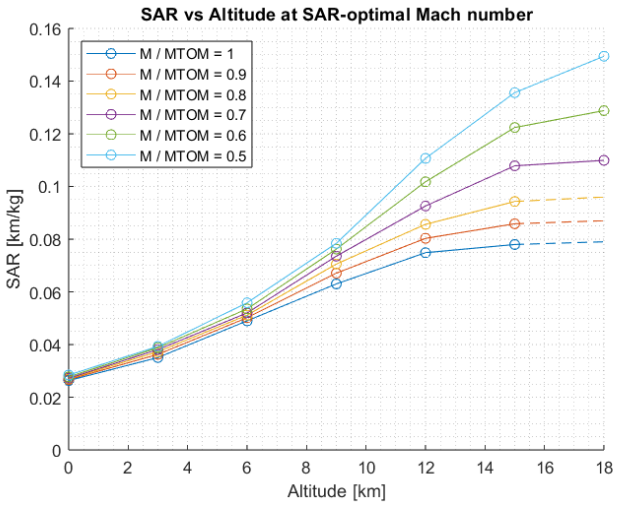

Fig. 5.89 SAR values for different altitudes at SAR-optimal Mach number

Eventually, the CO_2 MV can be computed for the case studies considered, exploiting the SAR data evaluated previously. The computed CO_2 MV are reported in Figure 5.90, where the subsonic limits are also shown: the red line represents the limit for subsonic In-Production (InP) types, as specified by [93], while the blue line is referred to subsonic New Types (NT) [93]. The CO_2 MV is evaluated for both the Mach 2 and Mach 1.5 configurations. Moreover, it is computed considering both the definition for subsonic aircraft and the adapted mass points at BOC, MOC and EOC. Two others concepts are also included, a NASA business jet concept at Mach 1.4 and a DLR business jet concept at Mach 1.6. As expected, all the supersonic aircraft considered results in CO_2 MV which are higher than the subsonic limits. Moreover, for larger aircraft (and higher MTOM) the different concepts exceeds the limits by a greater value. However, if the metric value is computed considering the modified mass points at BOC/MOC/EOC, significantly lower values are found with respect to the subsonic defininition of mass-points.

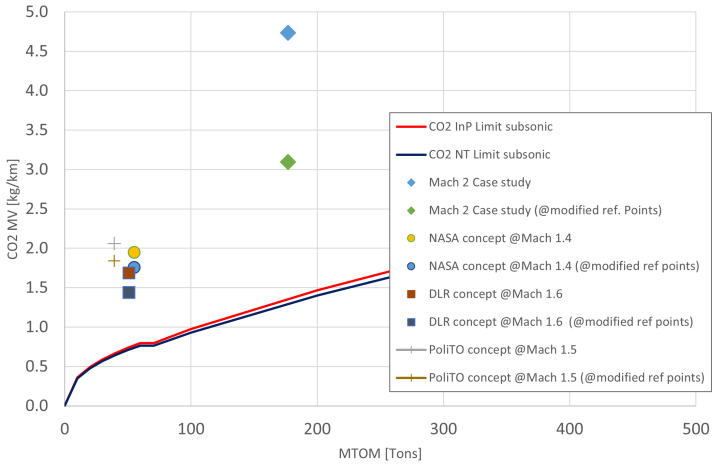

Fig. 5.90 CO_2 MV estimation

Chapter 6

Conclusions

This thesis aims at suggesting new methodologies and tools for the conceptual design of high-speed transport aircraft, with the main objective of supporting the definition of environmental regulations. Specifically, together with a detailed investigation of the high-speed aircraft developed or merely studied during the aviation and space history, particular attention has been paid to the conceptual and preliminary design phases of high-speed passenger concepts. The main drivers affecting the high-speed aircraft design have been analysed, focusing especially on the aerodynamic and propulsive characteristics of this kind of concepts. Moreover, the environmental issues of high-speed aircraft should also be included in the analysis, since it is an essential aspect for the design of environmentally sustainable aircraft. In particular, a description of the aircraft greenhouse gases and pollutant emissions, noise and sonic boom is included to provide an overview of those fundamental topics.

This thesis has been carried out within the framework of two European Funded projects, focusing on high-speed passenger transport, which are the STRATOFLY and MORE&LESS projects. Some of the most important design topics have been analysed, such as the aerodynamic and stability characteristics estimation at a preliminary level, as well as the mission simulation. In this context, preliminary aerodynamic models, already available in literature and that can be used for the estimation of the aerodynamic coefficients of high-speed aircraft, are introduced, to compensate for the lack of higher fidelity data during the first phases of the design. First, the accuracy of the selected models is evaluated on a set of case studies which are available among the concepts studied in the STRATOFLY and MORE&LESS

projects. The work is carried on considering two different categories of aircraft, based on their configuration type: the first one considers low supersonic wing-body aircraft designed to cruise at Mach number up to 3, while the second one involves a waverider configuration for cruise Mach greater than 5. Then, based on the higher fidelity aerodynamic data available within the projects' consortium, a comparison between the results obtained through the models and the high-fidelity one is performed. The comparison leads to the identification of possible modifications to the models, which are introduced to better capture the peculiar aerodynamic characteristics of high-speed aircraft. The aircraft's reference trajectory is also computed through mission simulation, to estimate the impact of the aerodynamic preliminary evaluation on the overall mission performance estimation.

As a next step, once the flight control surfaces are fully characterized, it is possible to study the aircraft's static stability and trimmability. The methodology used was based on the creation of trim maps, which contain all the possible combinations of control surfaces deflections that satisfy the stability and trim conditions. Those data are then exploited to perform a further mission simulation, which is then compared to the one evaluated cosidering the aerodynamic data of the clean configuration only. As expected, the trimmed aerodynamics highly affects the aicraft's performance along the mission, reducing the aerodynamic efficiency especially during the transonic/low supersonic climb phases. This highlights the importance of including the analysis on the aicraft's stability and trimmability since the very early phases of the design.

Together with the estimation of the vehicle performance during the mission, the required take-off and landing distance is also evaluated. This is a fundamental aspect to be verified, since the high-speed aicraft are supposed to operate within the current airport infrastructure. For that reason, it is useful to verify that the runways of the most important international airport are sufficiently long to allow for a safe take-off and landing, according to the prescribed regulations. Moreover, it can also be considered that this type of requirement can be relatively easy to satisfy for the low superonic concepts, which are characterized by a quite common configuration. However, this requirement can be unfeasible for hyperosic waveriders, which usually could require a much longer runway length, due to their larger dimension and mass. Hence, the required take-off and landing distance has been evaluated and verified for the STRATOFLY vehicle, considering a maximum length of 4000 m.

Eventually, the dataset evaluated throughout the research activity has been exploited to support the ongoing work to define CO_2 emission standards specifically tailored for the certification of high-speed aircraft. First, it has been proved that the present regulations are not suitable to be directly applied to supersonic case studies. Indeed, the mass-points have been evaluated and compared to the actual location of the main cruise reference points (i.e. begin and end of cruise) for the different case studies available. It has been verified that the mass-point definition valid for subsonic aircraft is not appropriate for supersonic concepts. Some modifications to the current formulation have also been proposed, and can be refined as soon as more case studies will be available. Moreover, the CO_2 MV is also computed and compared to the available data for other supersonic concepts from NASA and DLR, as well as to the limit imposed to subsonic aircraft certification. It has been found that the CO_2 MV evaluated for supersonic aircraft is higher than the limits imposed for subsonic aircraft certification, highlighting the need for a different metric value to be applied to supersonic concepts.

While the proposed methodology proved to be efficent for a preliminary evaluation of the aerodynamic and mission performance of different types of high-speed aircraft, the results obtained should be interpreted carefully. Indeed, those tools are intended for the preliminary and conceptual design of high-speed concepts, being based on simplified formulations and a limited set of case studies. Of course, future works may benefit from the availability of additional high-speed configurations, which could be exploited to refine and improve the aerodynamic models, and, as a consequence, the estimation of the aircraft's performance along the trajectory. Moreover, additional concepts would also be very beneficial to define new metric values specifically tailored for high-speed aircraft, to be applied for the certification of supersonic passenger transport systems.

References

[1] European Commission. The european green deal. https://commission.europa.eu/strategy-and-policy/priorities-2019-2024/european-green-deal_en, 2019. Accessed: 2024-01-10.

[2] Nicole Viola, Roberta Fusaro, Oscar Gori, Marco Marini, Pietro Roncioni, Guido Saccone, Bayindir H. Saracoglu, Ali Can Ispir, Christer Fureby, Thommie Nilson, Christian Iron, Axel Vincent, Jan Martinez Schramm, Volker Grewe, John Emmerig, Didier Hauglustaine, Florian Linke, and Daniel Bodmer. Stratofly mr3 - how to reduce the environmental impact of high-speed transportation. *AIAA Scitech 2021 Forum*, 2020.

[3] Nicole Viola, Roberta Fusaro, Bayindir Saracoglu, Christophe Schram, Volker Grewe, Jan Martinez, Marco Marini, Santiago Hernandez, Karel Lammers, Axel Vincent, Didier Hauglustaine, Bernd Liebhardt, Florian Linke, and Christer Fureby. Main challenges and goals of the h2020 stratofly project. *Aerotecnica Missili e Spazio*, 100(2):95–110, 2021. ISSN 2524-6968. doi: 10.1007/s42496-021-00082-6. URL https://doi.org/10.1007/s42496-021-00082-6.

[4] CORDIS. Mdo and regulations for low-boom and environmentally sustainable supersonic aviation. https://cordis.europa.eu/project/id/101006856, 2021. Accessed: 2024-01-10.

[5] Thomas Rötger, Chris Eyers, and Roberta Fusaro. A review of the current regulatory framework for supersonic civil aircraft: Noise and emissions regulations. *Aerospace*, 11(1), 2024. ISSN 2226-4310. doi: 10.3390/aerospace11010019. URL https://www.mdpi.com/2226-4310/11/1/19.

[6] International Civil Aviation Organization (ICAO). Committee on aviation environmental protection (caep). https://www.icao.int/environmental-protection/Pages/Caep.aspx. Accessed: 2024-01-11.

[7] Claus Weiland. *Aerodynamic Data of Space Vehicles*. Springer, 01 2014. ISBN 978-3-642-54167-4. doi: 10.1007/978-3-642-54168-1.

[8] Kevin Bowcutt. Physics drivers of hypersonic vehicle design. In *22nd AIAA International Space Planes and Hypersonics Systems and Technologies Conference*, 09 2018. doi: 10.2514/6.2018-5373.

[9] John David Anderson. *Fundamentals of Aerodynamics*. McGraw-Hill Education, 1984.

[10] John David Anderson. *Hypersonic and High-Temperature Gas Dynamics*. American Institute of Aeronautics and Astronautics (AIAA), 2019. doi: https://doi.org/10.2514/4.105142.

[11] Danyel Raymer. *Aircraft Design: A Conceptual Approach*. American Institute of Aeronautics and Astronautics, 2018.

[12] Charles R. Mcclinton. High speed / hypersonic aircraft propulsion technology development. In *NATO RTO - Educational Notes Paper*, 2008.

[13] Dries Verstraete. *The Potential of Liquid Hydrogen for long range aircraft propulsion*. PhD thesis, Cranfield University, 2009.

[14] Fuel Cells Hydrogen 2 Joint Undertaking. *Hydrogen-powered aviation. A fact-based study of hydrogen technology, economics, and climate impact by 2050*. Publications Office, 2020. doi: doi/10.2843/471510.

[15] European Commission. Proposal for a regulation of the european parliament and of the council on ensuring a level playing field for sustainable air transport, 2021.

[16] Susanne Becken, Brendan Mackey, and David S. Lee. Implications of preferential access to land and clean energy for sustainable aviation fuels. *Science of The Total Environment*, 886:163883, 2023. ISSN 0048-9697. doi: https://doi.org/10.1016/j.scitotenv.2023.163883. URL https://www.sciencedirect.com/science/article/pii/S0048969723025044.

[17] By Dennis D. Miller and Ross M. Welch. Food system strategies for preventing micronutrient malnutrition. *Food Policy*, 42:115–128, 2013. ISSN 0306-9192. doi: https://doi.org/10.1016/j.foodpol.2013.06.008. URL https://www.sciencedirect.com/science/article/pii/S0306919213000742.

[18] Martina Perišić, Ernest Barceló, Katarina Dimic-Misic, Monireh Imani, and Vesna Spasojević Brkić. The role of bioeconomy in the future energy scenario: A state-of-the-art review. *Sustainability*, 14(1), 2022. ISSN 2071-1050. doi: 10.3390/su14010560. URL https://www.mdpi.com/2071-1050/14/1/560.

[19] Parash Agarwal, Xiaoxiao Sun, Pierre Gauthier, and Vishal Sethi. Injector design space exploration for an ultra-low nox hydrogen micromix combustion system. 06 2019. doi: 10.1115/GT2019-90833.

[20] Eytan J. Adler and Joaquim R.R.A. Martins. Hydrogen-powered aircraft: Fundamental concepts, key technologies, and environmental impacts. *Progress in Aerospace Sciences*, 141:100922, 2023. ISSN 0376-0421. doi: https://doi.org/10.1016/j.paerosci.2023.100922. URL https://www.sciencedirect.com/science/article/pii/S0376042123000386. Special Issue on Green Aviation.

[21] Johannes Pletzer and Volker Grewe. Sensitivities of atmospheric composition and climate to altitude and latitude of hypersonic aircraft emissions. *EGUsphere*, 2023:1–54, 2023. doi: 10.5194/egusphere-2023-1777. URL https://egusphere.copernicus.org/preprints/2023/egusphere-2023-1777/.

[22] *Annex 16. Environmental Protection - Volume I - Aircraft Noise*, 2017. (ICAO) International Civil Aviation Organization.

[23] Grazia Piccirillo, Nicole Viola, Roberta Fusaro, and Luigi Federico. Guidelines for the lto noise assessment of future civil supersonic aircraft in conceptual design. *Aerospace*, 9(1), 2022. ISSN 2226-4310. doi: 10.3390/aerospace9010027. URL https://www.mdpi.com/2226-4310/9/1/27.

[24] International Civil Aviation Organization (ICAO). Reduction of noise at source. https://www.icao.int/environmental-protection/pages/reduction-of-noise-at-source.aspx, 2019. Accessed: 2023-12-29.

[25] SENECA. (LTO) noiSe and EmissioNs of supErsoniC Aircraft. https://seneca-project.eu/, 2021. Accessed: 2024-01-05.

[26] *Annex 16. Environmental Protection - Volume I - Aircraft Engine Emissions*, 2023. (ICAO) International Civil Aviation Organization.

[27] Egbert Torenbeek. *Essentials of Supersonic Commercial Aircraft Conceptual Design*. Wiley, 2020.

[28] Jay Casper, Susan E. Cliff, S. D. Thomas, M. A. Park, Matthew S. McMullen, John E. Melton, and Donald A. Durston. Assessment of near-field sonic boom simulation tools. *Collection of Technical Papers - AIAA Applied Aerodynamics Conference*, 08 2008. doi: 10.2514/6.2008-6592.

[29] Christian Gelzer. First generation x-1. https://www.nasa.gov/aeronautics/first-generation-x-1/, 2014. Accessed: 2024-01-05.

[30] Dennis R. Jenkins, Tony R. Landis, and Jay Miller. *American X-Vehicles: An Inventory X-1 to X-50 Centennial of Flight Edition*. National Aeronautics and Space Administration (NASA), 2003.

[31] Dede Dinius. Second generation x-1. https://www.nasa.gov/aeronautics/second-generation-x-1/, 2014. Accessed: 2024-01-05.

[32] Christian Gelzer. D-558-ii skyrocket. https://www.nasa.gov/aeronautics/d-558-ii-transonic-aircraft/, 2014. Accessed: 2024-01-05.

[33] Stuart Wilson. *Combat Aircraft Since 1945*. Aerospace Publications, 2000.

[34] Tony Buttler and Jean-Louis Delezenne. *X-Planes of Europe: Secret Research Aircraft from the Golden Age 1946-1974*. Hikoki Publications, 2012.

[35] Dryden Flight Research Center. Sr-71 blackbird. Technical report, National Aeronautics and Space Administration (NASA), 2008. URL https://www.nasa.gov/wp-content/uploads/2021/09/495839main_FS-030_SR-71.pdf.

[36] Christian Gelzer. Xb-70 valkyrie. https://www.nasa.gov/aeronautics/xb-70-valkyrie, 2014. Accessed: 2024-01-05.

[37] Joseph R. Chambers. Innovation in flight: Research of the nasa langley research center on revolutionary advanced concepts for aeronautics. Technical report, National Aeronautics and Space Administration (NASA), 2005.

[38] Boom supersonic. Overture. https://boomsupersonic.com/overture, 2023. Accessed: 2023-12-29.

[39] Robert Margetta. Nasa targets 2024 for first flight of x-59 experimental aircraft. https://www.nasa.gov/aeronautics/nasa-targets-2024-for-first-flight-of-x-59-experimental-aircraft/, 2023. Accessed: 2023-12-29.

[40] Christian Gelzer. X-15 hypersonic research aircraft. https://www.nasa.gov/centers-and-facilities/armstrong/x-15/, 2014. Accessed: 2024-01-05.

[41] Ray A. Williamson. Developing the space shuttle. *Exploring the Unknown: Selected Documents in the History of the U.S. Civil Space Program, Volume IV: Accessing Space*, 1999.

[42] Larry Schwelkart and Richard P. Hallion. The hypersonic revolution. case studies in the history of hypersonic technology. volume 3: The quest for the orbital jet: The national aero-space plane program (1983-1995). Technical report, AIR FORCE HISTORICAL STUDIES OFFICE BOLLING AFB DC, 1997.

[43] National Aeronautics and Space Administration (NASA). Nasa hyper-x program demonstrates scramjet technologies. https://www.nasa.gov/wp-content/uploads/2021/09/171371main_FS-040-DFRC.pdf, 2021. Accessed: 2024-01-10.

[44] Christopher M. Rondeau and Timothy R. Jorris. X-51a scramjet demonstrator program: Waverider ground and flight test. In *SFTE 44th International / SETP Southwest Flight Test Symposium*, 2013. URL https://apps.dtic.mil/sti/citations/ADA593742.

[45] Erik Seedhouse. *Virgin Galactic: The First Ten Years*. Springer, 01 2015. ISBN 978-3-319-09261-4. doi: 10.1007/978-3-319-09262-1.

[46] Hideyuki Taguchi, Hiroaki Kobayashi, Takayuki Kojima, Atsushi Ueno, Shunsuke Imamura, Motoyuki Hongoh, and Kenya Harada. Research on hypersonic aircraft using pre-cooled turbojet engines. *Acta Astronautica*, 73:164–172, 2012. ISSN 0094-5765. doi: https://doi.org/10.1016/j.actaastro.2011.10.006. URL https://www.sciencedirect.com/science/article/pii/S0094576511003080.

[47] Paulo GP Toro, Marco A Minucci, Tiago Rolim, Roberto Follador, Alberto Santos, Giannino Camillo, and Luiz Barreta. Brazilian 14-x hypersonic aerospace vehicle project. In *18th AIAA/3AF International Space Planes and Hypersonic Systems and Technologies Conference*, page 5851, 2012.

[48] D.E. Koelle and H. Kuczera. Sänger ii, an advanced launcher system for europe. *Acta Astronautica*, 19(1):63–72, 1989. ISSN 0094-5765. doi: https://doi.org/10.1016/0094-5765(89)90009-X. URL https://www.sciencedirect.com/science/article/pii/009457658990009X.

[49] Martin Sippel, Sven Stappert, Leonid Bussler, and Sholto O. Forbes-Spyratos. Technical progress of multiple-mission reusable launch vehicle spaceliner. In *HiSST 1st International Conference on High-Speed Vehicle Science & Technology*, 2018.

[50] J. Steelant, A. Bond, A. Götz, K. Hannemann, C. Bruno, and J. Longo. Lapcatlong-term advanced propulsion concepts and technologies. publishable final activity report. Technical report, European Space Agency (ESA), 2008.

[51] Farouk Jivraj, Richard Varvill, Alan Bond, and Guillermo Paniagua. The scimitar precooled mach 5 engine. In *2nd European Conference for Aero-Space Sciences*, 07 2007.

[52] J. Steelant, J. Longo, M. Kuhn, S. Soller, and M. Bouchez. Atllas aerodynamic and thermal load interactions withlightweight advanced materials for high speed flight. final public report: Objectives and achievements for the atllas project. Technical report, ESA-ESTEC, 2006.

[53] J.M.A. Longo, R. Dittrich, Daniel Banuti, M. Sippel, Josef Klevanski, U. Atanassov, Gérald Carrier, Ph Duveau, Itham Salah El Din, R. Thepot, A. Loubeau, François Coulouvrat, Rolf Jarlas, H. Rabia, David Perigo, and Johan Steelant. Concept study for a mach 6 transport aircraft. In *47th AIAA Aerospace Sciences Meeting*, 01 2009.

[54] Johan Steelant. Sustained hypersonic flight in europe: First technology achievements within lapcat ii. In *16th AIAA/DLR/DGLR International Space Planes and Hypersonic Systems and Technologies Conference*, 2009. ISBN 978-1-60086-942-6. doi: 10.2514/6.2011-2243.

[55] Johan Steelant, Richard Varvill, Sebastien Defoort, Klaus Hannemann, and Marco Marini. Achievements obtained for sustained hypersonic flight within the lapcat-ii project. In *20th AIAA International Space Planes and Hypersonic Systems and Technologies Conference*, 07 2015. doi: 10.2514/6.2015-3677.

[56] Johan Steelant and Tobias Langener. The lapcat-mr2 hypersonic cruiser concept. In *ICAS*, St. Petersburg (RU), 09 2014.

[57] Johan Steelant, Tobias Langener, Klaus Hannemann, Marco Marini, Laurent Serre, Marc Bouchez, and Francois Falempin. Conceptual design of the high-speed propelled experimental flight test vehicle hexafly. In *20th AIAA International Space Planes and Hypersonic Systems and Technologies Conference*, 07 2015. doi: 10.2514/6.2015-3539.

[58] J. Steelant, C. Walton, and L. Serre. High-speed experimental fly vehicles. final report. Technical report, European Space Agency – European Space Research and Technology Centre (ESA-ESTEC), 2014.

[59] Sara Di Benedetto, Maria Pia Di Donato, Antonio Schettino, Roberto Scigliano, Francesco Nebula, Gianfranco Morani, Domenico Cristillo, Marco Marini, Salvatore Cardone, Johan Steelant, and Victor Fernandez Villace. The high-speed experimental flight test vehicle of hexafly-int: a multidisciplinary design. *CEAS Space Journal*, 13:291 – 316, 2021. URL https://link.springer.com/article/10.1007/s12567-020-00341-5.

[60] Johan Steelant, Victor Fernandez Villace, Alexander Kallenbach, Alexander Wagner, Jean-Yves Andro, Sara Di Benedetto, Bayindir Saracoglu, Sergey Chernyshev, Anatoly Gubanov, Vadim Talyzin, Nina Voevodenko, Nikolay Kukshinov, Alexander Prokhorov, Nikolay Grigoriev, Andrew Neely, Dries Verstraete, and David Buttsworth. Flight testing designs in hexafly-int for high-speed transportation. In *International Conference on High-Speed Vehicle Science and Technology 2018 (HiSST)*, 11 2018.

[61] Destinus. https://www.destinus.ch/, 2023. Accessed: 2024-01-05.

[62] Hermeus. https://www.hermeus.com/, 2023. Accessed: 2024-01-05.

[63] Stratospheric flying opportunities for high-speed propulsion concepts. https://cordis.europa.eu/project/id/769246. Accessed: 2024-01-23.

[64] Johan Steelant. Atllas: Aero-thermal loaded material investigations for high-speed vehicles. In *15th AIAA International Space Planes and Hypersonic Systems and Technologies Conference*, 04 2008. ISBN 978-1-60086-985-3. doi: 10.2514/6.2008-2582.

[65] Johan Steelant, Mats Dalenbring, Markus Kuhn, MarcBouchez, and Jens von Wolfersdorf. Achievements obtained within atllas-ii on aero-thermal loaded material investigations for high-speed vehicles. In *21st AIAA International Space Planes and Hypersonics Technologies Conference*, 03 2017. doi: 10.2514/6.2017-2393.

[66] Emmanuel Blanvillain and Guy Gallic. Hikari: Paving the way towards high speed air transport. In *20th AIAA International Space Planes and Hypersonic Systems and Technologies Conference*, 07 2015. doi: 10.2514/6.2015-3676.

[67] Nunzia Favaloro, Attilio Rispoli, Ludovico Vecchione, Giuseppe Pezzella, Valerio Carandente, Roberto Scigliano, Marco Cicala, Gianfranco Morani, and Johan Steelant. Design analysis of the high-speed experimental flight test

vehicle hexafly-international. In *20th AIAA International Space Planes and Hypersonic Systems and Technologies Conference*, 07 2015. doi: 10.2514/6.2015-3607.

[68] Davide Ferretto, Roberta Fusaro, and Nicole Viola. Innovative multiple matching charts approach to support the conceptual design of hypersonic vehicles. *Proceedings of the Institution of Mechanical Engineers, Part G: Journal of Aerospace Engineering*, 234(12):1893–1912, 2020. doi: 10.1177/0954410020920037. URL https://doi.org/10.1177/0954410020920037.

[69] Davide Ferretto, Roberta Fusaro, and Nicole Viola. A conceptual design tool to support high-speed vehicle design. In *AIAA AVIATION 2020 FORUM*, 06 2020. doi: 10.2514/6.2020-2647.

[70] Davide Ferretto and Nicole Viola. Preliminary design and simulation of a thermal management system with integrated secondary power generation capability for a mach 8 aircraft concept exploiting liquid hydrogen. *Aerospace*, 10:180, 02 2023. doi: 10.3390/aerospace10020180.

[71] Nicole Viola, Pietro Roncioni, Oscar Gori, and Roberta Fusaro. Aerodynamic characterization of hypersonic transportation systems and its impact on mission analysis. *Energies*, 14(12), 2021. ISSN 1996-1073. doi: 10.3390/en14123580. URL https://www.mdpi.com/1996-1073/14/12/3580.

[72] Ali İspir, Pedro Gonçalves, and Bayindir Saracoglu. Analysis of a combined cycle propulsion system for stratofly hypersonic vehicle over an extended trajectory. *MATEC Web of Conferences*, 304:03001, 01 2019. doi: 10.1051/matecconf/201930403001.

[73] Christer Fureby. Subgrid models, reaction mechanisms, and combustion models in large-eddy simulation of supersonic combustion. *AIAA Journal*, 59:1–13, 09 2020. doi: 10.2514/1.J059597.

[74] Roberto Scigliano, Valeria De Simone, Marco Marini, Pietro Roncioni, Roberta Fusaro, and Nicole Viola. Preliminary finite element thermal analysis of stratofly hypersonic vehicle. 2020.

[75] Roberto Scigliano, Valeria De Simone, Roberta Fusaro, Davide Ferretto, Marco Marini, and Nicole Viola. Cooling system of stratofly hypersonic vehicle: conceptual design, numerical analysis and verification. In *Proceedings of the 33rd Congress of the International Council of the Aeronautical Sciences*, Stockholm, Sweden, September 2022.

[76] Roberta Fusaro, Davide Ferretto, Nicole Viola, Roberto Scigliano, Valeria De Simone, and Marco Marini. Liquid metals heat-pipe solution for hypersonic air-intake leading edge: Conceptual design, numerical analysis and verification. *Acta Astronautica*, 197:336–352, 2022. ISSN 0094-5765. doi: https://doi.org/10.1016/j.actaastro.2022.05.034. URL https://www.sciencedirect.com/science/article/pii/S0094576522002533.

[77] Roberto Scigliano, Valeria De Simone, Roberta Fusaro, Davide Ferretto, and Nicole Viola. Numerical simulation of heat pipe thermal performance for aerospace cooling system applications. *Aerospace*, 11(1), 2024. ISSN 2226-4310. doi: 10.3390/aerospace11010085. URL https://www.mdpi.com/2226-4310/11/1/85.

[78] Miguel Rodríguez-Segade, Santiago Hernandez, Jacobo Diaz, and Aitor Baldomir. A bi-level approach for the structural optimization of the hypersonic stratofly mr3 vehicle. In *AIAA Scitech 2021 Forum*, 01 2021. doi: 10.2514/6.2021-0098.

[79] Charles Edward Cockrell, Lawrence D. Huebner, and Dennis B. Finley. Aerodynamic characteristics of two waverider-derived hypersonic cruise configurations. Technical report, National Aeronautics and Space Administration (NASA), 1996.

[80] John Anderson, Jr and Mark Lewis. Hypersonic waveriders-where do we stand? In *31st Aerospace Sciences Meeting*, page 399, 1993.

[81] Kevin G. Bowcutt, John D. Anderson, and Diego Capriotti. Viscous optimized hypersonic waveriders. In *25th AIAA Aerospace Sciences Meeting*, 1987.

[82] Feng Ding, Jun Liu, Chi bing Shen, Zhen Liu, Shao hua Chen, and Xiang Fu. An overview of research on waverider design methodology. *Acta Astronautica*, 140:190–205, 2017. ISSN 0094-5765. doi: https://doi.org/10.1016/j.actaastro.2017.08.027. URL https://www.sciencedirect.com/science/article/pii/S0094576517309013.

[83] Frederick Ferguson, Nastassja Dasque, Mookesh Dhanasar, and Isaiah Blankson. Waverider design, analysis and performance evaluation. In *57th AIAA/ASCE/AHS/ASC Structures, Structural Dynamics, and Materials Conference*, 01 2016. doi: 10.2514/6.2016-1663.

[84] Davide Ferretto. *Innovative Model Based Systems Engineering approach for the design of hypersonic transportation systems*. PhD thesis, Politecnico di Torino, 2020.

[85] Davide Ferretto, Oscar Gori, Roberta Fusaro, and Nicole Viola. Integrated flight control system characterization approach for civil high-speed vehicles in conceptual design. *Aerospace*, 10(6), 2023. ISSN 2226-4310. doi: 10.3390/aerospace10060495. URL https://www.mdpi.com/2226-4310/10/6/495.

[86] Nicole Viola, Roberta Fusaro, Davide Ferretto, Oscar Gori, Marco Marini, Pietro Roncioni, Bora Orcun Cakir, Ali Can Ispir, and Bayindir Husein Saracoglu. Hypersonic aircraft and mission concept re-design to move from mach 8 to mach 5 operations. In *33rd Congress of the International Council of the Aeronautical Sciences*, pages 1218–1234, Stockholm, SE, September 2022.

[87] Louis J. Williams. Estimated aerodynamics of all-body hypersonic aircraft configurations. Technical report, NASA Ames Research Center Moffet Field, CA, United States, 1971.

[88] Astos solutions GmbH. https://www.astos.de/, 2024. Accessed: 2024-01-05.

[89] US Air Force National Oceanic and Atmospheric Administration(NOAA), National Aeronautics and Space Administration(NASA). U.s. standard atmosphere (1976). Technical report, National Oceanic and Atmospheric Administration(NOAA), National Aeronautics and Space Administration(NASA), US Air Force, 1976.

[90] EASA. Certification specifications and acceptable means of compliance for largeaeroplanes cs-25. amendment 24. Technical report, European Aviation Safety Agency, 2020.

[91] *Annex 14. Aerodromes*, 2020. International Civil Aviation Organization (ICAO).

[92] *Annex 6. Operation of Aircraft*, 2020. International Civil Aviation Organization (ICAO).

[93] *Annex 16. Environmental Protection - Volume III - Aeroplane CO2 Emissions*, 2017. International Civil Aviation Organization (ICAO).

[94] Jean-Yves Andro, Waldemar Rotärmel, Francesco Nebula, Gianfranco Morani, and Johan Steelant. Design of the actuation system of the hexafly-int hypersonic glider. In *HiSST 1st International Conference on High-Speed Vehicle Science & Technology*, 11 2018.

[95] Giuseppe Rufolo, Pietro Roncioni, Raffaele Votta, Marco Marini, and Salvatore Palazzo. Experimental and numerical aerodynamic data integration and aerodatabase development for the prora-usv1 reusable vehicle. In *14th AIAA/AHI Space Planes and Hypersonic Systems and Technologies Conference*, 11 2006. doi: 10.2514/6.2006-8031.

[96] Davide Ferretto, Roberta Fusaro, and Nicole Viola. Propellant subsystem design for hypersonic cruiser exploiting liquid hydrogen. In *AIAA AVIATION 2022 Forum*, 06 2022. doi: 10.2514/6.2022-3381.

[97] Pedro Goncalves, Ali İspir, and Bayindir Saracoglu. Development and optimization of a hypersonic civil aircraft propulsion plant with regenerator system. In *AIAA Propulsion and Energy 2019 Forum*, 08 2019. doi: 10.2514/6.2019-4421.